Volume 7, Issue 5, 2025

Print ISSN: 2663-1024
Online ISSN: 2663-1016

EURASIA JOURNAL OF SCIENCE AND TECHNOLOGY

Eurasia Journal of Science and Technology

Volume 7, Issue 5, 2025

Published by Upubscience Publisher

Eurasia Journal of Science and Technology
Print ISSN: 2663-1024 Online ISSN: 2663-1016
Email: info@upubscience.com
Website: http://www.upubscience.com/

Table of Content

Eurasia Journal of Science and Technology
Print ISSN: 2663-1024
Online ISSN: 2663-1016
DOI: https://doi.org/10.61784/ejst3105

ROBUST MULTI-OBJECTIVE CROP PLANNING IN MOUNTAINOUS NORTHERN CHINA VIA LP–NSGA-II–MONTE CARLO

ChiHo Thong[1], Jun Ren[2*], ShuHao Liu[3]
[1]*School of Economics and Finance, Huaqiao University, Quanzhou 362021, Fujian, China.*
[2]*College of Engineering, Huaqiao University, Quanzhou 362021, Fujian, China.*
[3]*School of Mathematical Sciences, Huaqiao University, Quanzhou 362021, Fujian, China.*
Corresponding Author: Jun Ren, Email: a2923734047@163.com

Abstract: This paper addresses the optimization of crop planting strategies for a mountainous rural village in northern China, characterized by diverse land resources and strict crop rotation requirements. A comprehensive mathematical modeling framework is developed, incorporating linear programming, genetic algorithms (NSGA-II), and Monte Carlo simulation to address multi-objective optimization and uncertainty in agricultural production. The study considers multiple practical constraints, including land type suitability, crop rotation, legume planting frequency, and limitations on greenhouse cultivation. The results reveal that the proposed models can effectively generate robust, adaptive cropping plans that maximize economic returns while reducing planting risks under both stable and fluctuating market conditions. The integration of Monte Carlo simulation enables the model to account for yield, price, and cost uncertainty, providing decision-makers with reliable strategies for risk management. The findings offer theoretical and practical guidance for agricultural planners and farmers, and the modeling framework has strong scalability for application in diverse environments.
Keywords: Crop planting optimization; Crop rotation; Genetic algorithm; Monte carlo simulation; Uncertainty management; Agricultural decision-making

1 INTRODUCTION

A rural village in the mountainous region of northern China possesses heterogeneous arable resources—flat dryland, terraced parcels, hillside plots, irrigated paddies, 16 conventional greenhouses and 4 smart greenhouses. Because each land class offers a distinct agro-ecological niche, crop selection must match plot characteristics while conforming to agronomic rules: legumes must appear at least once within every three-year cycle, and heavy-cropping of the same species in successive years is prohibited. To streamline field management, enhance production efficiency and curb planting risk, the present study formulates a mathematical optimisation framework that integrates land–crop suitability, expected yields, cultivation costs, market prices and projected sales volumes. The resulting model generates an optimal, rule-compliant planting strategy for every land type across the 2024 – 2030 planning horizon.

Bargués-Ribera & Gokhale studied the effect of crop rotation on disease transmission[1], and found that a reasonable crop rotation scheme can effectively reduce the accumulation of soil pathogenic microorganisms and increase crop yield. Bargués-Ribera & Gokhale studied the impact of crop rotation on disease transmission and found that a reasonable crop rotation programme can effectively reduce the accumulation of soil pathogenic microorganisms and increase crop yields. Martin studied uncertainty management at the farm level and used Monte Carlo simulation to evaluate the performance of cropping planning under market fluctuations[2], and found that the optimisation scheme considering uncertainties can significantly reduce market risks and improve the stability of agricultural returns. Zhan studied the optimisation of crop cropping structure[3], and proposed a fuzzy stochastic optimisation model, which was found to provide a more robust cropping strategy under uncertain market conditions and help to improve the science of agricultural decision-making. It is found that the model can provide a more robust planting strategy under uncertain market environment, which helps to improve the scientific nature of agricultural decision-making. Cao et al. studied the land use optimization problem based on the Non-dominated Sorting Genetic Algorithm II (NSGA-II)[4], and found that this method can effectively deal with the multi-objective optimization problem and minimize the environmental impact while maximizing the crop yield. Deb et al. proposed the NSGA-II algorithm and proved that it has high computational efficiency and reliability in solving the multi-objective optimization problems in agricultural production[5]. Chen et al. studied the application of genetic algorithms in crop planting optimisation[6], and found that the method can find suitable planting solutions according to different objectives (such as yield, cost and environmental impact) and improve the scientificity of planting decisions.

Existing research has made significant progress in crop optimisation, and methods such as linear programming, NSGA-II genetic algorithm and Monte Carlo simulation have improved the science of agricultural production decision-making to different degrees[7]. However, how to find a more efficient combination between multi-objective optimisation, uncertainty management and crop rotation pattern optimisation is still a problem that needs to be further explored in future research.

An optimal planting schedule for 2024 – 2030 is first established under relatively stable market conditions. To preserve profitability when prices fluctuate[8], the schedule is extended by introducing uncertainty parameters and re-optimising expected returns. The analysis is then broadened to capture substitution and complementarity among crops, yielding a multi-objective optimisation model that explicitly embeds these correlation effects. For a mountainous village in northern China[+], crop-planning decisions are governed by heterogeneous land categories and strict agronomic rules. The present study addresses these complexities by integrating a linear-programming model, the Non-dominated Sorting Genetic Algorithm II (NSGA-II) and Monte Carlo simulation[10]. Optimal rotation plans are produced for flat dryland, terraced plots, hillside fields, irrigated paddies and other terrain classes while respecting non-recurrent cropping, legume-rotation cycles and related constraints. A staged optimisation strategy progressively enlarges the objective set—from simple return maximisation, through uncertainty management, to the inclusion of inter-crop relationships—thereby providing a systematic response to the dual challenge of enhancing income and mitigating market-driven risk.

2 METHOD

2.1 Genetic Algorithm

The genetic algorithm (GA) operates by evolving a population of candidate solutions towards better fitness according to the following selection probability:

$$p_i = \frac{f(\mathbf{x}_i)}{\sum_{j=1}^{N} f(\mathbf{x}_j)} \tag{1}$$

where p_i is the probability of selecting individual i, $f(\mathbf{x}_i)$ is its fitness, and N is the population size.

Crossover and mutation operators are applied to generate new solutions, followed by fitness evaluation and selection. The algorithm iterates until convergence or a preset number of generations is reached.

Genetic algorithm model is an optimisation algorithm based on natural selection and genetic mechanism, which provides effective solutions to problems such as search, optimisation and learning by simulating the selection, crossover and mutation processes in biological evolution. Genetic algorithms are heuristic search algorithms, and their core idea is to find the optimal or near-optimal solution to a problem by simulating biological evolution.

In a specific application, the genes of an individual can represent the acreage and plot allocation for each crop. Through the selection operation, the better individuals have a higher probability of being retained and participate in the crossover process, where the good characteristics of different individuals (e.g., higher economic efficiency or resource utilisation) are combined to generate new individuals. The mutation operation, on the other hand, ensures the diversity of the solutions and prevents the algorithm from falling into local optimal solutions. After many generations of evolution, the genetic algorithm is able to find a near-optimal planting solution to maximise the revenue.

In the current crop planting planning problem, the optimal solution involves multiple decision variables (e.g., planting area and planting location for different crops). Genetic algorithms approximate the optimal solution step by step by constructing a population containing multiple possible solutions and using a natural selection mechanism to retain those individuals (i.e., planting schemes) that perform better. Each individual in the population represents a possible solution, and through repeated selection, crossover and mutation operations, the population gradually evolves to contain more and more individuals close to the optimal solution.

2.2 Monte Carlo Simulation

The Monte Carlo simulation estimates the expected value of an output function $g(\mathbf{x})$ using repeated random sampling:

$$E[g(\mathbf{x})] \approx \frac{1}{N}\sum_{i=1}^{N} g\left(\mathbf{x}^{(i)}\right) \tag{2}$$

where N is the number of samples and $g(\mathbf{x}^{(i)})$ is the result for the ii-th random input. The standard error is given by:

$$\mathrm{SE} = \frac{\sigma}{\sqrt{N}} \tag{3}$$

where σ is the sample standard deviation.

2.2.1 Probabilistic modelling of the definitional problem

The first task of Monte Carlo simulation is to identify the randomness and uncertainty in the problem, determine the random variables, choose the probability distribution and model the relationship.

2.2.2 Generation of random samples

This is one of the core steps in Monte Carlo simulation. To simulate the randomness in the problem, random samples must be generated from a predefined probability distribution. These samples will be used as inputs to the simulation to drive the system.

2.2.3 Conduct of simulation experiments

Once sufficient random samples have been generated, simulation experiments can be conducted to examine system behaviour and estimate key statistics. Monte Carlo analysis typically entails a large number of independent runs, each using a new random sample to emulate the system under varying conditions. Multiple repetitions are performed to

ensure the stability and reliability of the results. During each run, the random sample is entered into the model and the corresponding output is computed.

2.2.4Statistical analyses

Statistical analysis of a large number of experimental results enables useful information to be extracted from the simulated data. Common analytical techniques include the mean-value method, variance and standard deviation calculations, and the construction of confidence intervals.

2.2.5 Convergence and error analysis

This is the final step of the Monte Carlo simulation to ensure the reliability of the simulation results. As the number of experiments N increases, the simulation results should stabilise and converge to a realistic value. This process involves the following two aspects: convergence testing and error analysis.

2.3 NSGA-II

NSGA-II solves multi-objective optimization problems formulated as:

$$\text{Minimize:} \mathrm{F}(\mathbf{x}) = \left(f_1(\mathbf{x}), f_2(\mathbf{x}), ..., f_m(\mathbf{x})\right) \tag{4}$$

$$\text{Subject to:} \mathbf{x} \in \Omega \tag{5}$$

where F(x) is the objective vector, m is the number of objectives, and Ω is the feasible set.

The algorithm uses non-dominated sorting and crowding distance to select solutions:

$$d_i = \sum_{k=1}^{m} \frac{f_k^{i+1} - f_k^{i-1}}{f_k^{\max} - f_k^{\min}} \tag{7}$$

where d_i is the crowding distance for individual i.

Randomly generate an initial population Pt of size N, after non-dominated sorting, selection, crossover and mutation, generate the offspring population Qt, and unite the two populations to form a population Rt of size 2N; carry out rapid non-dominated sorting, and at the same time, carry out crowding computation of each individual in each non-dominated stratum, and according to non-domination and crowding, select suitable individuals to form the new parent population Pt+1; through the basic operations of genetic algorithm, generate a new offspring population Qt+1, and merge Pt+1 and Qt+1 to form the new population Rt, and repeat the above operations until the end of the procedure is satisfied. 1; generate a new offspring population Qt+1 through the basic operation of genetic algorithm, merge Pt+1 and Qt+1 to form a new population Rt, and repeat the above operations until the end of the programme is satisfied.

3 EXPERIMENTAL

3.1 Optimal Cropping Scenarios for Crops in 2024-2030

3.1.1 Data preprocessing

The data-pre-processing phase comprises three components: plot-area analysis, plot-type distribution analysis and crop-type statistics.

The size of each plot dictates the feasible cultivation scale. A census of available plots shows substantial variation: the largest parcel exceeds 200 acres, whereas several smaller plots cover less than 20 acres. To enhance overall planting efficiency, the optimisation model therefore imposes a plot-size constraint so that the planting area never surpasses a plot's maximum capacity.

Suitability for specific crops differs across plot types. Watered land favours rice or multi-season vegetables, while terraced and hillside plots support drought-tolerant cereals. A full inventory of land categories indicates that common greenhouses and terraces are most prevalent, whereas hillside and flat dryland parcels are comparatively scarce.

Crop-type statistics reveal that vegetables dominate at 43.9 % of the planted area, with cereals ranking second at 26.8 %. Although legumes occupy only a minor share, the rotation schedule still guarantees that every plot carries a legume crop at least once in a three-year cycle because of its agronomic importance.

The data are sourced from official datasets provided by the China Undergraduate Mathematical Contest in Modeling (CUMCM), the official website: https://www.mcm.edu.cn.

3.1.2 Setting of decision variables

The decision variable x_{ij}^t represents the area, measured in acres, of crop j planted on plot j in year t. Here, i denotes the plot number, ranging from 1 to 54; j indicates the crop type, ranging from 1 to 41; and t represents the year, covering a 7-year period from 2024 to 2030.

3.1.3 Restrictive condition 1

Limitations on the area of cultivated land: The total cultivated area of each plot cannot exceed its actual area.

$$\sum_{\mathrm{i}-1}^{41} x_{ij}^t \le A_i, \forall t, i \in [1,54] \tag{8}$$

Crop growing conditions: Different types of plots can only grow suitable crops, e.g. flat dry land, terraces and hillsides can only grow food crops, and greenhouses can only grow vegetables or mushrooms.

The suitability of flat drylands, terraces and slopes for the cultivation of food crops (other than rice) in a single season each year.

$$\sum_i x_{ij}^t \le A_j; i \in [1,26], j \in [1,16] \quad (9)$$

Rice grown in a single season per year on irrigated land.

$$\sum_i x_{ij}^t \le A_j; i \in [27,34], j \in [1,16] \quad (10)$$

Two seasons of vegetables are grown on watered land:
Season 1: Various vegetables other than cabbage, white radish and carrot

$$\sum_i x_{ij}^t \le A_j; i \in [27,34], j \in [17,34] \quad (11)$$

Season 2: One of cabbage, white radish and carrot

$$\sum_i x_{ij}^t \le A_j; i \in [27,34], j \in [35,37] \quad (12)$$

Common shed:
Season 1: Various vegetables other than cabbage, white radish and carrot

$$\sum_i x_{ij}^t \le A_j; i \in [35,50], j \in [17,34] \quad (13)$$

Season 2: Edible Mushrooms

$$\sum_i x_{ij}^t \le A_j; i \in [35,50], j \in [38,41] \quad (14)$$

Smart Shed:
Two vegetable seasons per year (except cabbage, white radish and carrot)

$$\sum_i x_{ij}^t \le 2A_j; i \in [51,54], j \in [17,34] \quad (15)$$

Non-cropping: The same crop cannot be grown on the same plot for two consecutive years to avoid the risk of yield reduction due to heavy cropping:

$$x_{ij}{}^t \times x_{ij}{}^{(t-1)} = 0, \forall i, j, t \quad (16)$$

Legume crop rotation requirements: Each plot should be planted with a legume crop at least once in every three years:

$$\sum_{t=T}^{T+2} \sum_{j \in [1,5] \cup [17,19]} x_{ij}^t \ge \epsilon, i \in [1,54], T = 2024,2027 \quad (17)$$

where ϵ is a positive number that ensures a certain area of cultivation of the legume crop.
Constraints on Non-Dispersed Planting Areas: To prevent cultivation zones for each crop from becoming overly fragmented, the model imposes restrictions that confine the planting areas of the same crop to adjacent plots:

$$|x_{ij}^t - x_{i'j}^t| \le \delta, \forall i, i' \text{is an adjacent plot of land} \quad (18)$$

where δ is the allowable acreage difference.
Limitations on the area of greenhouses: the planting area of ordinary greenhouses and intelligent greenhouses cannot exceed 0.6 acres, and the planting area of greenhouses for each crop should be limited to the specified range. For ordinary greenhouses, vegetables and edible fungi can be grown; intelligent greenhouses can only grow vegetables:

$$\sum_{j \in [17,34] \cup [38,41]} x_{ij}^t \le 0.6 \forall t, i \in [35,50] \quad (19)$$

$$\sum_{j \in [17,34]} x_{ij}^t \le 0.6 \forall t, i \in [51,54] \quad (20)$$

Since smart greenhouses can grow two seasons of vegetables per year, the acreage for each season needs to be constrained separately.

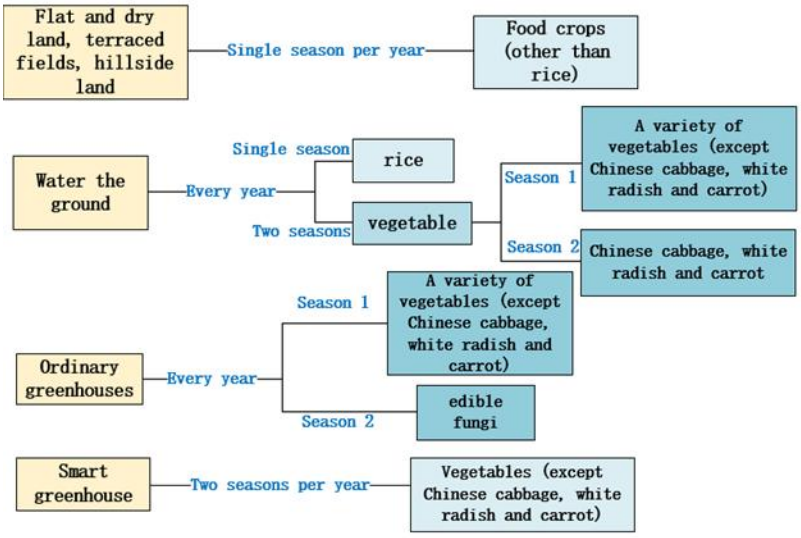

Figure 1 Crop Planting Condition Constraint Ideas

Figure 1 illustrates the core constraints for crop planting on various types of land. The figure clarifies that flat dry land, terraces, and hillsides are suitable for food crops, while greenhouses support the cultivation of vegetables and mushrooms. This visualization of constraints supports the model's practical value by ensuring that crop–land matching enhances both yield and risk mitigation.

3.1.4 Empirical results: scenario 1

Table 1 Optimal Planting Plan under Stable Market Conditions

Item	Soya bean	Black bean	.....	White mushroom (Pleurotus erythrorhizonticus)	Morel mushrooms
Season 1	1	0	.....	0	1
	.....	.....	.....	.....	.....
	0.62	0.54	.....	1	0
	0	1	.....	1	1
Season 2	.....	.....	.....	.....	.....
	1	0.78	.....	1	1

As shown in Table 1, the allocation of different crops in ordinary and smart greenhouses is clearly presented for each season. It can be observed that soybean and black bean are arranged such that rotation requirements are satisfied, and mushrooms are predominantly scheduled in the second season for both greenhouse types. This arrangement not only maximizes the efficient use of greenhouse space but also ensures compliance with rotation constraints, helping to maintain soil health and sustain high yields.

3.1.5 Modelling and solving

This subsection assumes that if the total production of a crop exceeds its expected sales volume, the excess is no longer wasted but is sold at 50 per cent of the 2023 sales price. Therefore, the objective is to develop an optimal planting plan for the years 2024-2030 that maximises total returns under this sales rule.

3.1.6 Determine the objective function

Unlike the scenario based on stable market conditions, the portion of the crop that exceeds the expected sales volume will be sold at half price.

Therefore, the objective function needs to differentiate and treat the return on the excess portion. For a certain crop j, the return can be divided into two parts:

Firstly, production $\mathrm{P_j t = x_{ij} t \times Y_j}$

When P_j^t is less than or equal to S_j^t:

$$Q_j^t = P_j^t \times R_j \tag{21}$$

WhenP_j^t exceeds S_j^t , the excess is sold at a 50% discounted price with the following revenue formula:

$$Q_j^t = S_j^t \times R_j + \left(P_j^t - S_j^t\right) \times R_j \times 0.5 \tag{22}$$

Thus, the total return can be expressed uniformly as:

$$Q_j^t = \min\left(P_j^t, S_j^t\right) \times R_j + \max\left(0, P_j^t - S_j^t\right) \times 0.5 \times R_j \tag{23}$$

Then, combined with the cost of cultivation, the objective function can be expressed as:

$$max \sum_{t=2024}^{2030} \sum_{i=1}^{34} \sum_{j=1}^{M} \min\left(x_i j^t \times Y_j, S_i\right) \times R_j + \max\left(0, x_i j^t \times A_j - S_i j^t\right) \times 0.5 \times R_j - x_{ij}^t \times C_j \quad (24)$$

3.1.7 Restrictive condition 2

Limitations on the area of cultivated land: The total cultivated area of each plot cannot exceed its actual area.

$$\sum_{j=1}^{41} x_{ij}^t \leq A_i, \forall t, i \in [1,54] \quad (25)$$

Crop growing conditions: Different types of plots can only grow suitable crops, e.g. flat dry land, terraces and hillsides can only grow food crops, and greenhouses can only grow vegetables or mushrooms.

$$\mathrm{x}_{\mathrm{ij}}^{\mathrm{t}} = 0 \text{ If the plot type is not suitable for growing crops} \quad (26)$$

Non-cropping constraints: The same crop cannot be grown on the same plot for two consecutive years in order to avoid the risk of yield reductions associated with heavy cropping:

$$x_{ij}{}^t \times x_{ij}{}^{(t-1)} = 0, \forall i, j, t \quad (27)$$

Legume crop rotation requirements: Each plot should be planted with a legume crop at least once in every three years:

$$\sum_{t=T}^{T+2} \sum_{j \in [1,5] \cup [17,19]} x_{ij}^t \geq \varepsilon, \forall i, T = 2024,2027 \quad (28)$$

where ϵ is a positive number that ensures a certain area of cultivation of the legume crop.

Limitations on the area of greenhouses: the planting area of ordinary greenhouses and intelligent greenhouses cannot exceed 0.6 acres, and the planting area of greenhouses for each crop should be limited to the specified range. For ordinary greenhouses, vegetables and edible fungi can be grown; intelligent greenhouses can only grow vegetables:

$$\sum_{j \in [17,34] \cup [38,41]} \mathrm{x}_{ij}^t \leq 0.6 \forall t, i \in [35,50] \quad (29)$$

$$\sum_{j \in [17,34]} \mathrm{x}_{ij}^t \leq 0.6 \forall t, i \in [51,54] \quad (30)$$

Since smart greenhouses can grow two seasons of vegetables per year, the acreage for each season needs to be constrained separately.

Limitations on types of greenhouse crops:

Ordinary greenhouses can only grow vegetables and mushrooms, not other crops:

$$x_{ij}^t = 0, \forall j \in [1,16] \quad (31)$$

Smart greenhouses can only grow vegetables, not other crops:

$$x_{ij}^t = 0, \forall j \notin [17,37] \quad (32)$$

3.1.8 Empirical results: scenario 2

Table 2 Optimal Planting Plan with Discounted Surplus Production

Item	Soya bean	Black bean	.....	White mushroom (Pleurotus erythrorhizonticus)	Morel mushrooms
	1	0	.....	0	1
Season 1	.....	.....	.....	.....	.....
	0.62	0.54	.....	1	0
	0	1	.....	1	1
Season 2	.....	.....	.....	.....	.....
	1	0.78	.....	1	1

Table 2 summarises the optimal crop layout when surplus output is sold at a discounted price. The plan maintains strict legume-rotation requirements and continues to schedule greenhouse capacity efficiently. Offering excess produce at a lower price encourages greater diversification, reflected in the lower dominance of any single crop within individual plots relative to the stable-market baseline.

3.2 Optimal Planting Programmes Taking into Account Uncertainty

To enhance practical relevance, the optimisation framework incorporates uncertainty in market performance, crop yields and cultivation costs. As market demand, yields and planting expenditures fluctuate over time, the model seeks a planting plan that accommodates such uncertainties while maximising expected future returns. The problem formulated under market uncertainty is inherently more complex than its stable-market counterpart; therefore, the multi-objective model is solved with the Non-Dominated Sorting Genetic Algorithm II (NSGA-II), producing a planting strategy that responds more robustly to market dynamics.

3.2.1 Uncertainty modelling: monte carlo simulation and NSGA-II.

(1) Monte Carlo simulation:

Key uncertainties include:

- Sales volume: Wheat and maize are set to grow at an annual rate of 5-10 per cent, with other crops fluctuating within a range of ±5 per cent per year.
- Yield per acre: Yield per acre may fluctuate ±10 per cent per year due to climatic influences.
- Cultivation costs: It is assumed that cultivation costs will increase by an average of 5 per cent per year.
- Selling prices: Market prices will also vary from crop to crop, with prices for vegetable crops expected to increase by 5 per cent per year, while prices for edible mushroom crops may decrease by 1-5 per cent.

Each variable can be represented by a random variable:

$$B_j^t = B_j^{2023} \times \left(1 + r_{B,j}^t\right) \quad (33)$$

$$Y_j^t = Y_j^{2023} \times \left(1 + r_{Y,j}^t\right) \quad (34)$$

$$C_j^t = C_j^{2023} \times \left(1 + r_{C,j}^t\right) \quad (35)$$

$$R_j^t = R_j^{2023} \times \left(1 + r_{R,j}^t\right) \quad (36)$$

Where $r_{sales\ volume,j}^t$、$r_{Y,j}^t$、$r_{C,j}^t$、$r_{R,j}^t$ are the growth rate or volatility of each variable, respectively, obeying the corresponding distribution (e.g., normal or uniform).

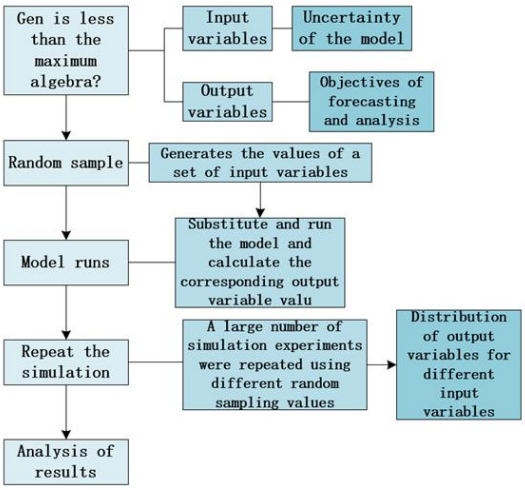

Figure 2 Monte Carlo Process

Figure 2 displays the Monte Carlo simulation process applied to crop planting strategy optimization. The flowchart demonstrates how random variables such as yield, price, and cost are incorporated into repeated simulation experiments. This process allows the model to robustly estimate outcomes under market uncertainty, providing a more reliable basis for decision-making.

(2) NSGA-II algorithm:

NSGA-II, an evolutionary technique well suited to multi-objective optimisation problems, is employed for crop-planting strategy optimisation so as to maximise expected returns while simultaneously minimising risks arising from market fluctuations.

Objective 1: Maximise returns:

$$f_1 = \sum_i \sum_j \left(P_{i,j} \cdot \min\left(C_{i,j} \cdot x_{i,j}, \text{Expectedsalesvolume}\right) + 0.5 \cdot P_{i,j} \cdot \max\left(C_{i,j} \cdot x_{i,j} - \text{Expectedsalesvolume}, 0\right)\right) \quad (37)$$

$P_{i,j}$: The unit sales price of the "j" crop grown on parcel "i".

$C_{i,j}$: The acreage of the "j" crop planted on parcel "i".

$x_{i,j}$: Area of the "j" th crop planted on the "i" th plot (decision variable).

Objective 2: Minimise planting costs:

$$f_2 = \sum_t \sum_j Plantingcost_{i,j} \cdot x_{i,j} \quad (38)$$

Planting cost: Unit cost of cultivation of crop "j" grown on plot "i".

3.2.2 Determine the objective function

Under uncertainty, the objective function is still to maximise expected returns over the period 2024-2030. Similar to the previous scenario based on stable market conditions, here the revenue parameters (such as sales volume, acreage, cost, and price) are treated as random variables or uncertain intervals.

When using Monte Carlo simulation, the objective function can be expressed as the average return under multiple scenarios, analogous to the stable market scenario:

$$maxE[\sum_{t=2024}^{2030}\sum_{i=1}^{34}\sum_{i=1}^{M}\left(\min\left(x_{ij}^{t}\times Y_{j}^{t},S_{j}^{t}\right)\times R_{j}^{t}-x_{ij}^{t}\times C_{j}^{t}\right] \quad (39)$$

Among them, $E[X]$ denotes the expected value over all random scenarios.
The other variables are similar.

3.2.3 Restrictive condition

Limitations on the area of cultivated land: The total cultivated area of each plot cannot exceed its actual area, viz:

$$\sum_{j=1}^{41} x_{ij}^{t} \le parcel\ area_i, \forall t, \forall i \quad (40)$$

Crop growing conditions: Different types of plots can only grow suitable crops, e.g. flat dry land, terraces and hillsides can only grow food crops, and greenhouses can only grow vegetables or mushrooms.

$$x_{ij}^{t} = 0_{\text{If the plot type is not suitable for growing crops}} \quad (41)$$

Non-cropping constraints: The same crop cannot be grown on the same plot for two consecutive years to avoid the risk of yield reductions associated with heavy cropping:

$$x_{ij}^{t} \times x_{ij}^{t-1} = 0, \forall i, j, t \quad (42)$$

Constraints on planting legumes once in three years: Each plot should be planted with legumes at least once in every three years:

$$\sum_{t=T}^{T+2}\sum_{j\in[1,5]\cup[17,19]} x_{ij}^{t} \ge \epsilon, \forall i, T = 2024{,}2027 \quad (43)$$

where ϵ is a positive number that ensures that the legume crop is planted on at least a certain area in three years.
Constraints on non-dispersed planting areas: The need to avoid spreading the planting areas of each crop too thinly can be addressed by adding constraints to limit the planting areas of the same crop to neighbouring plots:

$$|x_{ij}^{t} - x_{ij}^{t}| \le \delta, \forall i, i' \text{is adjacent plots} \quad (44)$$

where δ is the allowable acreage difference. Shed Size Limit: For each shed k, it cannot exceed 0.6 acres:

$$\sum_{j\in[17,34]\cup[38,41]} x_{ij}^{t} \le 0.6\forall t, i \in [35{,}50] \quad (45)$$

$$\sum_{j\in[17,34]} x_{ij}^{t} \le 0.6\forall t, i \in [51{,}54] \quad (46)$$

Since smart greenhouses can grow two seasons of vegetables per year, they need to be constrained separately for each season.
Limitations on types of greenhouse crops: Ordinary greenhouses can only grow vegetables and mushrooms, not other crops. Smart greenhouses can only grow vegetables, not other crops.

$$x_{ij}^{t} = 0\forall j \notin (1{,}16) \quad (47)$$

$$x_{ij}^{t} = 0\forall j \notin (17{,}37) \quad (48)$$

3.2.4 Fitness function

The fitness function evaluates the benefits and costs associated with each candidate cropping plan and verifies compliance with all constraints (e.g., plot size, crop-rotation intervals, heavy-cropping prohibitions). Any violation incurs a penalty, thereby reducing the individual's fitness score.
The following are the components of the fitness function:

Calculation of proceeds (f_1)

The objective is to maximise the return, which is given by the return formula:

$$B_{i,j} = \sum_{i}\sum_{j}\left(P_{i,j}\cdot\min\left(C_{i,j}\cdot x_{i,j}, S_{i,j}\right) + 0.5\cdot P_{i,j}\cdot\max\left(C_{i,j}\cdot x_{i,j} - S_{i,j}, 0\right)\right) \quad (49)$$

Among them, $P_{i,j}$ denotes the unit selling price of the j-th crop grown on plot i; $C_{i,j}$ represents the per-acre yield of this crop; and $x_{i,j}$ indicates the cultivated area allocated to crop j on plot i;
When production exceeds expected sales, the excess may be sold at a discounted price (thus multiplied by 0.5) or may even be sold late.
Costing (f_2)
The objective is to minimise the cost of planting with the cost formula:

$$C = \sum_{i}\sum_{j} C_{i,j}\cdot x_{i,j} \quad (50)$$

Here, Planting costs i,j is the unit cost of growing the crop, multiplied by the acreage of the crop$x_{i,j}$.
Introduction of the penalty function:
Since the solution must satisfy multiple constraints (e.g., plot-size limitations, crop rotation and recropping requirements), a penalty term is introduced into the fitness function. The penalty function reduces the fitness values of individuals violating constraints, thereby guiding algorithm convergence towards constraint-satisfying solutions.
The penalty function is designed as follows: Parcel size constraint penalties:

$$penalty1 = 0 \quad (51)$$

If the sum of the acreage planted to all crops on a given plot exceeds the maximum available acreage for that plot, the penalty value is increased:

$$penalty1 \mathrel{+}= 1000 \quad (52)$$

Crop rotation requirements for legumes are penalised:

$$penalty2 = 0 \quad (53)$$

If a plot has not grown a legume crop for three years, the penalty value is increased:

$$penalty2 \mathrel{+}= 1000 \quad (54)$$

Heavy stubble restraint penalties:

$$penalty3 = 0 \quad (55)$$

If a parcel grows the same crop in two consecutive years, the penalty value is increased:

$$penalty3 \mathrel{+}= 1000 \quad (56)$$

Total adaptation value

The final fitness function contains both objective values for benefits and costs and a penalty term. The fitness function returns two objective values:

Gain (maximisation): actual gain minus the value of the penalty for violating the constraint.

Cost (minimisation): the actual cost plus the penalty value for violating the constraint.

The specific formula is:

$$fitness1 = profit - penalty1 - penalty2 - penalty3 \quad (57)$$

$$fitness2 = cost + penalty1 + penalty2 + penalty3 \quad (58)$$

Interpretation of the adaptation function

For individuals that do not satisfy the constraints, the fitness value is significantly reduced by the presence of the penalty function. This motivates the NSGA-II algorithm to prefer retaining those individuals that satisfy the constraints.

If an individual fully satisfies all constraints, the penalty value is 0 and the fitness function considers only the true values of benefits and costs.

The weight of the penalty (e.g. 1000) can be adapted to the specifics of the problem to ensure that it is large enough to affect solutions that do not satisfy the constraints.

In this way, the fitness function both drives NSGA-II to optimise towards the objective value and ensures that the solution satisfies a variety of practical constraints.

3.2.5 Empirical results: scenario 3

Table 3 Optimal Planting Plan Considering Uncertainty

Strips	Crop	VintagesArea (of a floor, piece of land etc)		Lot 1
Lot 1	Wallabong (Bombay bean)	2024	0.68191	Lot 1
Lot 1	Crotonopsis pilosula	2025	0.68191	Lot 1
Lot 1	Wallabong (Bombay bean)	2026	0.68191	Lot 1
Lot 1	Wallabies	2027	0.68191	Lot 1
Lot 1	Wallabies	2028	0.68191	Lot 1
Lot 1	Crotonopsis pilosula	2029	0.68191	Lot 1
Lot 1	Wallabong (Bombay bean)	2030	0.68191	Lot 1
Lot 1	Millet	2024	4.99736	Lot 1
Lot 1	Millet	2025	4.99736	Lot 1
.....	.....	.....	.....	.....
Lot 53	Lettuce	2029	0.6	Lot 53
Lot 53	Lettuce	2030	0.6	Lot 53
Lot 54	Lettuce	2024	0.6	Lot 54
Lot 54	Lettuce	2025	0.6	Lot 54
Lot 54	Lettuce	2026	0.6	Lot 54
Lot 54	Lettuce	2027	0.6	Lot 54
Lot 54	Lettuce	2028	0.6	Lot 54
Lot 54	Lettuce	2029	0.6	Lot 54
Lot 54	Lettuce	2030	0.6	Lot 54
Lot 53	Lettuce	2029	0.6	Lot 53

Table 3 summarizes the optimal cropping schedule for each plot over the years 2024–2030 under uncertainty. From the table, it is clear that the rotation of crops—particularly legumes—has been well planned to avoid consecutive cropping and to fulfill rotation requirements. The allocation of lettuce in adjacent plots and the alternating use of various crops across years reflects the model's ability to manage both risk and sustainability in practice.

4 CONCLUSIONS

This study develops a comprehensive optimisation model for crop planning in a mountainous village of northern China, integrating land resources, crop attributes, market demand, and the interplay of substitutability and complementarity among species. By combining linear programming, Monte Carlo simulation and the NSGA II robust-optimisation framework, the model accommodates uncertainty in yields, costs and prices, providing resilient strategies across a range of market and environmental scenarios. The inclusion of agronomic constraints such as non-recurrent planting, legume rotation cycles and strict land-type limits ensures that the recommended plans are readily implementable in real-world production.

The modelling framework is easily extendable: additional drivers, including climate variability or policy shocks, can be incorporated with minimal structural change, enabling broad application. Region-specific calibration of climate, soil and market parameters also allows tailored deployment, giving farmers locally optimised planting schedules.

Embedding the model in an agricultural information platform or mobile application converts its outputs into intuitive, visual decision tools, streamlining on-farm management for producers and agricultural officers alike. At the policy level, the same predictive engine offers early warnings of supply-demand imbalances, supports subsidy design and guides crop-structure adjustments. Coupling the optimisation core with environmental metrics advances sustainable resource use, while integration with economic analysis maximises social and financial returns. Collectively, these innovations offer robust technical and strategic support for modernising regional agriculture and promoting long-term rural resilience.

COMPETING INTERESTS

The authors have no relevant financial or non-financial interests to disclose.

REFERENCES

[1] Bargués-Ribera M, Gokhale CS. Eco-evolutionary agriculture: Host-pathogen dynamics in crop rotations. PLoS Computational Biology, 2020, 16(1): e1007546.

[2] Martin M. Uncertainty at the Farm–Level: Monte–Carlo Simulations for Farm Planning. Office of Economics Working Paper 2020–05–E, U.S. International Trade Commission, 2020.

[3] Zhang C. Fuzzy stochastic optimization model and method for crop planting structure. Anhui Agricultural Science, 2019, 47(18): 243-246+250.

[4] Cao K, Batty M, Huang B, et al. Spatial multi-objective land use optimization: Extensions to the non-dominated sorting genetic algorithm-II. International Journal of Geographical Information Science, 2011, 25(12): 1949-1969.

[5] Deb K, Pratap A, Agarwal S, et al. A fast and elitist multiobjective genetic algorithm: NSGA-II. IEEE Transactions on Evolutionary Computation, 2002, 6(2): 182-197.

[6] Chen J, Zhang X, Li Y, et al. Crop planting optimization model based on genetic algorithm. Computers and Electronics in Agriculture, 2018, 150: 146-153.

[7] Ren Shuming, Xu Mengjie, Wang Qian. M&A and firm' s R&D: evidence from Chinese listed manufacturing firms. China Industrial Economics, 2017(7): 137- 155.

[8] Bowles TM, Mooshammer M, Socolar Y, et al. Long-term evidence shows that crop-rotation diversification increases agricultural resilience to adverse growing conditions in North America. One Earth, 2020, 2(3): 284-293.

[9] Mohammed A, Benkrid S, Andras P. Monte Carlo simulations for optimal crop planning under uncertain environments. Agricultural Systems, 2021, 189: 103063.

[10] Tian Y, Li X, Zhang H, et al. Agricultural production under climate change: A stochastic programming approach with scenario analysis. Journal of Agricultural Economics, 2020, 71(1): 32-49.

Eurasia Journal of Science and Technology
Print ISSN: 2663-1024
Online ISSN: 2663-1016
DOI: https://doi.org/10.61784/ejst3107

UNSUPERVISED SEGMENTATION OF DEFORMING 3D MESHES VIA DEFORMATION-AWARE GRAPH CUTS

Yu Su
Beijjing City International School, Beijing 100000, China.
Corresponding Email: susu071025@icloud.com

Abstract: We propose an unsupervised method for segmenting deforming 3D mesh sequences using a deformation-aware graph cut. Our approach constructs a spatiotemporal graph and formulates segmentation as a minimum s-t cut problem. Unary costs, derived from per-vertex deformation energy, separate near-rigid parts from deforming regions, while pairwise costs enforce spatial smoothness. By iteratively applying max-flow/min-cut, the algorithm greedily extracts coherent parts without supervision. Results show the automatic partitioning of complex animations into meaningful, temporally-consistent components, validating our approach.
Keywords: Graph cut; 3D mesh segmentation; Unsupervised learning

1 INTRODUCTION

Mesh segmentation is a fundamental problem in computer graphics[1-2]. While traditional methods partition static geometry based on cues like curvature and concavity[3], emerging needs in animation and 4D modeling require the segmentation of deforming mesh sequences. This task aims to identify near-rigid components that move coherently through a non-rigid animation, thereby partitioning the object into its functional or anatomical substructures.

Segmenting deforming meshes introduces the key challenge of maintaining temporal consistency, rendering purely geometric criteria insufficient. Segmentation must therefore account for temporal deformation patterns. Prior works have addressed this by detecting regions of large deformation or clustering motion trajectories[2]. Our work builds on this concept by leveraging per-vertex deformation magnitude as a primary cue to distinguish between highly dynamic and relatively static regions of a mesh.

This paper introduces an unsupervised, deformation-aware graph cut method for segmenting deforming mesh sequences. We formulate the problem as a binary vertex labeling task, solved via max-flow/min-cut optimization on a specially constructed graph. The graph's unary terms encode temporal deformation energy, while its pairwise terms encode the mesh's spatial adjacency. This formulation allows a minimum cut, corresponding to a globally optimal solution for this energy, to cleanly separate a single component from the deforming mesh.

Our approach uses a greedy strategy: each iteration applies a binary graph cut to isolate and remove the most rigid component, repeating on the remaining mesh. Relying solely on vertex deformation, it partitions shapes into meaningful segments without manual annotation or training data. Validation on a complex animation shows consistent identification of natural anatomical divisions across ~135 frames, indicating the promise of deformation-based graph cut segmentation for unsupervised dynamic shape analysis.

2 RELATED WORK

Static 3D Mesh Segmentation: Segmenting static 3D shapes often relies on surface geometry and concavity; for example, Katz and Tal used fuzzy clustering and minimum cuts at deep concavities for hierarchical mesh decomposition[4]. Many methods use shape-aware metrics for segmentation– e.g., spectral clustering on mesh graphs segments a mesh based on eigenfunctions of an affinity matrix[5], and shape diameter function (SDF) based segmentation uses a volumetric shape function to consistently partition the mesh[6]. Other methods cluster faces or vertices by geometric similarity or primitive fitting[7], aiming to segment objects into meaningful parts, often evaluated by alignment with human perception.

Another line of work has explored segmentation with graph-based algorithms. Golovinskiy and Funkhouser proposed a randomized hierarchical segmentation using multiple random cuts on a mesh graph[4]. Their method uses repeated randomized min-cuts to find segmentation boundaries, merging them into a final partition and demonstrating the effectiveness of graph cuts. Similarly, some methods use normalized cuts or other graph partitioning techniques[8]. Markov Random Field (MRF) models further refine segmentation by treating it as a mesh labeling problem with pairwise smoothness constraints.

Spatiotemporal and Dynamic Segmentation: Few studies address segmentation of deforming or animated meshes. Notably, Lee et al. segment mesh animations into near-rigid components by analyzing inter-frame face deformations[2]. They segment at high-deformation regions to approximate rigid parts, separating joints or bends. Later methods cluster vertices or faces by motion using space-time graphs. Similarly, our approach builds a spatiotemporal graph with deformation features.

Flow-Based Segmentation Methods: Graph cuts (e.g., Boykov-Jolly, Boykov-Kolmogorov) are widely used for global image segmentation. We extend this to deforming 3D meshes by formulating segmentation as energy minimization with

deformation and Potts-model costs, allowing direct use of max-flow/min-cut solvers. Unlike prior 3D methods, our approach automatically extracts deformation features from the sequence.
Supervised and Data-Driven Segmentation: While our method is unsupervised, learning-based methods like Kalogerakis et al. use Conditional Random Fields and labeled data for semantic segmentation, but require extensive training and are limited to known classes. In contrast, our approach requires no training or labels, discovering segments purely from motion, and is suitable when labeled data is unavailable.

3 METHODOLOGY

Our method segments a sequence of 3D meshes with full vertex correspondence, as commonly found in animations or simulations with fixed topology. This allows us to measure each vertex's motion over time and use it for segmentation.

4 GRAPH CONSTRUCTION

We construct a spatiotemporal graph $G = (V, E)$ where each node $v \in V$ corresponds to a vertex of the mesh (and by extension, the trajectory of that vertex across all frames). We add undirected edges between nodes to encode spatial adjacency and enforce smoothness of the segmentation:

- Spatial Edges: For any two vertices that are connected by an edge in the mesh's triangular connectivity, we add an edge in G. These edges connect immediate neighbors on the mesh surface. Let E_{spatial} denote this set of edges. They form a graph isomorphic to the mesh's vertex graph for each frame (since connectivity is constant over time).
- Temporal Connections: We *do not* add explicit temporal edges between the same vertex across frames; instead, each vertex is a single node capturing its temporal behavior via the unary term. Essentially, each node already represents the vertex across all frames. (If the correspondence were not given, one could create per-frame vertex copies and link them temporally[2], but that is not needed here.)

Next, we define an s-t graph structure for performing a binary cut. In addition to the nodes representing mesh vertices, we introduce two special terminal nodes: the Source (S) and Sink (T). Each mesh vertex can connect to S or T with a weighted edge, encoding a preference for that vertex to be in one of two labels (which we can think of as Label 1 = "part of the segment" vs Label 0 = "not part of the segment" in the current cut).

5 DEFORMATION ENERGY AND UNARY COSTS

The key driver for segmentation is the amount each vertex *deforms* over time. We compute a deformation energy for each vertex *i* as the total variance of its 3D position over the sequence. Denote the position of vertex *i* at frame *t* as $(x_{i,t}, y_{i,t}, z_{i,t})$. We calculate:
$$ d_i = \mathrm{Var}*t(x)* + \mathrm{Var}*t(y)* + \mathrm{Var}*t(z)*, $$
i.e., sum of coordinate variances over all frames. This scalar $d_i \ge 0$ measures how much vertex *i* moves; $d_i = 0$ would mean the vertex is static, while larger values indicate more motion. We then determine a rigidity threshold τ – chosen as the median of all ${d_i}$ values across the mesh. The intuition is that approximately half the vertices move less than τ (more rigid) and half move more (more deformable). Vertices with $d_i < \tau$ are likely part of relatively rigid components (e.g., core body parts), whereas vertices with $d_i \ge \tau$ often belong to highly deforming parts (e.g., limbs, extremities).
Using this deformation measure, we assign unary costs (terminal edge weights) for each vertex *i*:

- Connect vertex *i* to the Source with weight λ if $d_i < \tau$, else weight 0.
- Connect vertex *i* to the Sink with weight λ if $d_i \ge \tau$, else weight 0.

Here λ is a tunable constant that represents the strength of the unary bias. In practice we set λ to a moderate value (e.g. comparable to or slightly larger than typical pairwise costs) to enforce the deformation cue while still allowing the cut to deviate if needed. The above scheme means: low-deformation vertices have a cost λ if they are cut to the Sink side (i.e., not included in the part), whereas high-deformation vertices have a cost λ if cut to the Source side. In other words, the energy will be lower if low-motion vertices stay with the Source (label 1) and high-motion vertices stay with the Sink (label 0). This encourages the cut to separate the graph such that mostly low-motion vertices are on the Source side of the cut (forming the segment), and high-motion vertices are on the Sink side (excluded from that segment). The threshold τ thus biases the cut to prefer dividing the mesh along deformation lines.

6 PAIRWISE SMOOTHNESS TERM

To ensure that the resulting segment is spatially coherent, we add a pairwise smoothness cost on each edge between neighboring vertices. For each edge $(i,j) \in E_{\text{spatial}}$ connecting vertices i and j on the mesh, we assign a penalty if i and j end up in different labels. Specifically, the pairwise cost is:
$$ E_{\text{pair}}(i,j) = w \cdot \mathbf{1}(L_i \neq L_j), $$
where $L_i \in \{0,1\}$ is the binary label (Sink or Source) of vertex i, and $\mathbf{1}(\cdot)$ is an indicator function that is 1 if the argument is true (labels differ) and 0 if labels are the same. We choose a constant weight w (e.g. $w=150$ in our experiments) for all adjacency edges. This is essentially a Potts model smoothness prior: it penalizes cut edges and thus encourages the segment to be a contiguous region on the mesh. A high w means the algorithm will prefer

to cut fewer edges (creating larger, smoother segments) unless strongly compelled by the unary terms. If w is too low, the segmentation could become noisy or fragmented. In our setting, we found that a relatively large w (on the order of the median d_i values) works well, since we expect only a few major parts rather than a very intricate segmentation boundary.

Putting it together, the energy function for a binary labeling $L = {L_i}$ can be written as:

$$ E(L) = \sum_{i \in V} U_i(L_i) \;+\; \sum_{(i,j)\in E_{\text{spatial}}} w \cdot \mathbf{1}(L_i \neq L_j), $$

where $U_i(L_i)$ is the unary cost for assigning label L_i to vertex i, determined by d_i and τ as described above. This energy is submodular (it has the form of a graph cut with non-negative weights), so it can be minimized exactly by solving a minimum s-t cut (max-flow) problem. We use the Boykov-Kolmogorov algorithm via the PyMaxflow library to compute the min-cut efficiently.

7 ITERATIVE SEGMENTATION PROCEDURE

The graph and energy define a binary cut (Source: low-deformation core; Sink: remainder), but our goal is multi-part segmentation without pre-setting the number of segments. We use an iterative, greedy strategy: extract one segment at a time, remove it, and repeat binary segmentation on the rest, yielding a sequence of prominent parts.

Our algorithm is as follows (pseudocode form):

Input: mesh_sequence (with N vertices per frame), max_iterations, min_part_size

Output: segmentation_labels for all vertices (each vertex gets an integer part ID)

1. Compute per-vertex deformation energy d_i for all vertices (as above).
2. Initialize all vertex labels as 0 (meaning “unsegmented”).
3. Set current_label = 1.
4. For iter = 1 to max_iterations:

a. Let $U =$ set of vertices with label 0 (still unsegmented).

b. If $|U| <$ min_part_size, break (stop if remaining region is too small to segment further).

c. Construct graph G on U with edges and weights as defined (using the same τ and λ, w).

d. Run max-flow / min-cut on G to obtain an optimal binary split of U.

e. Let $S \subset U$ be the subset of vertices that are on the Source side of the cut (i.e., selected as the new segment).

f. If $|S| <$ min_part_size, then this cut is too small; mark those vertices as segmented (or continue) without assigning a new label and continue to next iteration.

g. Assign label = current_label to all vertices in S.

h. Remove S from U (they are now segmented); increment current_label by 1.

5. End For.
6. Return the segmentation labels.

This iterative procedure uses graph cuts to greedily extract the most coherent low-deformation region each time, starting with the largest rigid part and later segmenting more deformable regions. It stops when the maximum iterations are reached or too few vertices remain, avoiding spurious small segments.

We keep the deformation threshold τ fixed as the global median of all d_i, ensuring a consistent unary bias. Although τ could be updated per iteration, the global median proved effective and provides a stable criterion for "high" deformation.

The complexity of each graph cut is $O(V \cdot E)$ in practice with Boykov-Kolmogorov, which for our mesh (N vertices, ~N*3 edges for a triangulated mesh) is manageable. Since we typically extract only a handful of parts (on the order of 3-6 in our examples), the iterative approach is efficient.

8 RESULTS

We evaluated our method on a 135-frame 3D mesh sequence of a dancing cartoon mouse, comprising $N=5,000$ vertices with fixed connectivity. The animation includes varied motions such as arm waving and walking, causing significant deformation across different body parts (Figure 1).

Figure 1 Example Frames from the Input Deforming Mesh Sequence

As a prerequisite for segmentation, we compute the per-vertex deformation energy d_i . This metric effectively highlights extremities like the hands and feet as high-motion areas, while the torso and head remain relatively rigid. This energy map, shown in Figure 2, serves as the primary cue for our graph cut formulation.

Figure 2 Visualization of Per-Vertex Deformation Energy (Blue: Low, Red: High)

We set the rigidity threshold τ to the median of the deformation values and ran our iterative segmentation with a unary weight λ and a pairwise smoothness weight of $w=150$. A minimum part size of 50 vertices was enforced to prevent spurious segments.

The iterative process begins by isolating the most dynamic regions. In the first iteration, the graph cut separates the hands and feet, which exhibit the highest deformation due to waving and stepping. This initial result is depicted in Figure 3.

Figure 3 The First Cut Isolates the Highly Deformable Hands and Feet

After these extremities are removed, the second iteration segments the next most coherent part. The algorithm identifies a natural boundary at the neck and shoulders, cleanly partitioning the relatively rigid head and upper torso from the lower body, as illustrated in Figure 4.

Figure 4 The Second Cut Separates the Head and Upper Torso at the Neckline

In the final main iteration, the algorithm operates on the remaining lower body and tail, isolating the tail as a distinct component based on its motion pattern. This is shown in Figure 5.

Figure 5 The final Cut Isolates the Tail from the Lower Body

After three iterations, the algorithm yields four distinct segments: (1) hands and feet, (2) head and upper torso, (3) tail, and (4) the lower torso and legs. The final partition demonstrates smooth boundaries that align with natural joints and successfully recovers semantically meaningful regions, thanks to the pairwise smoothness term. The complete segmentation is visualized in Figure 6.

Figure 6 The Final Four-Part Segmentation of the Mesh, with Each Component Colored Uniquely

Qualitative results show our method produces meaningful segmentations: high-deformation regions are isolated early, head and torso are grouped then separated, and boundaries align with articulation points. The method is robust to minor mesh noise and motion inconsistencies, as the global deformation metric reduces the impact of short-term jitter. Without anatomical priors, it segments parts based on motion, often matching semantic regions, showing potential for automatic rigging or articulation analysis.

9 CONCLUSION

In this paper, we introduce an unsupervised method for segmenting deforming 3D mesh sequences based on a deformation-aware graph cut framework. Our approach formulates the task as an energy minimization problem on a spatiotemporal graph, where a unary term derived from per-vertex deformation magnitude distinguishes near-rigid from dynamic regions, and a pairwise term enforces spatial coherence. Through an iterative application of the max-flow/min-cut algorithm, our method greedily extracts motion-consistent components without requiring training data or manual annotations, successfully partitioning complex animations into meaningful, temporally-consistent segments that align with natural anatomical parts. This work validates the adaptation of graph-cut techniques for robust dynamic shape analysis. Future research directions include exploring global multi-label optimization to replace the iterative binary scheme and conducting a comprehensive quantitative evaluation against established benchmarks.

COMPETING INTERESTS

The authors have no relevant financial or non-financial interests to disclose.

REFERENCES

[1] Katz S, Tal A. Hierarchical Mesh Decomposition Using Fuzzy Clustering and Cuts. ACM Transactions on Graphics (Proc. SIGGRAPH), 2003, 22(3): 954–961.
[2] Golovinskiy A, Funkhouser T. Randomized Cuts for 3D Mesh Analysis. ACM Transactions on Graphics, 2008, 27(5): 145.
[3] Kalogerakis E, Hertzmann A, Singh K. Learning 3D Mesh Segmentation and Labeling. ACM Transactions on Graphics, 2010, 29(4): 102.
[4] Lee TY, Wang YS, Chen TG. Segmenting a Deforming Mesh into Near-Rigid Components. The Visual Computer, 2006, 22(9-11): 729–739.
[5] Shapira L, Shamir A, Cohen-Or D. Consistent Mesh Partitioning and Skeletonisation using the Shape Diameter Function. The Visual Computer, 2008, 24(4): 249–259.
[6] Liu R, Zhang H. Segmentation of 3D Meshes through Spectral Clustering. Proceedings of Pacific Graphics, 2004: 298–305.
[7] Boykov Y, Jolly MP. Interactive Graph Cuts for Optimal Boundary & Region Segmentation of Objects in N-D Images. Proceedings of ICCV, 2001: 105–112.
[8] Boykov Y, Kolmogorov V. An Experimental Comparison of Min-Cut/Max-Flow Algorithms for Energy Minimization in Vision. IEEE Transactions on Pattern Analysis and Machine Intelligence, 2004, 26(9): 1124–1137.

Eurasia Journal of Science and Technology
Print ISSN: 2663-1024
Online ISSN: 2663-1016
DOI: https://doi.org/10.61784/ejst3109

OPTIMAL CROP PLANTING STRATEGY BASED ON PARTICLE SWARM ALGORITHM

TianYou Zuo[1*], LiangYing Ji[2], YuSa Liu[3]
[1]*Department of School of Overseas Education, Changzhou University, Changzhou 213164, Jiangsu, China.*
[2]*Department of School of Safety and Engineering, Changzhou University, Changzhou 213164, Jiangsu, China.*
[3]*Department of College of pharmacy, Changzhou University, Changzhou 213164, Jiangsu, China.*
Corresponding Author: Tianyou Zuo, Email: 15961207191@163.com

Abstract: With the development of rural economy, optimizing planting strategy is an important research topic in organic planting industry. At present, most experts are not clear about the binding conditions for crop planting. This paper searched for data on agricultural products and local soil conditions in Hutang Town, Changzhou City, Jiangsu Province, and identified data on local cropping strategies for 2023. Based on the above data and the ideas of linear programming and multi-objective programming, the planting strategy optimization model under multiple constraints was established by determining planting risk factors and other indicators to seek the optimal crop planting strategy with maximum returns, and particle swarm optimization algorithm was used to solve the model. Finally, the optimal planting strategy under certain conditions and uncertain factors is obtained, and the complex problems arising from the optimal crop planting strategy are solved.
Keywords: Linear programming; Monte carlo simulation; Poisson process; Particle swarm optimization

1 INTRODUCTION

With the development of rural economy, the issue of optimizing planting strategies is an important research topic in the organic farming industry. Obtaining optimal crop planting strategies has become more difficult under many changing cropping conditions and policy economics.

Prof. Xu Zhihong of the University of Chinese Academy of Sciences and others pointed out in his article “The Development Status and Future Trends of Chinese Agriculture” that the adjustment of agricultural planting strategies is very complex and should be adjusted to the trend, but did not give a specific strategy in the context of the actual situation[1]. In other articles, they propose a proposal for optimizing crop planting strategies under specific natural conditions such as climatic and soil conditions in the Sichuan region, but in practice the influence of humanistic conditions on planting strategies is very important, and the above mentioned article did not specify the changes that these conditions may bring to the planting strategies[2].Some teams made a more detailed combination of natural and human factors on the impact of planting strategy for analysis, and we found that in practice there are some uncertainties such as sudden natural disasters on the cultivation of the judgment of the interference, which we believe that we need to add[3].

Therefore, we combine the natural and human conditions of crop cultivation and stochastic simulation of uncertainties to construct a more accurate model of crop cultivation strategies.

After model building and solving, this paper derives the local crop planting strategy for the next seven years. This makes up for the lack of integration of natural factors, human factors and uncertainties into the model building in the above literature, which better maximises crop revenue, improves farmers' economic income and positively affects local economic growth. Finally, we make a comprehensive evaluation of the proposed model, and consider that the model in this paper fits the reality, can reasonably solve the proposed problems, and has the characteristics of strong practicability and high efficiency of algorithm. The model is also applicable to forestry, animal husbandry and other aspects.

2 RELATED THEORIES

2.1 Monte Carlo Simulation

The Monte Carlo method, also known as statistical simulation, is a stochastic simulation method, a computational method based on probabilistic and statistical theoretical methods, and an approach to solving many computational problems using random numbers (or, more commonly, pseudo-random numbers). The problem to be solved is linked to a certain probabilistic model, and statistical simulation or sampling is implemented using an electronic computer to obtain an approximate solution to the problem.

When the problem to be solved is the probability of occurrence of a certain event, or the expected value of a certain random variable, they can obtain the frequency of occurrence of this event, or the average value of this random variable, by means of a certain “test” method, and use them as a solution to the problem. The Monte Carlo method is a numerical simulation of an experiment by capturing the geometric quantities and geometric features of the motion of a thing and

simulating them mathematically[4]. It is based on a probabilistic model and follows the process depicted in this model, by simulating the results of the experiment as an approximate solution to the problem. Monte Carlo problem solving can be reduced to three main steps: constructing or describing the probabilistic process; realizing sampling from a known probability distribution; and establishing various estimators[5].

2.2 The Particle Swarm Optimization

Particle swarm algorithm is an optimization algorithm based on group intelligence, and its basic idea originates from the study of the foraging behavior of bird flocks, by initializing the particle swarm, evaluating the fitness of each particle, and initializing the individual optimum and the global optimum. Repeat the above steps to update the individual optimal and global optimal until the global optimal solution is found and output, which is mainly used to solve continuous nonlinear optimization problems.

Assuming that there is a D-dimensional target search space with n particles forming a particle swarm, where each particle is described by a D-dimensional vector, denote its spatial location as $m_i = (m_{i1}, m_{i2}, \cdots, m_{iD})$, $i = 1, 2, \cdots, n$; This can be viewed as a solution in an objective optimization problem, and substituting the fitness function to calculate the fitness value can measure the merit of the particles; the flight speed of the ith particle is also a D-dimensional vector, denoted as $v_i = (v_{i1}, v_{i2}, \cdots, v_{iD})$[6].The position experienced by the ith particle with the best fitness value is called the best position in the history of the individual and is denoted as $p_i = (p_{i1}, p_{i2}, \cdots, p_{iD})$: The best position experienced by the entire particle population is called the global historical best position, denoted as $p_g = (p_{g1}, p_{g2}, \cdots, p_{gD})$, The evolutionary equation for a swarm of particles can be described as follows[7].

$$v_{ij}(t+1) = v_{ij}(t) + c_1 r_1(t)\left(p_{ij}(t) - x_{ij}(t)\right) + c_2 r_2(t)\left(p_{gj}(t) - x_{ij}(t)\right) \tag{1}$$

$$m_{ij}(t+1) = m_{ij}(t) + v_{ij}(t+1) \tag{2}$$

Where i denotes the ith particle, j denotes the jth dimension of the particle, t denotes the tth generation, and c_1, c_2 are two acceleration constants that usually take values in the range $(0,2)$, $r_1 \sim U(0, 1)$, $r_2 \sim U(0, 1)$ are two mutually independent random functions[8]. From the above equation, we see that c_1 regulates the particle to go to the best position in its own neighborhood, and c_2 regulates the particle to go to the best position that can be found by the whole swarm of particles.

2.3 The Poisson Process

The Poisson distribution is one of the most important discrete distributions, and it occurs mostly in occasions such as when X denotes the number of events that occur in a certain time or space[9].

Assuming that natural disasters will occur k times over a long period of time 0-τ, take a very large natural number n and divide the time period 0-τ into equal n segments:

$$l_1 = \left[0, \frac{1}{n}\right], l_2 = \left[\frac{1}{n}, \frac{2}{n}\right], ..., l_i = \left[\frac{i-1}{n}, \frac{i}{n}\right], ..., l_n = \left[\frac{n-1}{n}\right] \tag{3}$$

Make the following two assumptions:

1. The probability of a natural disaster occurring exactly once in every l_i is approximately proportional to the length of this period of time, $\frac{1}{n}$, which can be set to$\frac{\gamma}{n}$. When n is large, $\frac{1}{n}$ is small, and it is impossible for two or more natural disasters to occur in such a short period of time as l_i. Therefore the probability that a natural disaster does not occur during a period of time l_i is $1 - \frac{\gamma}{n}$.

2. The segments $l_i,...,l_n$ are independent when it comes to whether a natural disaster occurs or not.

Set each small segment to be $\delta = \frac{\tau}{n}(n \to \infty)$, where the probability that k natural disasters may occur in time δ is P(k, δ), then:

$$P(k, \delta) = \begin{cases} 1 - \lambda\delta & k = 0 \\ \lambda\delta & k = 1 \\ 0 & k > 0 \end{cases} \tag{4}$$

The probability that a natural disaster occurs k times in n subsections is then:

$$C_n^k P^k (1-p)^{n-k} \qquad P = \lambda\delta \tag{5}$$

$$e^k = \lim_{n\to\infty}\left(1 + \frac{k}{n}\right)^n \tag{6}$$

In turn, a Poisson process is used to model the probability of occurrence of a natural disaster, and this probability is used as a planting risk factor to influence the objective function[10].

3 EXPERIMENT

The model fully considers the impact of expected sales volume, planting cost, mu yield and other factors on planting strategy, and lists a total of 19 constraints on the model according to the requirements of different aspects of the constraints to ensure the accuracy and reliability of the model. Monte Carlo simulation is introduced to simulate the planting cost, mu yield and other decision variables with a small range of uncertainty. For the potential planting risk,

this paper introduces the concept of planting risk factor, which is obtained in the form of probability according to the Poisson process, and constructs the linear relationship between the factor and the objective function, so as to satisfy the simulation of the planting risk affecting the return. As the increase in the number of constraints increases the model complexity, this paper increases the number of iterations when choosing the particle swarm optimization algorithm to solve the problem, so as to make the model results closer to the optimal results. The particle swarm algorithm flow is shown in Figure 1.

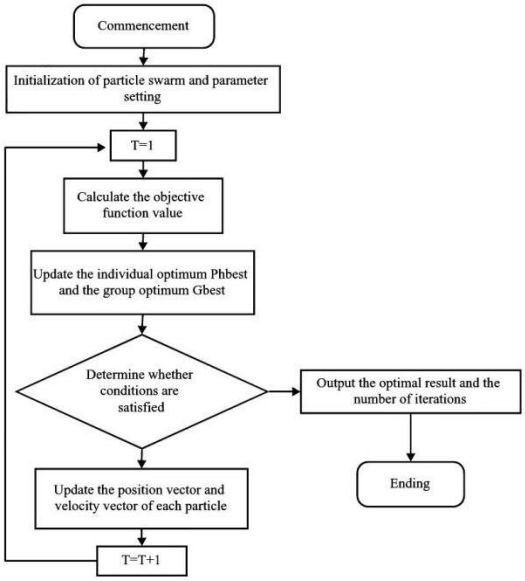

Figure 1 Particle Swarm Optimization Algorithm Model Illustration

According to the crop cultivation data in the Hutang Town area of Changzhou City that we have found, this paper derives the following objective function:

$$\max\left\{\sum_{k=1}^{2}\sum_{i=1}^{N}\sum_{j}\sum_{t}\left[x_{ijkt}S_j(t)P_j(t)D_j(t)\right]-\sum_{k=1}^{2}\sum_{i=1}^{N}\sum_{j}\sum_{t}x_{ijkt}C_i(t)\right\}\left[-P(k,\tau)+1\right] \tag{7}$$

Included among these:

x_{ijkt} denotes the area of crop j planted in plot i in the kth season in year t;$i\in[1,...N]$:denotes plot I;$j\in[1,...M]$:denotes the jth crop;t is the planting year and $t\in T=\{2024,2025,2026...2030\}$;$D_j$ is the expected sales volume;P_j is the acre yield of each crop, and;C_j is the cost of cultivation;S_j is the selling price;T is the type of planting;A_j is the total area of the jth plot or shed.

Combined with the data related to specific practical conditions, this paper gives the following constraints:

$$\text{st.}\begin{cases} D_i(t)=D_i(2023)\cdot(1+r_{i,t}),\ r_{i,t}\in[0.05,0.10],\ \forall i\in\{C_6,C_7\},t\in\{2024,...,2030\} \\ D_i(t)=D_i(2023)\cdot(1+r_{i,t}),\ r_{i,t}\in[-0.05,0.05],\ \forall i\notin\{C_6,C_7\},t\in\{2024,...,2030\} \\ p_i(t)=p_i(2023)\cdot(1+u_{i,t}),\ u_{i,t}\in[-0.1,0.1],\ \forall i,t\in\{2024,...,2030\} \\ c_i(t)=c_i(2023)\cdot(1+0.05)^{t-2023},\forall i,t\in\{2024,...,2030\} \\ s_i(t)=s_i(2023),\ \forall i \text{ with } S_i=S_1\cup S_2,t\in\{2024,...,2030\} \\ p_i(t)=p_i(2023)\cdot(1+0.05)^{t-2023},\ \forall i \text{ with } S_i=S_3\cup S_4,t\in\{2024,...,2030\} \\ p_i(t)=p_i(2023)\cdot(1-v_{i,t}),\ v_{i,t}\in[0.01,0.05],\ \forall i \text{ with } S_i=S_5,t\in\{2024,...,2030\} \\ p_{41}(t)=p_{41}(2023)\cdot(1-0.05)^{t-2023},\ t\in\{2024,...,2030\} \end{cases} \tag{8}$$

The optimal strategy for crop cultivation in Hutang Town, Changzhou City, in the next seven years was derived by solving the above model using particle swarm optimization algorithm. The details are as follows.

4 RESULTS

In solving the above model, this paper adopts the particle swarm optimization algorithm, and after simulating through many iterations, it comes up with the planting strategies of different crops in the next 7 years, in which this paper selects the planting strategy in 2024 for displaying.

As shown in the table below, Table 1 indicates particle swarm optimization model parameters, and Table 2 indicates Selected results of crop cultivation distribution in 2024.

Table 1 Particle Swarm Optimization Model Parameters

Parameter description	Parameter values	Parameter description	Parameter values

Inertial Weight	0.5	Particle Number	30
Individual Learning Factor	1.5	Maximum number of iteration	5000
Social learning Factor	1.5	Monte Carlo simulations	100

Table 2 Selected Results of Crop Cultivation Distribution in 2024

Area number	Crop name	Area size (acres)	Planted area (acres)
A1	Broomcorn	80	72.3
A2	Barley	55	55.0
B1	Refried beans	60	59.3
B2	Barley	46	42.0
C1	Buckwheat	15	14.7
D7	Kidney bean	15	15.0
E1	Mushrooms	0.6	0.3
E2	Morel mushrooms	0.6	0.3
F2	Capsicum	0.6	0.3

Based on the adjustment of the above particle swarm parameters (as shown in Table1), some results of crop planting strategies were derived (as shown in Table2). Based on the above crop planting strategies, this paper concludes that the total crop income in the local area in the next 7 years is about 20 million yuan.

5 CONCLUSIONS

In this paper, we have fully considered the factors affecting the planting strategy such as expected sales volume and planting cost, and listed a total of several constraints to impose different forms of restrictions on the model as required. We introduced Monte Carlo simulation to simulate decision variables such as planting cost and mu yield with a small degree of uncertainty. For potential planting risk, we introduced the concept of planting risk factors and calculated the factors in probabilistic form using Poisson process.

Eventually, a crop cultivation strategy for the next seven years in Hutang Town, Changzhou City was derived. The output of the model meets the requirements of the topic and can solve practical problems. The particle swarm optimisation algorithm used in this paper has the characteristics of high stability and strong global search ability, which is very suitable for solving complex multi-objective optimisation models. The model can be more widely promoted. In the field of animal husbandry, the parameter of the number of livestock breeds can be used to replace the parameter of the planting area of agricultural products, so as to solve the problem of the optimal breed purchase strategy under limited economic conditions.

COMPETING INTERESTS

The authors have no relevant financial or non-financial interests to disclose.

REFERENCES

[1] Xu Zhihong, Sun Caixin, Zhang Xiaoxing, et al. The Development Status and Future Trends of Chinese Agriculture. Transactions of China Electrotechnical Society, 2021, 19(10): 53-58.
[2] Fangfang. Analysis of Crop Cultivation Techniques and Factors Affecting High Yield. Harbin Institute of Technology, 2022, 34(2): 57-63.
[3] Ma Xuesong. Comprehensive data: area under cultivation of major crops and trends in China. IEEE Transactions on Power Systems, 2021, 16(4): 798-805.
[4] Ma Kunlong. Monte Carlo and Quasi-Monte Carlo Methods. Changsha: Hunan University, 2020, 6(1):107-115.
[5] Shen Xianjun. Adaptive particle swarm optimisation algorithm and its applications. Systems Engineering-Theory and Practice, 2022, 30(1): 158-160.
[6] Tang Guosheng. Particle swarm and applications. Journal of Higher Education, 2023, 9(11): 53-56.
[7] Liu Zhimei. Deep integration of Mathematical Modeling and Mathematics Teaching in Higher Vocational Colleges. Journal of Jiamusi Vocational College,2023, 39(03):152-154.
[8] Xu Yatao, Wu Libao. Research on Evaluation index system of Mathematical modeling teaching in Senior high school based on Delphi AHP. Journal of neijiang normal college, 2023, 38(02): 113-119.
[9] Yang Benchao, Shi Yaan, Duan Ganheng, et al. Analysis of price fluctuation of agricultural products in China and its influencing factors. University Education, 2023(04): 44-46.
[10] Huang Jian, Xu Binyan. Research on crop production risk management based on Monte Carlo simulation. Journal of Mathematics Education, 2020, 32(01): 93-98.

Eurasia Journal of Science and Technology
Print ISSN: 2663-1024
Online ISSN: 2663-1016
DOI: https://doi.org/10.61784/ejst3108

LATERAL FORCE OF MIXING DRUM IN CONCRETE MIXER TRUCK BASED ON EDEM

YuHuan Gao
Huaiyin Institute of Technology, Huaian 223200, Jiangsu, China.
Corresponding Email: 806892554@qq.com

Abstract: Concrete demonstrates fluid properties, which results in specific dynamic behaviors during the transit of concrete mixer trucks. A defining operational trait of these vehicles is that their Concrete Mixing Drum sustain continuous rotation while the trucks are in motion. When a concrete mixer truck makes a turn, the concrete inside the Concrete Mixing Drum undergoes load migration—a phenomenon primarily induced by the combined effects of the concrete's intrinsic fluidity and the centrifugal force generated by the Concrete Mixing Drum's rotation. This load migration is often accompanied by dynamic impacts that exert forces on the Concrete Mixing Drum and the vehicle's chassis. Notably, when the truck's speed increases slightly, the aforementioned load migration and dynamic impacts further deteriorate the vehicle's roll stability. Once the roll stability drops below a critical level, the risk of the truck encountering a rollover accident rises significantly, potentially endangering road safety, property, and human lives. To address this pressing issue, the present study focuses on investigating the Lateral Force generated during the concrete mixing process, as these forces are key factors contributing to the compromised roll stability of the vehicle. To achieve this research goal, EDEM software—a specialized tool for discrete element method simulations—was utilized to conduct numerical simulations of the concrete mixing process inside the Concrete Mixing Drum. The simulations were designed to cover two distinct Filling Ratio conditions of the Concrete Mixing Drum: one with a Filling Ratio of 1:1, corresponding to a total mass of concrete and aggregates of 10,000 kg, and the other with a Filling Ratio of 1:1.2, where the total mass of concrete and aggregates amounts to 12,000 kg. Additionally, three different Rotational Speed of the Concrete Mixing Drum—2 rpm (revolutions per minute), 5 rpm, and 10 rpm—were incorporated into the simulations to examine their respective influences on the generation and magnitude of Lateral Force. By analyzing the simulation data under these varied conditions, the study aims to gain insights into how Filling Ratio and Concrete Mixing Drum Rotational Speed affect Lateral Force characteristics, thereby providing a theoretical foundation for enhancing the roll stability of concrete mixer trucks and mitigating the risk of rollover accidents.
Keywords: Concrete mixing drum; Filling ratio; Rotational speed; Lateral force

1 INTRODUCTION

Concrete mixer trucks are specialized engineering vehicles in the field of engineering and construction[1]. During the transportation of concrete, the Concrete Mixing Drum of the concrete mixer truck needs to rotate continuously to prevent concrete segregation. Under different Filling Ratio and Rotational Speed conditions, the impact of concrete on the Concrete Mixing Drum may reduce the stability of the concrete mixer truck, making it prone to rollover under the influence of the Concrete Mixing Drum's rotation when turning. In 2016, Sun Yunqi et al. conducted a simulation study using Workbench software to analyze the stress and deformation of the Concrete Mixing Drum of concrete mixer trucks under braking conditions. Bogdan Cazacliu elaborated on the mixing process of the Concrete Mixing Drum in mixer trucks and also explained the working principle of this type of vehicle.In recent years, rollover accidents of concrete mixer trucks have occurred frequently. Many researchers have explored the causes of rollover of concrete mixer trucks, but there is little research on the Lateral Force generated by the Concrete Mixing Drum when mixing concrete with different Filling Ratio and under different Rotational Speed conditions[2][3]. The concrete carried by concrete mixer trucks has a large mass; the most commonly used 12-cubic-meter concrete mixer truck can carry up to nearly 30 tons of concrete and aggregates. During the rotation of the Concrete Mixing Drum, a huge Lateral Force will be generated, which will have a significant impact on the stability of the concrete mixer truck.

In conclusion, studying the Lateral Force generated by the Concrete Mixing Drum during the mixing process is of positive significance for preventing the rollover of concrete mixer trucks. In this paper, the working conditions close to the actual concrete transportation scenario were selected, including the Concrete Mixing Drum loaded with 10,000 kg and 12,000 kg of concrete and aggregates (with Filling Ratio of 1:1 and 1:2 respectively), as well as the working conditions with Rotational Speed of 2 rpm, 5 rpm and 10 rpm[4].

2 SIMULATION DESCRIPTION

2.1 Structure of the Concrete Mixing Drum

As the core component of concrete mixer trucks, the 12-cubic-meter mixing drum typically adopts a pear-shaped three-section cylinder structure. Inside the Concrete Mixing Drum, there are double logarithmic spiral blades (with a staggered angle of 1120°), which feature a segmented variable-parameter design: the maximum angle of the front cone section is 25°, the maximum angle of the cylindrical section is 20°, and the maximum angle of the rear cone section is 112°[5]. This structural design enables the mixing, lifting, and turning of concrete through the spiral pushing effect during rotation, ensuring uniform mixing of materials. Its overall dimensions must match the mixing capacity. meanwhile, the agitating Rotational Speed must comply with relevant standards (e.g., ≤ 10 r/min) to guarantee mixing effectiveness while preventing concrete segregation. The geometric accuracy of the drum wall and blades directly affects the movement trajectory of granular materials and the accuracy of simulation results. Therefore, attention must be paid to the geometric accuracy of the drum wall and blades when modeling the Concrete Mixing Drum. The structural dimension diagram of the Concrete Mixing Drum system is shown in Figure 1.

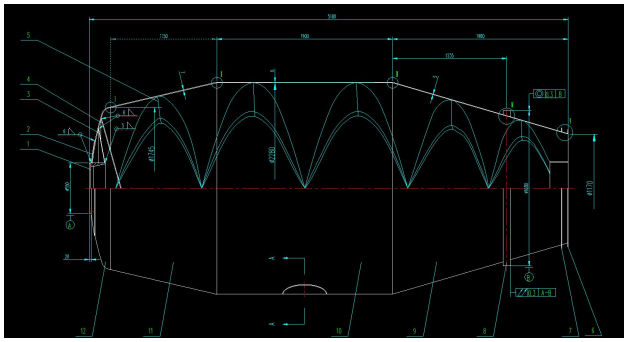

Figure 1 Structural Dimensions of the Concrete Mixing Drum System

2.2 Modeling of the Concrete Mixing Drum

When drawing a 12-cubic-meter Concrete Mixing Drum in SolidWorks, the most critical step is to draw the spiral blades on the corresponding reference plane, rotate them by 180°, and generate a single blade using the "Sweep" function. After completing the modeling of the Concrete Mixing Drum, the model is saved in STL format to facilitate its subsequent import into EDEM software.It is crucial to ensure that an appropriate precision is selected when saving the model in STL format (to avoid excessively high precision leading to an overly large file that impairs simulation efficiency, or excessively low precision resulting in the loss of key structural details such as spiral blades).Meanwhile, check the integrity and geometric accuracy of the spiral blades inside the Concrete Mixing Drum (to prevent deviations in particle motion simulation in EDEM caused by issues such as missing blades or damaged surface areas), and confirm that the model coordinate system is consistent with the EDEM simulation scenario coordinate system. This will reduce the adjustment workload during subsequent scenario construction and ensure the accuracy of the simulation results.The parameters of the concrete mixing drum are shown in Table 1.The view is shown in Figure 2-5.

Table 1 Parameters of the Concrete Mixing Drum

Name	Total Weight
Nut M8	0.96
Bolt M8×25	1.32
Washer M8	0.048
Liner Plate	2.4
Access Hole Cover Plate	8
Sealing Ring	0.14
Head (or End Closure)	111.65
Front Cylinder Body	418.3
Middle Cylinder Body	639
Rear Cylinder Body	395.9
Concrete Mixing Drum	173.2
Rear Retaining Ring	3.05
Front Retaining Ring	4.06
Spiral Blade Group	282.6
Material Return Plate	101

Inner Support Plate	24.8
Outer Reinforcement Plate	23.3
Flange	57.8

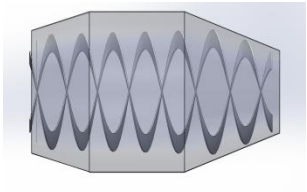

Figure 2 Left View

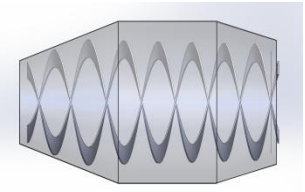

Figure 3 Right View

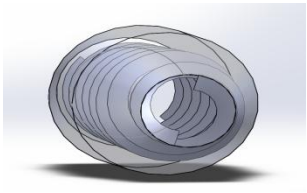

Figure 4 Rear View

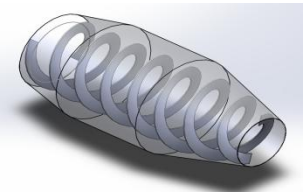

Figure 5 Isometric View

2.3 Simulation Scheme

EDEM is a high-performance CAE software based on the Discrete Element Method (DEM), which mainly consists of three components: the pre-processing module, the solver, and the post-processing module. EDEM is equipped with an extensive library of pre-calibrated material models, which allows for quick and easy initiation of simulations and can represent a variety of materials such as rocks, ores, soils, and powders. It features fast and scalable computational performance on CPU, GPU, and multi-GPU solvers, enabling the simulation of large and complex particle systems containing millions or tens of millions of particles. Additionally, custom physical settings can be implemented via EDEM's API for complex simulations and advanced material behaviors, including wet coating, agglomeration, breakage, and magnetic particles.

In the pre-processing module, it is necessary to convert the Concrete Mixing Drum model drawn in Section 2.1 into STL format for import, and establish the coordinate system and global units[6]. In EDEM, particle models can be imported from external sources, and the built-in particle factory can also be used to quickly and easily create corresponding solid particles.[6] Since concrete is a fluid-like material composed of cementitious materials, aggregates, cement, and admixtures, two models—Hertz-Mindlin (no slip) and Hertz-Mindlin with JKR (high cohesiveness)—need to be used in particle modeling to represent concrete particles and aggregates respectively[7]. The JKR model can accurately simulate the bonding between cement paste and aggregates, avoiding the distorted result of "excessive particle dispersion" caused by neglecting cohesion. This enables more reliable optimization of process parameters such as Concrete Mixing Drum rotational speed and pumping pressure, thereby reducing the cost of experimental trial and error[7].The contact parameters are shown in Tables 2-3.The concrete particle properties are shown in Figure 6.

Table 2 Settings of Material Properties and Contact Parameters

Material	Density /(kg·m^{-1})	Shear Modulus /(10^{9}Pa)	Poisson's Ratio
Aggregate	1450	20	0.35
Cement	1400	70	0.3
Steel	7850	29	0.25

Table 3 Contact Parameter Settings

Contact Pair	Coefficient of	Coefficient of Static	Coefficient of Kinetic
Steel-Steel Contact	0.2	0.01	0.700
Aggregate-Aggregate Contact	0.7	0.30	0.200
Cement-Cement Contact	0.7	0.20	0.010
Steel-Aggregate	0.6	0.10	0.030

Contact			
Steel-Cement Contact	0.5	0.35	0.025
Aggregate-Cement Contact	0.8	0.35	0.015

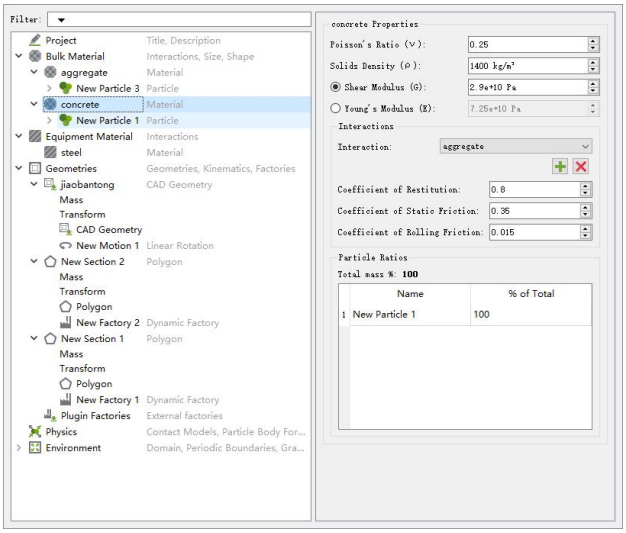

Figure 6 Concrete Particle Properties

To Facilitate Calculation, the radius of cement particles is set to 0.01 meters, as shown in Figure 7.

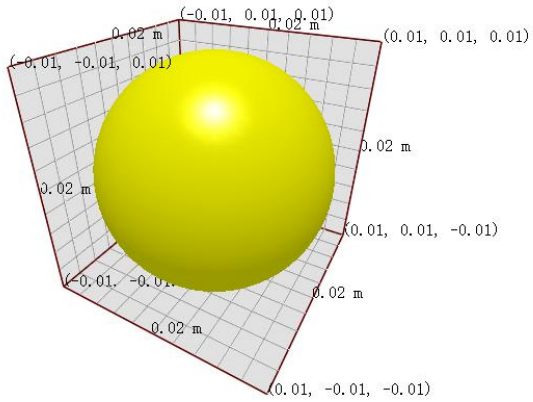

Figure 7 Properties of Cement Particles

Since concrete exhibits fluid-like behavior, it is necessary to additionally set the properties of two models—Hertz-Mindlin (no slip) and Hertz-Mindlin with JKR (high cohesiveness)—when configuring particles, as shown in Figure 8.

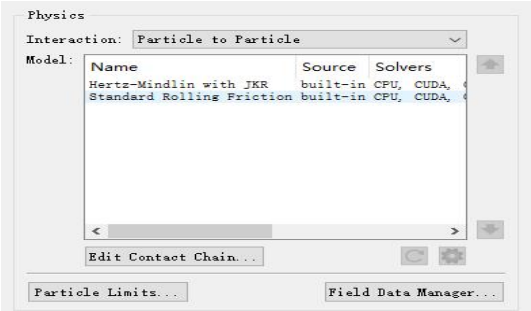

Figure 8 JKR Model

As a key component of concrete, aggregates typically account for three-fourths of the concrete volume and exert a significant impact on concrete strength; common coarse aggregates include pebbles and crushed stones, while common fine aggregates include natural sand and manufactured sand[8]. During the particle modeling of aggregates, establishing multi-morphology aggregates would incur enormous computational costs in subsequent steps, so to facilitate calculation, the aggregate particle model in this paper is simply set as a single spherical model with a radius of 0.07 meters, and the aggregate properties are shown in Figure 9. From the perspective of concrete performance, the interface bonding state between aggregates and cement paste during the mixing process is one of the core factors determining concrete strength. If mixing is insufficient, the aggregate surfaces will not be uniformly coated with cement paste, leading to the formation of weak interface zones and a subsequent decrease in the compressive and tensile strengths of concrete[9]. Conversely, sufficient mixing enables tight bonding between aggregates and cement paste, which fully exerts the "skeletal support" effect of aggregates and enhances the mechanical properties of concrete. In addition, the water absorption of aggregates also affects the workability of concrete during the mixing process: aggregates with high water absorption (such as natural sand) will absorb water from the cement paste during mixing. If the water dosage is not adjusted in advance, it will easily cause a decrease in concrete slump, thereby affecting the simulation results.

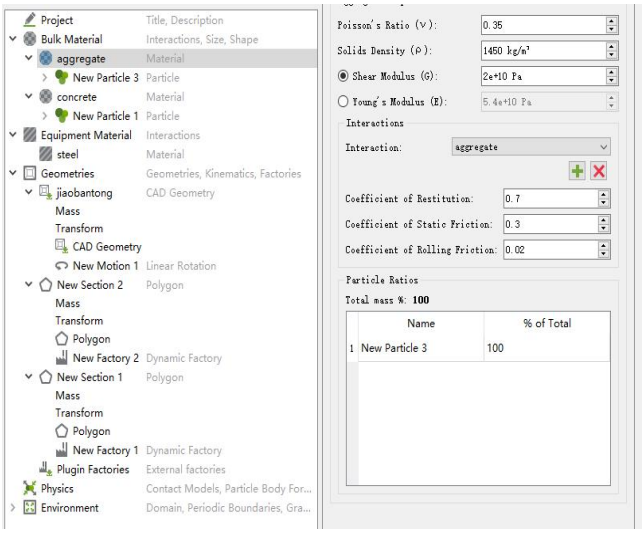

Figure 9 Aggregate Particle Properties

The particle model of aggregates is shown in Figure 10.

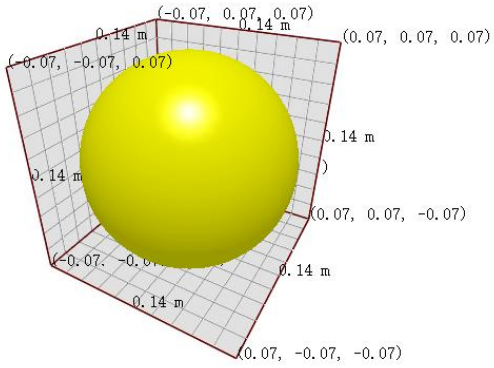

Figure 10 Aggregate Particle Model

2.4 Hertz-Mindlin with JKR Contact Model

The Hertz-Mindlin with JKR contact model is a complex yet accurate model in EDEM, mainly used to account for contact scenarios involving surface energy and adhesive effects. Since concrete exhibits fluid-like behavior, the JKR model can better simulate real concrete for simulation purposes.The normal contact force of this model consists of three components: Hertz elastic force, JKR adhesive force, and normal damping force[10]. The relationship is as follows.

$$F_n = F_n^H + F_n^{JKR} + F_n^d \tag{1}$$

$$F_n^H = \frac{4}{3} E^* \sqrt{R^*} \delta_n^{3/2} \tag{2}$$

In Equation (2), F_n^H denotes the normal contact force, E*represents the equivalent elastic modulus, and R^* stands for the equivalent contact radius[11]. For two spherical particles, the relationship between R* and R (particle radius) is as follows.

$$\frac{1}{R^*} = \frac{1}{R_1} + \frac{1}{R_2} \tag{3}$$

Among them, R_1 and R_2 are the radii of the two particles. When the surface energy is 0, the normal force in Equation (2) becomes the Hertz normal contact force[12].

$$F_{\text{Hertz}} = \frac{4}{3} E^* \sqrt{R^*} \delta^{\frac{3}{2}} \tag{4}$$

In the JKR model, an attractive cohesive force can be provided even when there is no direct contact between two particles. This force is calculated using Equations (5) and (6).

$$\delta_c = \frac{\alpha_c^2}{R^*} - \sqrt{\frac{4\pi\gamma\alpha_c}{E^*}} \tag{5}$$

$$\alpha_c = \left[\frac{9\pi\gamma R^{*2}}{2E^*} \left(\frac{3}{4} - \frac{1}{\sqrt{2}} \right) \right]^{\frac{1}{3}} \tag{6}$$

When the gap between particles is large or there is no contact, the normal force is zero, while a maximum cohesive force exists. Its expression is as follows.

$$F_{\text{pullout}} = -\frac{3}{2} \pi\gamma R^* \tag{7}$$

In Equation (7), F_{pullout} represents the pullout force. The incorporation of the JKR model implies an increase in the computational complexity of the model, which results in significant performance consumption of the computer during large-scale model simulations[13].

2.5 Particle Factory

The core function of the EDEM Particle Factory is to quickly and accurately generate qualified particles for discrete element simulations, serving as a key tool for constructing simulation geometries and material models. In this paper, the Particle Factory was used to generate 10,000 kg and 12,000 kg of concrete, as well as concrete-aggregate mixtures with ratios of 1:1 and 1:2. Among them, Factory 1 is responsible for generating concrete particles, while Factory 2 is dedicated to producing aggregate particles, with both generating 200 kg of their respective materials per second. During the initial filling stage of the Concrete Mixing Drum, the Particle Factory was set to "dense packing mode" to optimize particle arrangement density through algorithms, simulating the natural compaction process of concrete under its own weight[14].

This process directly affects the initial contact stress distribution between particles and the drum wall, thereby altering the peak Lateral Force at the moment of mixing startup. The method adopted in this paper is to generate all particles first before rotating the Concrete Mixing Drum, which can avoid the impact of concrete on the peak Lateral Force at the startup moment.When generating particles using the Particle Factory in EDEM, it is essential to focus on multiple key factors to ensure the accuracy and computational efficiency of the simulation: The parameter configuration of particle physical properties should be defined based on specific simulation scenarios, covering key indicators such as density, elastic modulus, and Poisson's ratio that match the characteristics of actual materials, so as to ensure that the particle properties are highly consistent with those of real materials. The particle generation parameters need to be scientifically set: the generation rate should be adapted to the filling sequence of equipment such as the Concrete Mixing Drum to avoid abnormal particle

accumulation caused by excessively high rates or prolonged simulation cycles due to excessively low rates; the particle size and its distribution must strictly conform to the gradation characteristics of actual materials; if a single spherical model is adopted, verification is required to ensure that the particle size selection balances computational accuracy and solution efficiency.

The settings of the Particle Factory are shown in Figures 11-12.

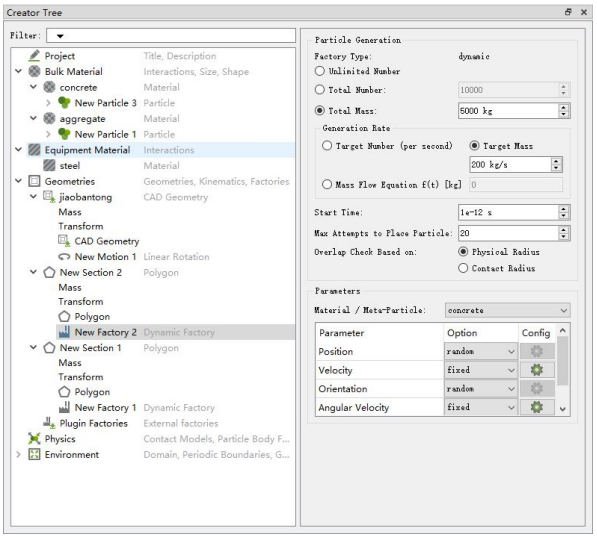

Figure 11 Concrete Particle Factory

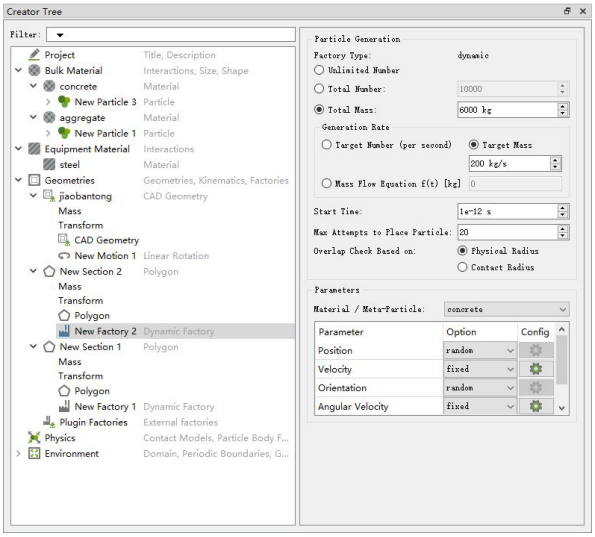

Figure 12 Aggregate Particle Factory

According to the GB/T 26408-2020 standard, the maximum Rotational Speed of the mixing drum of a concrete mixer truck is 18 rpm; the mixing speed during transportation is 1-3 rpm, 6-10 rpm during loading, and 3-14 rpm during unloading. Combined with practical scenarios, the Rotational Speeds of the Concrete Mixing Drum selected in this paper are 2 rpm, 5 rpm, and 10 rpm—among which 10 rpm is used to study the Lateral Force on the concrete mixer drum under extreme transportation conditions. The relationship between Rotational Speed and acceleration is shown in Equation (7)Aggregate Particle Factory

$$\omega = \frac{2\pi n}{60} \tag{8}$$

When the Concrete Mixing Drum rotates at 2 rpm, its angular velocity is approximately 0.209 rad/s when it rotates at 3 rpm, the angular velocity is about 0.524 rad/s and when it rotates at 10 rpm, the angular velocity is roughly 1.047 rad/s. The generated particles are shown in Figure 13.

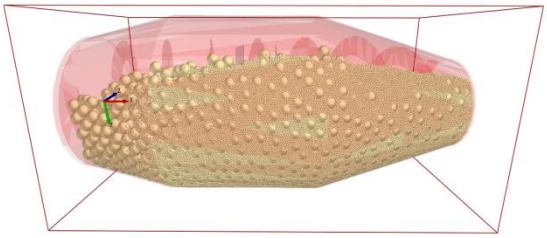

Figure 13 Particle Generation Diagram

The radii were set based on the central points at both ends of the Concrete Mixing Drum, and the initial Rotational Speed of the drum was configured. The total time required to generate particles is 30 seconds; to reduce the potential impact of the Concrete Mixing Drum's rotation on the peak Lateral Force during particle generation, the drum was set to start rotating only after 30 seconds.The rotational speed parameters are shown in Figure 14.

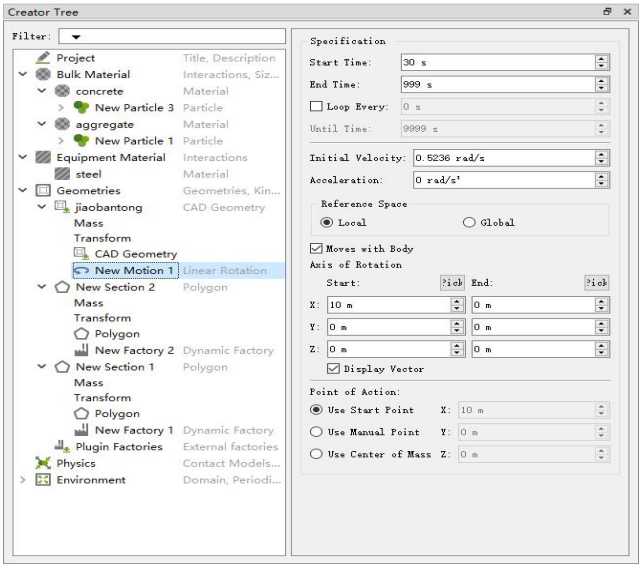

Figure 14 Rotational Speed Parameters

Since there are no restrictions on the rotation direction, the rotation direction selected in this paper is toward the inside of the screen, as shown in Figure 15.

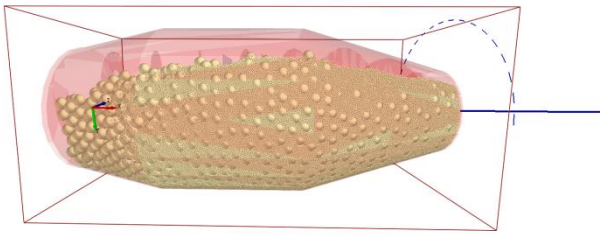

Figure 15 Rotation of the Concrete Mixing Drum

3 PROCESSING OF SIMULATION RESULTS

In the Simulator Settings, the time step was set to 20%, data was saved every 0.1 seconds, and the mesh division size was configured as 2.5R (Cell Size), with a total of 1,820,216 meshes divided. The simulation group parameters and results are shown in Table 4 and Figures 16-20.

Table 4 Simulation Group Parameters

Time/(s)	Concrete Aggregate Packing Ratio	Weight/(kg)	Rotational Speed/(rpm)
30-35	1:1	10000	10

35-40	1:1	10000	5
40-45	1:2	12000	2
45-50	1:1	12000	5
50-55	1:2	10000	2

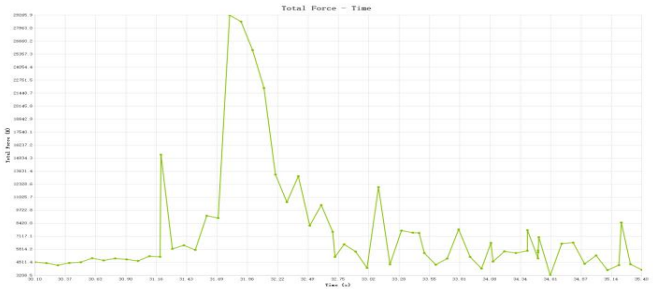

Figure 16 30-35 Seconds

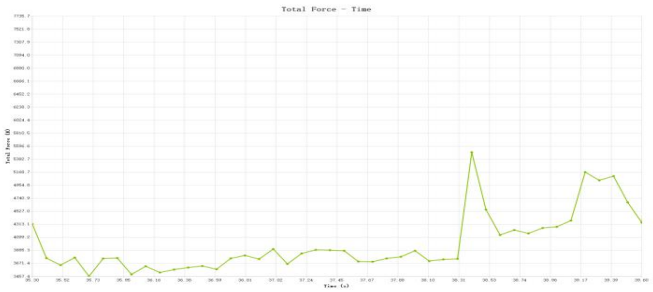

Figure 17 35-40 Seconds

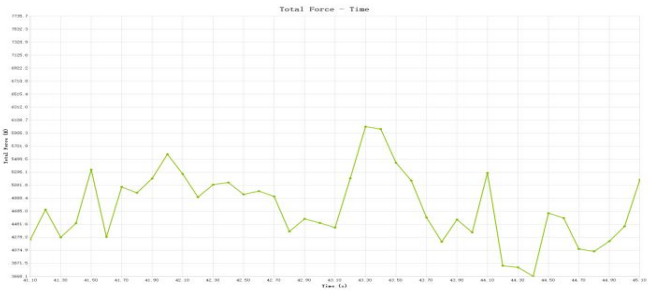

Figure 18 40-45 Seconds

Figure 19 45-50 Seconds

Figure 20 50-55 Seconds

4 CONCLUSIONS AND PROSPECTS

From the simulation results, it can be concluded that during the concrete mixing process of the concrete mixer truck, the different packing ratios of concrete and aggregate and the rotational speed of the mixing drum have a significant impact on the lateral force.

1.The simulation results show that when the mass ratio of concrete to aggregate is 1:1 (with a total mass of 10,000 kg) and the rotational speed of the mixing drum is 10 rpm, the peak lateral force exceeds 29,000 N.

2.When the mass ratio of concrete to aggregate is 1:1, the average lateral force is approximately 4,500 N at a rotational speed of 2 rpm; when the rotational speed increases to 5 rpm, the average lateral force can reach 5,500 N. It can be concluded that the faster the rotational speed, the greater the lateral force on the mixing drum, and the greater the threat to the driving safety of the mixer truck.

3.When the rotational speed of the mixing drum is consistently 2 rpm, the peak lateral force in the case of a 1:2 concrete-to-aggregate packing ratio (with a total mass of 10,000 kg) is more than 10,000 N higher than that in the case of a 1:1 packing ratio (with a total mass of 12,000 kg). It can be concluded that the higher the packing ratio, the greater its impact on the lateral force.

4.In this study, the assumed models of concrete spheres and aggregates are ideal spheres. Considering that factors such as the shape and size differences of material particles will affect the simulation results, it may not be possible to obtain highly accurate results. Future research needs to develop more optimization algorithms to improve the accuracy of simulation results.

COMPETING INTERESTS

The authors have no relevant financial or non-financial interests to disclose.

REFERENCE

[1] Deng R, Tan Y, Zhang H, et al. Numerical study on the discharging homogeneity of fresh concrete in truck mixer: Effect of motion parameters. Particulate Science and Technology, 2018, 36(2): 146-153.

[2] Yang J, An Q. Mechanics analysis for the main bearing of the rotating drum in the concrete mixing truck. Journal of the Brazilian Society of Mechanical Sciences and Engineering, 2018, 40(6): 1-14.

[3] Fedorko G, Kral J, Kral J, et al. Determination of Calculation for the Shape of Blades Trace in the Concrete Mixer Truck. Procedia Technology, 2015, 19, 395-401. DOI: https://doi.org/10.1016/j.protcy.2015.02.056.

[4] Peng J, Shen H, Ding W, et al. Research and analysis of conveyor separation mechanism of light and simple sweet potato combine harvester based on EDEM discrete element method. Computational Particle Mechanics, 2025, 1-18. DOI: 10.1007/S40571-025-01031-X.

[5] Ou M, Wang G, Lu Y, et al. Structure Optimization and Performance Simulation of a Double-Disc Fertilizer Spreader Based on EDEM-CFD. Agronomy, 2025, 15(5): 1025-1025.

[6] Song S, Zhu S, Wang J, et al. Disturbance analysis of shield tunneling in clay and limestone composite strata using EDEM simulation. Scientific Reports, 2025, 15(1): 12616-12616.

[7] Zhao Z, Hou J, Guo P, et al. Analysis of Soil–Straw Movement Behavior in Saline–Alkali Soil Under Dual-Axis Rotary Tillage Based on EDEM. Agriculture, 2025, 15(3): 337-337.

[8] Gong Y, Yu C, Zhang Z, et al. Enhancement of recycled coarse aggregate concrete properties using a combined adjustable cement slurry coating and mixing approach. Construction and Building Materials, 2025, 491, 142634-142634.

[9] Wang X, Zhang Y, Zhang W, et al. Research on improving the performance and mechanism of manufactured sand concrete based on vibration-coupled mixing. Journal of Building Engineering, 2025, 108, 112971-112971.

[10] Jiang D, Soroush M, Yi B, et al. Modeling mixing kinetics for large-scale production of Ultra-High-Performance Concrete: effects of temperature, volume, and mixing method. Construction and Building Materials, 2023, 397. DOI: https://doi.org/10.1016/j.conbuildmat.2023.132439.
[11] Guodong C, Lide L, Shiguo L, et al. Numerical flow simulation of fresh concrete in mixing truck. Powder Technology, 2022, 409. DOI: https://doi.org/10.1016/j.powtec.2022.117781.
[12] Cristian F, Nicolò B. Mixing Phase Study of a Concrete Truck Mixer via CFD Multiphase Approach. Journal of Engineering Mechanics, 2022, 148(3). DOI: https://doi.org/10.1061/(ASCE)EM.1943-7889.0002042.
[13] Yuanqiang T, Rong D, Hao Z, et al. Study of mixing and discharging of dry particles in a truck mixer. Particulate Science and Technology, 2020, 38(3): 271-285.
[14] Deng R, Tan Y, Zhang H, et al. Experimental and DEM studies on the transition of axial segregation in a truck mixer. Powder Technology, 2016, 314, 148-163.

Eurasia Journal of Science and Technology
Print ISSN: 2663-1024
Online ISSN: 2663-1016
DOI: https://doi.org/10.61784/ejst3110

THE CORRELATION BETWEEN LIFESTYLE AND PREVALENCE OF HIP JOINT DISEASE IN PLATEAU AREAS

JianCheng Li*, Peng Zhou, KaiZhao Pang, JiRong Li
Department of Orthopedics, Qinghai Kangle Hospital, Xining 810000, Qinghai, China.
Corresponding Author: JianCheng Li, Email: doctorcheng2013@163.com

Abstract: This study systematically analyzed the relationship between lifestyle habits and the incidence of hip joint disease in high-altitude areas, focusing specifically on the mechanisms by which factors such as low oxygen levels, strong ultraviolet radiation, traditional infant swaddling methods, and unique walking patterns influence hip joint health. This study provides a scientific basis for the prevention and control of hip joint disease in high-altitude areas.
Keywords: Plateau area; Prevalence of hip arthritis; Relevance

1 INTRODUCTION

Hip disorders severely impact patients' quality of life and encompass a wide range of conditions, including developmental dysplasia of the hip (DDH), osteoarthritis (OA), and avascular necrosis of the femoral head. Population growth and the increasingly aging population in high-altitude regions worldwide have made hip disease a growing concern in these high-altitude areas. The unique geographical and cultural characteristics of these plateaus, such as low oxygen levels, intense ultraviolet radiation, and distinct lifestyles and customs, can profoundly impact hip health. According to statistics, approximately 500 million people worldwide live permanently at altitudes above 1,500 meters. This is particularly true of China's Qinghai-Tibet region Plateau, the world's highest and largest plateau, with an average elevation exceeding 4,000 meters and home to approximately 5 million Tibet region ans. The epidemiological characteristics of hip disease in these regions and its association with lifestyle have become a key research topic in orthopedics and public health.

2 EPIDEMIOLOGICAL CHARACTERISTICS OF HIP ARTHRITIS IN PLATEAU AREAS

2.1 Prevalence of Developmental Dysplasia of the Hip (DDH)

Developmental dysplasia of the hip (DDH) is a common childhood condition, particularly in high-altitude areas. A 2019 study in Shigatse, Tibet region , China, found a prevalence of DDH of 174.9‰ (106/606) among 606 infants aged 0-6 months. This rate was significantly higher than reported data from the plains. Interestingly, the study demonstrated a significant positive correlation between the prevalence of DDH and altitude (r=0.82, P=0.004). This suggests that the incidence of DDH increases with increasing altitude [1]. This finding was further validated in subsequent studies. A 2021 survey showed an average prevalence of DDH of approximately 32.4‰ in Shigatse, Tibet region . Unilateral cases were more common than bilateral cases, with the ratio of right to left being 1.00:2.06.
Meanwhile, a study conducted in Luoma Township, Seni District, Nagqu City, Tibet region Autonomous Region, revealed that the prevalence of knee osteoarthritis was 36.1%, while hand osteoarthritis reached 50.5%. Furthermore, rheumatoid arthritis accounted for 4.4%, slightly higher than other relevant data from China and abroad (0.18% to 1.07%). These data indicate that, particularly in the Qinghai-Tibet region Plateau, the incidence of hip and other joint diseases is generally higher than in the plains.

2.2 Epidemiology of Hip Fracture and Osteoarthritis

Hip fractures are a common hip disease and have unique epidemiological characteristics in high-altitude areas. A study of hip fracture incidence at different altitudes in Norway found that women living at higher altitudes had a significantly increased risk of hip fracture (IRR = 1.04, 95% CI: 1.02, 1.05), while men showed no significant difference. The study also showed that the risk of hip fracture increases with distance from the coast. The data showed that women who lived farther from the coast had a higher risk of hip fracture (relative risk ratio = 1.04, 95% confidence interval: 1.02 to 1.06).
A study of the Peruvian highland city of Juliaca (at an altitude of approximately 3,800 meters) revealed a prevalence of hip osteoarthritis of 0.37% among residents. A Japanese study showed that the prevalence of radiographic hip osteoarthritis in the general population was 1.1% in men and 0.9% in women [2], while in rural areas, the prevalence was 0.59%. Although comparisons of prevalence rates across studies require caution, these data suggest that the prevalence of hip osteoarthritis in highland areas may differ from that in lowland areas.

3 ASSOCIATION MECHANISM BETWEEN PLATEAU ENVIRONMENTAL FACTORS AND HIP JOINT DISEASE

3.1 Effects of Hypoxic Environment on Hip Joint Health

3.1.1 Effects of hypoxia on hip joint blood circulation

Low oxygen levels at high altitudes are one of the main factors affecting hip joint health. Studies have shown that low oxygen levels trigger the kidneys to release angiotensin II and vasopressin, increasing blood volume and cardiac output to ensure adequate oxygen supply to tissues. However, this compensatory mechanism can cause blood to become more viscous, increasing the risk of blood clots and thus affecting blood flow in the hip joint area.

A research team from Peking University, studying the effects of high altitude on human hemodynamics, found that in the initial stages of acute high altitude exposure, the subjects' diastolic blood pressure (DBP) increased significantly by 11%, their stroke volume (SV) decreased by 17% [3], and their subendocardial myocardial viability ratio (SEVR) decreased by 19%. These changes indicate an imbalance in myocardial oxygen supply and demand. While this study focused on cardiac function, it also indirectly revealed adaptive changes in systemic blood circulation under hypoxic conditions, which may also affect blood flow in the hip joint area.

Research by the Human Phenome Research Institute at Fudan University has further demonstrated that low-pressure, low-oxygen environments can trigger functional problems in the vascular endothelium, which is closely linked to dysregulation of energy metabolism. Under hypoxic conditions, glycolysis in endothelial cells increases, while oxidative phosphorylation decreases, leading to the production of a large amount of lactate. This lactate promotes the lactylation of PKM2 [4], preventing its degradation, leading to dysregulation of endothelial energy metabolism and worsening endothelial dysfunction. This endothelial dysfunction may adversely affect nutrient delivery to the cartilage and bone tissue of the hip joint, thereby promoting the development and progression of hip joint disease.

3.1.2 Hypoxia and avascular necrosis of the femoral head

Multiple studies have demonstrated a link between oxygen-deficient environments and avascular necrosis of the femoral head. Studies have shown that in SD rats treated with glucocorticoids, hypoxia exacerbates femoral head necrosis in the presence of sustained hypoxia (simulating an altitude of 4,000 meters) [5]. This phenomenon is closely linked to a hypercoagulable state and increased thrombosis.

A study investigating the hidden blood loss associated with intertrochanteric fractures in patients living at high altitudes found that hypoxia may be an independent risk factor for increased blood loss in elderly patients with intertrochanteric fractures at high altitudes. This suggests that hypoxia may alter blood flow characteristics, increasing the risk of thrombosis in blood vessels near the hip joint, thereby affecting blood supply to the femoral head and ultimately causing avascular necrosis.

The circumflex branches of the femoral artery, particularly the medial retinaculum, supply blood to the hip head, with the medial retinaculum responsible for approximately two-thirds of blood flow. In an oxygen-poor environment, these vessels are more susceptible to spasm, narrowing, or thrombosis, leading to localized blood deficiency in the femoral head and potentially avascular necrosis.

3.1.3 Effects of hypoxia on hip cartilage metabolism

An oxygen-deficient environment may promote the progression of hip joint disease by altering chondrocyte metabolism. Studies have shown that moderate levels of reactive oxygen species (ROS) can support essential cellular functions, such as promoting chondrocyte proliferation and cartilage matrix remodeling [6]. However, excessive ROS accumulation can lead to oxidative stress, triggering cell aging, loss of differentiation, and death, and promoting an increase in matrix-degrading enzymes, leading to cartilage matrix destruction.

In oxygen-deficient conditions, chondrocytes may experience increased oxidative stress. A research team from Soochow University found that by enhancing the antioxidant capacity of chondrocytes, for example by increasing the expression of SOD3, they could effectively alleviate cartilage degradation, restore the balance between anabolism and degradation, and thus improve athletic performance. This demonstrates the importance of the antioxidant defense system under hypoxic conditions and the potential role of oxidative stress in the development of hip joint disease at high altitudes.

3.2 Impact of Strong Ultraviolet Radiation on Hip Joint Health

3.2.1 Direct damage to articular cartilage caused by ultraviolet radiation

Intense ultraviolet radiation at high altitudes is a key environmental factor affecting hip joint health. Studies have shown that ultraviolet radiation can directly damage skin and articular cartilage cells while stimulating the production of free radicals, leading to oxidative stress. Ultraviolet radiation can stimulate keratinocytes to produce large amounts of prostaglandin E2 (PGE2), which promotes the release of inflammatory mediators and further exacerbates inflammatory responses in joint tissue.

Studies of articular cartilage's UV absorption properties have shown that 365-nanometer UV rays are significantly attenuated as they pass through the cartilage, particularly in the cartilage's surface layer. This attenuation decreases with increasing depth [7]. This suggests that the surface cells of articular cartilage may be more susceptible to direct damage from UV radiation. Furthermore, studies have shown that intact cartilage sheets exhibit significant light absorption properties when exposed to UV radiation, particularly at wavelengths below 300 nm. These characteristics may explain why articular cartilage is more susceptible to degeneration after long-term exposure to strong UV radiation.

3.2.2 Ultraviolet radiation and oxidative stress

Oxidative stress caused by ultraviolet radiation is a key factor in the destruction of articular cartilage. Studies have shown that ultraviolet radiation can increase the concentration of reactive oxygen species (ROS) in chondrocytes, triggering oxidative stress and subsequently damaging DNA [8], proteins, and lipids within the cells. A study examining the impact of environmental factors on the inflammatory changes in articular tuberculosis found that the risk of articular tuberculosis in people who have lived at high altitudes for a long time is positively correlated with the intensity of ultraviolet radiation.

Selenium plays a key role in protecting against DNA damage caused by ultraviolet radiation. Studies have shown that selenium can offset the effects of DNA damage caused by UV radiation, such as by reducing DNA damage and enhancing DNA repair. In high-altitude environments with strong ultraviolet radiation, adequate supplementation of antioxidant nutrients such as selenium may help protect joint cartilage from damage.

3.2.3 Epidemiological evidence of ultraviolet radiation and hip joint diseases

Indirect evidence from epidemiological surveys suggests a possible link between UV radiation and hip problems. One study of residents at different altitudes in Ecuador found that UV radiation levels at altitudes between 2,800 and 3,000 meters were approximately 40% higher than those at lower altitudes. Intense UV exposure may increase the likelihood of oxidative damage to hip cartilage, thereby impacting hip joint health.

An orthopedic research team led by Professor Zhu Xuesong found that in articular cartilage, SOD3 (superoxide dismutase 3) expression increased, while APOE (apolipoprotein E) expression decreased. This suggests that enhancing cartilage's antioxidant capacity and restoring cholesterol balance may be crucial for preventing hip joint disease in high-altitude areas. This further supports the hypothesis that ultraviolet radiation may affect hip joint health through oxidative stress mechanisms.

3.3 Impact of the Special Lifestyle in Plateau Areas on the Hip Joint

3.3.1 Walking habits and hip joint load

The walking habits of residents in high-altitude areas have a significant impact on hip health. Research has found that the stress on the hip joint varies significantly depending on the slope of the walk. Hip torque increases significantly when walking uphill. While hip torque changes less during downhill walking, knee extension torque increases significantly. This may indicate that people who walk in high-altitude areas for a long time are more susceptible to hip and knee problems.

People living in mountainous areas and plateaus, due to long periods of walking on steep terrain, place greater stress on their knees and hips, making them more susceptible to joint degeneration. In contrast, people living in plains, where the terrain is flatter, experience less stress on the hip joints and are therefore less likely to develop joint problems. This difference may contribute to the higher incidence of hip joint problems in plateau areas.

A simulation study analyzed the forces acting on lower limb joints during weight-bearing walking at different inclines. The results showed that when walking uphill, the torques in almost all joints increased, and the load on the hip joint also increased with increasing incline. For instance, at a 15-degree incline, the average hip joint torque measures 0.4693 Nm/kg, and the peak torque reaches 1.7221 Nm/kg, which is notably higher than the values observed at a 0-degree incline, where the average and peak torques are 0.3893 Nm/kg and 1.4880 Nm/kg, respectively. Based on these data, the complex terrain conditions in plateau areas may significantly increase the mechanical load on the hip joint, leading to faster wear and degeneration of articular cartilage.

3.3.2 Traditional clothing and joint protection

The traditional attire of plateau residents may affect hip joint health. Among Tibet region ans, long, open-fronted robes and riding boots are typical clothing styles, which, to some extent, expose joints more readily. In low temperatures, exposed joints can cause local blood circulation impairment and increased muscle tension, which can affect joint stability and function and increase the risk of hip problems.

In high-altitude areas, low temperatures may increase the viscosity of joint fluid and reduce the elasticity of surrounding joint tissues, thereby increasing friction and resistance during joint movement. Studies have shown that falling temperatures make joint fluid more viscous, increasing resistance to joint movement and potentially exacerbating cartilage wear. Therefore, the cold climate at high altitudes and traditional clothing practices may jointly affect hip joint health.

3.3.3 Impact of religious activities such as circumambulation

Religious practices such as circumambulation, performed by ethnic groups like Tibet region ans in high-altitude areas, may affect hip health. Circumambulation involves repetitive hip rotation, and prolonged performance can cause fatigue and chronic damage to the soft tissue surrounding the hip joint. Standard hip rotation movements are generally harmless. However, training errors or pre-existing hip conditions can lead to soft tissue damage or hip dislocation.

Furthermore, the constant shift in the body's center of gravity and the repetitive rotation of the hip joint during prayer wheel rotation may increase shear stress on the hip cartilage, accelerating cartilage degeneration. For patients with congenital hip dysplasia or hip dislocation, performing hip rotations may exacerbate their condition or even lead to serious complications. Therefore, individuals at high risk of hip disease may need to adjust the style and intensity of their religious activities, such as prayer wheel rotation, while in the plateau.

3.4 Traditional Baby Swaddling and Hip Dysplasia

3.4.1 Traditional Tibet region an baby wrapping methods

Traditional Tibet region an infant swaddling has a significant impact on hip formation. In Shigatse, Tibet region , infants are traditionally swaddled, where their legs are tied together for up to two months. Studies have shown a strong link between this swaddling method and the development of developmental dysplasia of the hip (DDH).

A study showed that all infants diagnosed with developmental dysplasia of the hip (DDH) in the Shigatse region of Tibet region had been wrapped with their legs tied for more than two months. Statistical analysis revealed a significant association between DDH and wrapping the hips in extension ($P<0.001$). This suggests that traditional Tibet region an infant wrapping is a major environmental risk factor for developmental dysplasia of the hip.

3.4.2 Epidemiological Characteristics of DDH in the plateau area

Research conducted in the Shigatse region of Tibet region reveals that the average prevalence of developmental dysplasia of the hip (DDH) in this area is approximately 32.4 per 1,000 individuals. Unilateral cases surpass bilateral ones, with 33 instances affecting the right side and 68 affecting the left, resulting in a right-to-left ratio of 1.00 to 2.06. This prevalence is much higher than that in inland cities, suggesting that the occurrence of DDH in the plateau may be related to multiple factors.

Recent studies have reaffirmed this conclusion. A study published in 2019 reveals that the prevalence of DDH in the Shigatse region of Tibet region is approximately 174.9 per 1000 (106 out of 606), or around 17.5%. This figure is much higher than previously reported, which may be related to the research methods used, the number of samples, or regional differences. The study also revealed a significant positive correlation: there was a positive correlation between altitude and the prevalence of DDH ($r=0.82$, $P=0.004$), which means that plateau areas may be an independent risk factor for DDH.

3.4.3 Interaction between infant wrapping method and altitude

Studies have shown that swaddling method and altitude may jointly influence the incidence of DDH. In the Shigatse region of Tibet region , studies have shown a significant correlation between the incidence of DDH and the local altitude ($r=0.820$, $P=0.046$). Furthermore, swaddling with the legs tied was also significantly associated with the incidence of DDH ($P=0.0017$). This suggests that using traditional infant swaddling methods at high altitudes may have a greater negative impact on hip development.

A study of Tibet region an infants revealed significant associations between altitude, leg-binding wrapping, nomadic lifestyle, and breech presentation and the development of DDH. Leg-binding wrapping was identified as a major environmental risk factor for DDH. These findings highlight the crucial role of changes in traditional infant wrapping methods in preventing DDH at high altitudes.

4 CHARACTERISTICS OF HIP JOINT DISEASE IN DIFFERENT POPULATIONS IN PLATEAU AREAS

4.1 Hip Dysplasia in Tibet Region an Infants and Children

Tibet region an infants and young children are at high risk of developmental dysplasia of the hip. Studies have shown that the incidence of DDH in Tibet region an infants is significantly higher than that in infants of Han and other ethnic groups. In the Xigaze region of Tibet region , the prevalence of DDH reaches 174.9 per 1,000 (106 out of 606), equating to approximately 17.5%. In contrast, urban areas in mainland China typically experience a DDH prevalence rate ranging between 1 to 2 per 1,000.

Developmental dysplasia of the hip (DDH) in Tibet region an infants is influenced by a combination of factors. The traditional Tibet region an practice of leg binding and wrapping is a significant environmental risk factor. Furthermore, studies have revealed a significant positive correlation between altitude and the prevalence of DDH ($r=0.82$, $P=0.004$), suggesting that the high-altitude environment itself may increase the risk of DDH. Furthermore, breech delivery is considered a risk factor for developmental dysplasia of the hip in Tibet region an infants ($P=0.0082$).

Tibet region an infants with developmental dysplasia of the hip (DDH) often exhibit unique clinical features. Studies have shown that DDH is more common on the left side of the body in Tibet region an infants, with a ratio of 1:2.06. This finding may be related to the delivery method used by Tibet region an women, the position of the fetus in the womb, or traditional swaddling practices, and warrants further investigation.

4.2 Hip Joint Diseases in Tibet Region an Adults

Hip joint problems in Tibet region an adults present with unique manifestations. A survey conducted in Luoma Township, Seni District, Nagqu City, Tibet region Autonomous Region, revealed a prevalence of knee osteoarthritis of 36.1% and a prevalence of 50.5% in finger joints. The survey found that the distal interphalangeal joints and carpometacarpal joints of the thumb were particularly common, while the proximal interphalangeal joints of the little finger were particularly prone to deformity. While the study focused on the knee and hand joints, it also revealed the prevalence of joint problems in the plateau region.

Studies have shown that sustained hypoxic conditions or environments may increase the incidence of avascular necrosis

of the femoral head. In conditions simulating the long-term hypoxic environment of 4,000 meters above sea level, SD rats treated with glucocorticoids experienced worsening femoral head necrosis. This condition is associated with increased hypercoagulability and thrombosis. This finding may, to some extent, explain the frequent occurrence of avascular necrosis of the femoral head in high-altitude areas.

Hip diseases among adult Tibet region ans are related to their occupation and lifestyle. Tibet region ans who engage in manual labor, particularly herders and farmers, often engage in weight-bearing activities, which leads to a higher incidence of hip degenerative disease. Prolonged standing, walking, and repetitive movements such as bending over can put constant pressure and wear on the hip joint, increasing the risk of degenerative disease.

4.3 Changes in Hip Joint Health among People Migrating to the Plateau

Studying changes in hip health among people who migrate to high altitudes is a topic of great research interest. Studies have shown that the risk of hip problems may change when people move from low-altitude to high-altitude areas. Oxygen deprivation may increase the risk of avascular necrosis of the femoral head. Furthermore, migrants may maintain their existing lifestyles, and these habits can interact with the high-altitude environment, impacting hip health.

Research has shown that after long-term acclimatization to the low oxygen and low pressure conditions of high altitude, the body and structure undergo a series of adjustments. After prolonged exposure to high-altitude hypoxia, red blood cell count increases to improve oxygen delivery. This adaptive change may affect blood flow and metabolism in the hip, impacting hip joint health. When these individuals return to the plains, the increased red blood cell count may trigger oxidative stress damage, resulting in symptoms such as dizziness, drowsiness, and fatigue. This phenomenon is known as "altitude deacclimatization."

However, there is currently little research on changes in hip health in people who migrate to the plateau. Future studies could further analyze the specific impacts of environmental and genetic factors on the development of hip disease by comparing the incidence of hip disease in people who have lived in the plateau for a long time, those who have recently moved to the plateau, and those who have previously migrated to the plains.

5 PREVENTION AND TREATMENT STRATEGIES FOR HIP JOINT DISEASE IN PLATEAU AREAS

5.1 Prevention and Intervention of Infantile Developmental Dysplasia of the Hip

To address the high incidence of DDH in Tibet region an infants, implementing preventive measures and timely early intervention are extremely critical. Based on existing research results, the following measures are recommended:

First, changing the conventional infant wrapping method is key to preventing DDH. Studies have shown that DDH in Tibet region an infants is primarily affected by the way the legs are tied and wrapped, a significant environmental risk factor. It is recommended that the hip-abduction wrapping technique be promoted to prevent the forced straightening and closing of the infant's legs, thereby supporting healthy hip development.

Furthermore, it is crucial to establish DDH screening programs for infants in high-altitude areas. The study recommends that government-level measures be taken to establish programs to screen high-risk infants for developmental dysplasia of the hip. This study, for the first time, reveals the high prevalence and influencing factors of DDH in Tibet region ans living at high altitudes, providing important insights for the formulation and management of relevant policies.

Third, we should increase training for medical staff in high-altitude areas to improve their skills in early recognition and diagnosis of DDH. Early recognition and treatment of DDH are crucial for improving prognosis, so improving the awareness and professional capabilities of primary health care workers is a key step in prevention and treatment.

Finally, we need to organize health education activities to raise awareness of the dangers of DDH among Tibet region an families and guide them to change traditional habits that are detrimental to hip health. Research has shown that increasing public understanding of DDH and implementing behavioral interventions can effectively reduce the incidence of the disease.

5.2 Protective Measures for Hip Arthritis Related to High Altitude Hypoxia

In response to the impact of the plateau hypoxic environment on hip joint health, the following protective measures can be taken:

First, promoting blood flow in the hip joint area is key. Studies have shown that an oxygen-deficient environment can cause blood to become more viscous, increasing the risk of blood clots and negatively impacting blood flow to the hip joint. Therefore, moderate exercise, adequate hydration, and avoiding prolonged sitting can help promote blood circulation and reduce the risk of hip joint disease.

Furthermore, improving antioxidant defenses may help mitigate damage to the hip joint caused by hypoxia and UV radiation. Studies have shown that trace elements such as selenium can protect cells from UV-induced DNA damage by reducing DNA damage and enhancing DNA repair capacity. Therefore, increasing antioxidant intake may help improve hip joint health in residents of high-altitude areas.

Third, appropriate protective equipment, such as hip braces, can be used to reduce the stress on the hip joint while walking and working. Studies have shown that people who walk on steep mountain roads for long periods of time experience increased stress on their hip joints, and wearing appropriate protective gear may be effective in reducing this

stress.
Finally, for high-risk groups, such as military personnel and herdsmen stationed in plateau areas for a long time, regular hip joint examinations are needed to detect and treat potential hip joint problems in a timely manner.

5.3 Interventions for Hip Arthritis Associated with Traditional Lifestyle

In view of the impact of traditional lifestyle in plateau areas on hip joint health, the following intervention measures can be taken:
First, adjusting infant swaddling techniques is crucial for preventing developmental dysplasia of the hip. Research clearly shows that the traditional Tibet region an method of swaddling the legs is a primary environmental factor contributing to DDH. Therefore, promoting scientific infant care methods that avoid excessive hip extension and adduction is crucial for preventing DDH.
Additionally, hip joint stress can be reduced by changing work and walking habits. Studies have shown that the load on the hip joint changes significantly with changes in slope during walking. During climbing, the rotational stress on the hip joint increases significantly. Walking downhill significantly increases knee extension force. Therefore, it is recommended that residents living in plateau areas slow down when ascending hills and use assistive devices to reduce hip joint stress. Protect your knees and prevent overextension when descending.
Third, improve hip joint stability by strengthening the hip muscles. Proper hip muscle training through appropriate activities can strengthen the muscles surrounding the joint, improve hip joint stability, and reduce pressure on the cartilage. For example, resistance training such as hip abduction and extension can be performed. However, excessive weight and strenuous exercise should be avoided.
Patients with hip problems should adopt a comprehensive treatment approach that includes physical therapy, medication, and surgery when needed. Studies have shown that for early-stage hip problems, non-surgical treatments such as reducing weight bearing, using medication, and physical therapy may be effective in slowing the progression of the disease.

6 CONCLUSION AND OUTLOOK

6.1 Main Research Conclusions

This study systematically analyzed the association between lifestyle and the prevalence of hip arthritis in plateau areas and drew the following main conclusions:
The incidence of hip joint diseases, especially developmental dysplasia of the hip (DDH), osteoarthritis, and avascular necrosis of the femoral head, increases significantly in high-altitude areas. In the Shigatse region of Tibet region , the prevalence of DDH reaches 174.9 per 1000 (106 out of 606), significantly higher compared to mainland cities.
2. Plateau environmental conditions are closely linked to the onset and progression of hip joint disorders. Hypoxic environments may impair blood circulation and energy metabolism in the hip joint, increasing the risk of avascular necrosis of the femoral head. Intense ultraviolet radiation may damage articular cartilage through oxidative stress. The unique topography and gait patterns of the plateau may increase mechanical stress on the hip joint, accelerating joint degeneration.
3. Traditional Tibet region an infant swaddling is a key environmental risk factor for DDH. Studies indicate that there is a significant association between tandem lower limb swaddling and the occurrence of DDH ($P<0.001$). Furthermore, there exists a notable positive correlation between altitude and the prevalence of DDH ($r=0.82$, $P=0.004$).
4. Hip problems vary significantly among different ethnic groups in high-altitude areas. Among Tibet region an infants, developmental dysplasia of the hip (DDH) is more common on the left side, with a left-right ratio of 1.00:2.06. Hip problems in Tibet region an adults are often closely related to their occupation and lifestyle.
5. For the prevention and treatment of hip joint diseases in plateau areas, multiple strategies should be adopted, including changing the traditional baby wrapping method, strengthening screening and early intervention, improving blood circulation in the hip joint, enhancing antioxidant defense mechanisms, and adjusting work and walking methods.

6.2 Research Limitations and Prospects

This study has several limitations. The current study was primarily cross-sectional in nature and lacked long-term observational data, making it difficult to establish causal relationships. Furthermore, differences in diagnostic criteria and methods used across studies preclude direct comparison of the results. Furthermore, the pathogenesis of hip joint disease in plateau regions remains largely unexplored, particularly regarding the specific mechanisms of action of hypoxia and ultraviolet radiation on hip cartilage and bone, which require further exploration.
Future research should focus on the following directions:
A large-scale and long-term follow-up cohort study should be conducted to clarify the incidence and risk factors of hip joint diseases in the plateau area and confirm their causal relationship.
2. Conduct detailed research on the mechanisms by which plateau climate conditions (e.g., low oxygen levels and strong ultraviolet radiation) affect hip cartilage and bone tissue, with a particular focus on changes in oxidative stress, apoptosis, and extracellular matrix metabolism.

3. Analyze how genetic and environmental factors interact to influence hip joint disease in the plateau region, with a particular focus on the genetic susceptibility of the Tibet region an population.
4. Conduct intervention studies to evaluate the effectiveness of strategies such as modifications to traditional infant swaddling practices and antioxidant supplementation in preventing hip disease.
5. Establish an early detection and intervention system for hip joint diseases in plateau areas to enhance the efficiency of prevention and treatment.
These studies help to deeply analyze the relationship between lifestyle and hip joint diseases in plateau areas, provide theoretical support for the formulation of special prevention and treatment measures, and thus improve the hip joint health of residents in plateau areas.

6.3 Policy Recommendations

Based on the findings of this study, the following policy recommendations are put forward:
1. Promote scientific infant care methods in high-altitude areas, especially changing the traditional leg-binding wrapping method to prevent developmental dysplasia of the hip (DDH).
2. Carry out infant hip screening programs in high-altitude areas to achieve early detection, timely diagnosis and effective treatment.
3. Strengthen training for primary medical personnel in plateau areas to improve their skills in identifying and managing hip joint diseases.
4. Organize health education activities to enhance the knowledge of hip joint health among residents in plateau areas and encourage them to improve bad living habits to maintain hip joint health.
5. Integrate hip joint health into the public health service system in plateau areas, carry out regular screening and follow-up, and form a long-term mechanism for the prevention and control of hip joint diseases.
6. Conduct research on hip joint diseases in plateau areas, paying special attention to the interaction between environmental and genetic factors, to provide a scientific basis for the prevention and treatment of diseases.
7. Provide hip joint protection advice to special occupational groups in plateau environments, such as soldiers and herdsmen, to reduce the risk of occupational hip injuries.
8. Strengthen the allocation of medical resources in plateau areas, improve the diagnosis and treatment capabilities of hip joint diseases, and especially popularize hip replacement surgery techniques.
These policy measures can effectively reduce the incidence and disability of hip joint diseases in plateau areas and improve the quality of life of local residents.

COMPETING INTERESTS

The authors have no relevant financial or non-financial interests to disclose.

REFERENCE

[1] Wei Y, Zhang L. High Altitude and Developmental Dysplasia of the Hip in Tibet region an Infants: A Population-Based Study. Journal of Pediatric Orthopaedics, 2020, 40(6): e456-e461.
[2] Glorieux M, Gupta R M. Hypoxia-Induced Vascular Dysfunction in Bone and Joint Disorders. Frontiers in Physiology, 2019, 10: 1234.
[3] Li H, Wang Q, Zhao Y. Ultraviolet Radiation and Oxidative Stress in Articular Cartilage: Mechanisms and Implications. Free Radical Biology and Medicine, 2021, 167: 1-10.
[4] Anderson J L, Parker J D. High-Altitude Hemodynamics and Their Impact on Joint Perfusion. Journal of High Altitude Medicine & Biology, 2018, 19(2): 105-112.
[5] Zhang X, Liu Y, Smith T R. Traditional Swaddling and Hip Dysplasia: A Cross-Cultural Comparison. The Lancet Child & Adolescent Health, 2019, 3(8): 556-564.
[6] Johnson A W, Clark M J. Epidemiology of Osteoarthritis in High-Altitude Populations: A Systematic Review. Arthritis Care & Research, 2017, 69(10): 1473-1481.
[7] Chen J, Li P. Genetic and Environmental Factors in Avascular Necrosis of the Femoral Head Among Tibet region an Populations. Journal of Orthopaedic Research, 2022, 40(3): 621-629.
[8] Martinez S, Lopez D. Impact of UV Radiation on Cartilage Degeneration: An Experimental Study. Photochemistry and Photobiology, 2020, 96(4): 832-839.

Eurasia Journal of Science and Technology
Print ISSN: 2663-1024
Online ISSN: 2663-1016
DOI: https://doi.org/10.61784/ejst3111

GROUP PHARMACOKINETICS OF FLUCONAZOLE IN PATIENTS WITH SEVERE INFECTION

Lu Yao[1,4#], Wei Bu[1,4#], Min Luo[1,4,5], Liu Shi[1,4], HongBo Xu[3], WenMei Liang[1], Yan Chen[3], Tao Chen[1], Bao Fu[1*], Lei Gong[1,2*]
[1]*Department of Critical Care Medicine, Affiliated Hospital of Zunyi Medical University, Zunyi 563000, Guizhou, China.*
[2]*Department of Pharmaceutics, Kweichow Moutai Hospital, Renhuai, Zunyi 563000, Guizhou, China.*
[3]*Guizhou Children's Hospital, Affiliated Hospital of Zunyi Medical University, Zunyi 563000, Guizhou, China.*
[4]*School of Pharmacy, Zunyi Medical University, Zunyi 563000, Guizhou, China.*
[5]*Zhijin County People's Hospital, Bijie 552102, Guizhou, China.*
[#]*Lu Yao and Wei Bu contributed equally to this work and they are both first authors.*
[*]*Bao Fu and Lei Gong contribute the same to the article and are the corresponding authors.*
Corresponding Author: Lei Gong, Email: gonglei28@126.com; Bao Fu, Email: fubao0607@126.com

Abstract: Objective: The aim was to investigate the population pharmacokinetics (PopPK) model of Vorticamole (VRC), identify significant covariates and corresponding dose optimization strategies in the existing clinical patient VRC PopPK model, and explore the characteristics of the existing VRC PopPK model. Methods: We searched the PubMed database for clinical PopPK studies of VRC using the nonlinear mixed-effects method from the establishment of the database to May 2025, and screened the relevant references. Results: A total of 29 studies that met the inclusion criteria were finally included. One-compartment and two-compartment models were reported in 21 and 7 studies, respectively, as the best models to describe the PopPK of VRC, and one study used a three-compartment model. More than 40 covariates were included in the screening, with the most common covariates being CYP2C19 phenotype and body weight, and ALB being a secondary covariate. The typical volume of distribution in adult and pediatric patients was similar, but the estimated clearance in pediatric patients was significantly higher than that in adult patients, and the estimated bioavailability in pediatric patients was significantly lower than that in adult patients. The typical values of voriconazole clearance and total apparent volume of distribution exhibit substantial variability, ranging from 2.29–7.35 L/h and 76–194 L, respectively. Twenty-four studies used the exponential model as the basic model to describe the inter-individual variation. Only three studies used external methods to evaluate the model. Conclusion: First, this paper emphasizes the broadness and variability of the estimated PopPK parameters of VRC and provides the covariates that affect the clearance and apparent volume of distribution in such patients. Second, external evaluation of PopPK models should be conducted, and the predictive performance of various models should be further compared to improve the extrapolation ability of the models. In addition, it is recommended to conduct Monte Carlo simulations based on the significant covariates derived from different patient groups, and to supplement PopPK models to guide the differences in clinical efficacy between dose and traditional empirical dose, track the individualized medication effects of patients guided by PopPK models, and conduct supplementary trials based on actual clinical efficacy to facilitate the more reasonable application of models in clinical practice.
Keywords: Voriconazole; Population pharmacokinetics; Exposure-response relationship

1 INTRODUCTION

Voriconazole (VRC) is a second generation triazole with broad spectrum antifungal activity [1].VRC has effective antibacterial activity against Aspergillus and Candida, as well as some clinically rare fungal pathogens [2]. It has effective activity against a wider range of clinically important fungal pathogens, including Aspergillus, Candida, Cryptococcus neoformans and some unusual organisms, such as Fusarium and Pseudobacter boydii. In 2016, the guidelines of the American Society of Infectious Diseases recommended VRC as the first choice for invasive aspergillosis and alternative therapy for candidiasis [3-4].

In recent years, many studies have studied the exposure-response relationship of VRC. The results of these studies show that low concentration may lead to higher treatment failure rate, while high concentration is related to increased toxicity. As a result, the target valley concentration range of VRC is narrow [5]. VRC is mainly metabolized by CYP2C19 isoenzymes in the human body, followed by CYP2C9 and CYP3A4 isoenzymes [6]. The CYP2C19 phenotype and its associated polymorphisms influence the metabolism of VRC by modulating enzyme expression, thereby contributing to its nonlinear pharmacokinetics. The lack of predictability in the relationship between pharmacokinetic characteristics and administered dosages may result in unpredictable pharmacological effects of VRC at standard doses, potentially leading to toxic effects [7].

The nonlinear kinetics observed for VRC partially accounts for its highly variable serum concentration. Additionally, there are substantial inter-individual and intra-individual differences in VRC pharmacokinetics, demonstrating extensive variability among different patient populations [8]. The binding affinity of VRC to proteins is moderate, approximately 60%, and its volume of distribution (Vd) ranges from 2 to 4.6 L/kg, suggesting extensive distribution both in

extracellular and intracellular compartments [9]. Although it has been observed that the pharmacokinetics of VRC exhibit relatively high inter-individual and intra-individual variability, and the therapeutic range of this compound is relatively narrow, the metabolic pathways and mechanisms of VRC have not yet been fully elucidated [10]. The third edition of the Aspergillosis Diagnosis and Treatment Guidelines in 2017 recommends that for the majority of patients receiving voriconazole for prophylaxis or treatment, the target trough concentration should be maintained at 1 - 5.5 μg/mL. For patients with severe infections, it is advisable to elevate the target trough concentration to 2 - 6 μg/mL [11]. The guideline for Individualized Use of voriconazole issued by the Chinese Pharmacological Society in 2018 recommended that the target trough concentration range of voriconazole is 0.5-5.0 μg/mL, which has good efficacy and low toxic and side effects [12]. In 2022, the Japanese Therapeutic Drug Surveillance Society's "Clinical Practice Guidelines for Voriconazole Therapeutic Drug Monitoring" suggested that the target trough concentration range for voriconazole in Asian patients should be set at 1.0–4.0 μg/mL. For non-Asian patients, the recommended trough concentration treatment range was established as 1.0–5.5 μg/mL [6]. In 2024, the European Leukemia Infection Conference updated the guidelines for antifungal prophylaxis in adults, which recommended voriconazole for the prevention of fungal infections in the range of 1.0-6.0 μg/mL [13]. The recommended concentration range of VRC is 0.5–5.0 μg/mL, as per the Chinese practice guidelines for its individualized use [12]. In conclusion, patients treated with voriconazole necessitate distinct therapeutic drug monitoring (TDM) indications, durations, and target trough concentrations, as well as individualized medication regimens to prevent drug exposure levels from exceeding the therapeutic range.

In clinical practice, TDM of VRC is recommended to enhance drug efficacy and minimize toxic and adverse effects [14]. However, the TDM method can only be applied subsequent to the initiation of treatment, and traditional TDM sampling is conducted under steady-state conditions. In practice, VRC achieves its steady-state trough concentration approximately 5 days following standard administration. Although a quasi-steady state may be attained within 24 hours post-administration, this still involves a waiting period that could potentially compromise clinical outcomes. In addition, VRC undergoes metabolism via cytochrome P450 isoenzymes, and the presence of inhibitors or inducers of these isoenzymes may alter the plasma concentration of VRC. This phenomenon also results in significant drug-drug interactions (DDIs) between VRC and co-administered medications during clinical application [15]. Therefore, the identification of factors contributing to a high degree of variation in the pharmacokinetics of VRC is crucial for determining an appropriate dosing regimen as early as possible.

In recent years, model-guided dose optimization has facilitated the advancement of individualized medicine into the quantitative decision-making phase. With the rapid evolution of quantitative pharmacological data analysis techniques, Population Pharmacokinetics (PopPK) modeling and simulation have assumed an increasingly critical role in precision medicine. By integrating PopPK models with TDM to optimize drug dosing regimens, it is possible to achieve covariate-based individualized drug administration [16]. Given the nonlinearity, significant inter- and intra-individual variability, extensive drug interactions, and relatively narrow therapeutic index of VRC, comprehending the pharmacokinetic characteristics in clinical patients receiving VRC is crucial for selecting appropriate antibiotic dosages and developing individualized treatment strategies [17]. For the development of individualized voriconazole dosing regimens, the guidelines recommend employing the PopPK method to adjust voriconazole dosing regimens when locally applicable population-based PopPK models are available [18]. In fact, over the past two decades, numerous scholars have been actively engaged in PopPK research on voriconazole. This review aims to consolidate the existing literature on VRC in clinical PopPK, thereby facilitating a comprehensive understanding of the current knowledge framework and paving the way for further research to enhance comprehension and inform optimal therapeutic dosing decisions.

2 METHODS

2.1 Methods of Retrieval

The PubMed database was systematically searched. The search time spanned from the establishment of the database to May 2025, and the search strategy was as follows: (((population pharmacokinetics) OR (PopPK) OR (nonlinear mixed-effect model) OR (PPK)) AND (voriconazole)). Search scope: All fields.

2.2 Inclusion and Exclusion Criteria

Studies included in this review were required to meet the following inclusion criteria: (1) the study population consisted of children, adult patients, or healthy volunteers; (2) VRC was administered as the study drug, regardless of whether it was given intravenously or orally; (3) a nonlinear mixed-effects PopPK modeling method was employed. Exclusion criteria included: (1) reviews and methodological articles; (2) laboratory-based or animal studies; (3) studies utilizing nonparametric methods.

3 RESULTS OF LITERATURE RETRIEVAL

3.1 Results of Literature Screening

After an initial search, 244 studies were retrieved from the Pubmed database. Following deduplication using Endnote

X9 software and manual screening, seven animal experiments and seven laboratory studies were excluded. Subsequently, after applying the inclusion and exclusion criteria, a total of 29 studies met the eligibility criteria, with publication years ranging from 2009 to 2025. No additional studies were identified following a review of the reference lists of the included studies. Table 1 summarizes the population characteristics of the 29 studies; the number of subjects in each study ranged from 13 to 305 (median: 95), and 21 studies (73%) included more than 50 participants. Eighteen of the studies focused on the Chinese population. There were 11 studies conducted on foreign populations, specifically in Thailand [7, 19], the United States[20, 21], the Czech Republic[9], the Netherlands [22], Japan [23], Australia [24], South Korea [25], Sweden [26], and Pakistan [27].

Table 1 Summary of Demographic Characteristics of the VRC Clinical PopPK Study

Study	country	CYP2C19 genotype (n)	Subjects /sample	Type of study	Structural model	Software	Age	Subject characteristics	Routes
Karlsson 2009[26]	Sweden	EMs:HEMs:PM=58:21:3	82/1274	perspicacity	2-CMT	NONMEM V	2-12	Paediatric patients	PO/IV
Han 2010[20]	America	NR	13	perspicacity	2-CMT	NONMEM 6.2.0	19-70	Adult lung transplant recipients	PO/IV
Han 2011[21]	America	NM:IM=11:2	13	perspicacity	1-CMT	NONMEM 6.2.0	41-67	Adult liver transplant recipient	PO/NFT
Dolton 2014[24]	Australia	NM and RM:IM and PM:UK =56:38:146	240/3352	NR	2-CMT	NONMEM 7.2	NR	Healthy adults (63) and adult patients with fungal infection (177)	PO/IV
Chen WY 2014[43]	China	NR	62/240	perspicacity	1-CMT	NONMEM VI	16-90	Critical adult patients with lung disease	IV
Muto 2015[23]	Japan	NM:PM:IM=9:2:10	39/276	NR	2-CMT	NONMEM 7	3-14	Immunocompromised children who were at high risk for systemic fungal infection	PO/IV
Li Z 2017[28]	China	RM:EM:IM:PM=2:24:25:5	56/125	retrospectivity	1-CMT	Phoenix NLME 1.4	18-60	Adult renal transplant recipients	PO/IV
Lin XB 2018[8]	China	RM:EM:IM:PM=1:44:49:12	105/342	perspicacity	1-CMT	Phoenix NLME 7.0	18-58	Adult renal transplant recipients	PO/IV
Kim 2019[25]	Korea	PM:EM:IM=48:75:70	193/1828	perspicacity	3-CMT	NONMEM 7.3	18-80	Healthy volunteers and patients	PO/IV
Chen C 2019[29]	China	CYP2C19*2:CYP2C19*3=13:5	23/121	retrospectivity	1-CMT	NONMEM 7.3.0	19-60	Haematopoietic stem cell transplant patients	PO/IV
Liu 2019[41]	China	NM:IM:PM=18:16:7	41/186	perspicacity	1-CMT	NONMEM 7.3.0	19-81	Patients with confirmed or suspected IFD haematological malignancy	PO
Tang 2019[44]	China	NR	57/166	perspicacity	1-CMT	NONMEM 7.3	27-80	Patients with liver dysfunction	PO/IV
Ren 2019[30]	China	UM:EM:IM:PM=1:61:80:18	180/NR	retrospectivity	1-CMT	Phoenix NLME 7.0	18-85	patient with cirrhosis of the liver	PO/IV
Khan-asa 2020[19]	Thailand	UM:EM:IM:PM=1:33:24:7	67/235	perspicacity	1-CMT	NONMEM	20-78	Adult haematological patients	PO
Tang 2021[38]	China	UM:EM:IM:PM=1:24:21:5	51/272	perspicacity	1-CMT	Phoenix NLME 8.0	15-89	Patients with liver dysfunction	PO/IV
Chantharit 2020[7]	Thailand	EM:IM:PM=40:36:12	106（12/60 perspicacity，		1-CMT	Phoenix 8.1	18-87	Patients with invasive Aspergillus	PO

			94/409 retrospectivity）					infections	
Lin XB 2022[40]	China	NM:IM:PM=12.11:3	26/297	perspicacity	2-CMT	Phoenix NLME 8.0	28-89	Critically ill patients with liver dysfunction	IV
Wang Jun 2021[37]	China	UM:EM:IM:PM=1:34:45:14	99/195	perspicacity	2-CMT	Phoenix NLME 8.2	0.4-13.58	Critically ill paediatric patients	IV
Wang T 2021[31]	China	NR	Cirrhosis group120/219; Non-cirrhotic group 11/83	retrospectivity	2-CMT	NONMEM 7.20	18-84	Patients with cirrhosis of the liver	PO/IV
Li SC 2021[32]	China	IM:NM:PM=32:27:16	78/427(VRC:214;VNO:213)	retrospectivity	1-CMT	Phoenix NLME8.2.0	14.0–70.0	Patients with impaired immune function	PO
Wu 2022[33]	China	EM:IM:PM=31:27:9	67/146	retrospectivity	1-CMT	NONMEM 7.4.3	5.5-14.71	Children with haematological malignancies	PO/IV
Jiang 2022[39]	China	EM:IM:PM=30:31:8	63/233	perspicacity	1-CMT	NONMEM 7.4.0	53-63	Patients with Manilfredia bluestem infections	PO/IV
Dvorackova 2023[9]	Czech Republic	NR	40/78	perspicacity	NR	Monolix Suite 2021R1	38-68	Adult lung transplant recipients	PO
Hu 2023[34]	China	NM:IM:PM=37:43:11	91/210	retrospectivity	1-CMT	NONMEM 7.5	2-14	Paediatric haematology patients	PO
Wang Jing 2023[35]	China	NR	150/438	retrospectivity	1-CMT	NONMEM 7.3.0	60-103	Elderly patients	IV
van den Born 2023[22]	Netherlands	NR	54/1060	perspicacity	1-CMT	Edsim++ 1.9.1.30	19-73	Prevention and treatment of patients with invasive fungal infections	PO/IV
Ling 2024[36]	China	NM:IM:PM=66:72:29	167/232	retrospectivity	1-CMT	NONMEM 7.3.0	16-97	Patients with invasive fungal infections	PO/IV
Wang 2025[42]	China	RM EM IM PM=1:28:39:4	72/150	perspicacity	1-CMT	NONMEM 7.3.0	77(69, 84)	COVID-19-associated pulmonary aspergillosis	IV
Akbar 2025[27]	Pakistan	NR	88/88	retrospectivity	1-CMT	NONMEM 7.4.4	3-90	Cancer patients with systemic fungal infections	IV

CMT compartment model; PO: oral administration; IV: intravenous administration; NFT: nasal feeding tube; HEMs: heterozygous extensive metabolizers; EMs: homozygous extensive metabolizers; NM: cytochrome P450 2C19 normal metabolizer; IM: cytochrome P450 2C19 interme- diate metabolizer; PM: cytochrome P450 2C19 poor metabolizer; RM: CYP2C19 rapid metabolizee; UM: ultra-rapid metabolizer

3.2 Clinical Protocol and Design

Among the included studies, 10 were retrospective in nature [27-36], 18 were prospective studies, and the remaining study adopted a mixed-methods design combining both prospective and retrospective approaches [7]. The dose of VRC was determined by the physicians in each hospital based on their clinical judgment and in accordance with the recommended dosing regimen. The route of administration across all 16 studies was either intravenous or oral; specifically, six studies utilized intravenous administration, six studies used oral administration, and one study employed oral administration via a nasogastric tube. Among the 29 PopPK models describing VRC, five studies

focused on the pediatric population [23, 26, 33-34, 37], one study was specifically designed for elderly patients [35], one study encompassed patients across all age groups [27], and the remaining studies were conducted in adult populations. The study population comprised healthy volunteers and patients receiving voriconazole for the treatment or prophylaxis of fungal infections. These individuals might also present with comorbidities such as liver dysfunction, organ transplantation, or hematologic malignancies.

3.3 PopPK Analysis

Table 2 provides a summary of the model characteristics for the included studies. As shown in Table 2, 19 studies utilized NONMEM modeling along with associated parameter analysis, 8 studies employed Phoenix®NLME modeling, 1 study adopted Monolix Suite modeling, and 1 study applied Edsim++ modeling. Twenty-one literatures were included in the CYP2C19 genotyping data [7-8, 19, 21, 23-26, 28-30, 32-34, 36-42]. Most of the individual variability in the base model was attributed to the exponential error model, while the individual variability in the final model was primarily driven by residual variation combined with the exponential error model. For covariate screening of the model, all studies employed the stepwise method for forward inclusion and backward elimination. In the context of model verification and evaluation, the majority of studies adopt the goodness-of-fit plot method (GOF) to assess the adequacy of the final model fit, the nonparametric Bootstrap method to evaluate the robustness and reliability of the final model, and the visual predictive check (VPC) to assess the predictive performance of the model [38]. Several models were assessed both graphically and statistically through the utilization of normalized prediction distribution errors (NPDEs)[33, 37]. A total of five studies established the absorption rate constant as a fixed value [7, 29, 33, 37, 38], four studies used lag times to balance the delayed absorption of the model [21, 23-25].

Table 2 Summary of Covariate Characteristics of the VRC Clinical PopPK Model

Study	Combination of drugs	Covariates tested	Significant covariate	Residual model	Pharmacokinetic parameters
Karlsson 2009[26]	CYP2C19 inhibitors, CYP2C9 inhibitors, CYP3A4 inhibitors and CYP450 inducers	Age, Sex, Weight, Height, Race, Scr, AST, ALT, ALP, GGT, ALB, TBIL, and Total Protein Levels	CYP2C19 genotype and alanine aminotransferase levels	BSV: exponential error model; WSV NR	CL=4.28×(DBIL /2.6)−0.4 L/h; Vc=93.4 L; Vc (L/kg)=0.807; Q=0.609; Vp=2.17; Ka(h-1)=0.849; F= 44.6%
Han 2010[20]	NR	Diagnosis, age, weight, race, sex, days post-transplant, and pre-transplant, post-transplant, and same-day laboratory biochemical characteristics	Cystic fibrosis, postoperative time and body weight	BSV: exponential error model; WSV combinatorial error model	F=45.9%; CL=3.45L/h、Vc=54.7L; Vp=143L
Han 2011[21]	Pantoprazole, alanine transaminase	Age, sex, weight, body mass index, liver and kidney function and CYP2C19 genotype	ALT and pantoprazole	BSV&WSV Additive error models, proportional error models, combinatorial error models and exponential error models	CL/F=7.92 L/h Vd/F=248 L
Dolton 2014[24]	PPIs, phenytoin, rifampicin, short-term ritonavir and glucocorticosteroids	Body weight, age, sex and CYP2C19 genotype	Combined use of phenytoin or rifampicin, St John's wort, methylprednisolone, dexamethasone and prednisone , CYP2C19 phenotypes for EM/ HUM	BSV exponential error model; WSV Proportional error models, additive error models and combinatorial error models	Ka=0.53h−1; Lag time=0.162h F=94.2%; Vc=27.1 L; Vp=127 L; Q=35.1L/h; Vmax=43.9 mg/h; Km =3.33 mg/L
Chen WY 2014[43]	Azithromycin, methylprednisolone, omeprazole, glutathione, levofloxacin	Age, sex, weight, BUN, CRP, UA, CLCR, ALB, ALT, AST, ALP, GGT, TBIL, DBIL, TG, CHO, TBA	DBIL	BSV exponential error model; WSV constant coefficient model	CL=4.28 L/h; V=93.4 L
Muto 2015[23]	NR	Age, sex, weight, body mass index, CYP2C19 genotype	Age and weight	BSV exponential error model; WSV additive error model	CL (liters/h/70 kgc)= 6.16; F=73%; V2 (liters/70

					kg)= 79.0; V3 (liters/70 kg)= 103; Q (liters/h/70 kgc)=25.4
Li Z 2017[28]	Glucocorticoids and PPIs	Age, sex, weight, blood, liver and renal function indices, time since transplantation, CYP2C19 genotype	AST and CYP2C19 genotypes	BSV exponential error model; WSV proportional error model	CL=4.76 L/h; V=22.47 L
Lin XB 2018[8]	Tacrolimus, cyclosporine; omeprazole, esomeprazole, pantoprazole, lansoprazole and methylprednisolone	Age,weight,WBC,HGB,PLT, ALT,AST,ALB,TBIL,DBIL, Scr,CYP2C19 genotype, POT	CYP2C19 genotypes, POT, weight	BSV exponential error model; WSV additive error model	θV=169.27; θCL=2.88; θF=58%
Kim 2019[25]	PPIs and glucocorticoids	Age, sex, weight, CYP2C19 genotype, AST, ALT, Scr, eGFR	CYP2C19 genotypes, weight, Hepatic insufficiency (≥grade 3)	BSV exponential error model WSV Additive error models, proportional error models and joint additive and proportional error models	V2:35.7;CL:45.3 V3:58.9;Q2:10.9 V4:25.4;Q3:54.6 Ka:1.23 F1=87.6%; lag time 0.237 h
Chen C 2019[29]	MMF, acyclovir and SMZ dosage forms, dosage amounts, dosing intervals, duration of administration	Sex, age, weight and WBC, RBC, MCV, NEUT, PLT, lymphocytes, monocytes, AST, ALT, ALB, total protein, ALP, GGT, TBIL, CR and BUN	CYP2C19*2 genotype and MMF co-administration	BSV NR; WSV proportional error model	F=89.5%; FIX;CL=9.52 L/h;V=155 L;Ka (h-1)=1.1 FIX
Liu 2019[41]	CYP2C19 inhibitor, inducer	Age, sex, weight, ALP, AST, ALT, TBIL, total protein, ALB, BUN, Scr, HGB levels	CYP2C19 genotypes, Age	BSV exponential error model; WSV joint additive and proportional error models	CL=4.18 L/h，V=88.9 L，Ka=0.729h−1
Tang 2019[44]	PPI	Age, sex, weight, HGB, PLT, ALT, AST, ALB, TBIL, DBIL, BUN, UA, INR, CLCR, CYP2C19 genotype	PLT	BSV exponential error model; WSV Additive error model, proportional error model, exponential error model	CL=0.58 L/h，Vd=134 L，F=80.8%
Ren 2019[30]	PPI	VRC dose, frequency and duration of use, age, sex, weight, CLCR, PL, Scr, PT, ALT, AST, ALP, TBIL, GGT, ALB, HGB, CRP, Child-Pugh classification (A, B, C)	CYP2C19 genotypes and Child-Pugh classification、BW	BSV exponential error model; WSV proportional error model	CL=1.45 L/h; V=132.12 L
Khan-asa 2020[19]	PPIs,sulfamethoxazole /metronidazole, glucocorticoids	Age, sex, diagnosis, weight, source of fungal infection, WBC, NEUT, HGB, MCV, PLT, BUN, Scr, AST, ALT, ALP, DB, TB, ALB, Glo, CYP2C19 genotype	Alb and omeprazole ≥40 mg/day	BSV exponential error model; WSV Additive error model	CL/F(oral cavity)=3.43 L/h V/F=47.6 L; Ka=1.1 h−1
Tang 2021[38]	PPIs	Age, sex, weight, PLT, ALT, AST, TBIL, DBIL, ALB, CLCR, INR	PLT、TBIL	BSV exponential error model; WSV proportional error model	CL=0.88 L/h; V=148.8 L; F=88.4%; CL=18.0%; V=12.0%; ka (h−1) =1.1(fix)
Chanthar it 2020[7]	glucocorticoids、PPIs	Age, sex, weight, underlying disease, site of infection, time of blood collection, underlying disease, AST, ALT, ALB, GGT, CYP2C19 genotypes, sepsis	ALB、GGT	BSV exponential error model; WSV Combinations of additive, proportional and (additive + proportional) modelsl	CL=7.32L/h ; V=417.91L; ka (h−1) =1.1(fix)
Lin XB 2022[40]	PPIs	Age, weight, inflammatory markers, Child-Pugh category, CYP2C19 genotype, APACHE II score,	weight、Child-Pugh category	BSV exponential error model; WSV Combinations of additive, proportional	CL (CP-A/B)=2.33 L/h; CL(CP-C)=1.29

		SOFA score		and (additive + proportional) modelsl	L/h; Vc=51.64L; Vp=110.89 L; Q (L/h) =36.45
Wang Jun 2021[37]	Concomitant drugs (not specified)	Age, sex, weight, height, BSA, ALT, AST,TBIL, ALB, BUN, Scr, UA, eGFR, CRP, IL-6, CYP2C19 genotypes	weight、CYP2C19 genotypes、omeprazole	BSV exponential error model; WSV proportional error model	V1=22.79L; V2=61.28L; Q=13.71L·h-1; Vmax=18.13L·h-1; Km=1.15 h-1(fixed)
Wang T 2021[31]	CYP2C19 inhibitors and inducers	Time of administration, dose, route, demographics, type of cirrhosis, Child-Pugh classification and MELD end-stage liver disease model	Child-Pugh category、weight	BSV exponential error model; WSV proportional error model	CL（non-LC）=7.59 L/h; CL (CP-A/B)=1.86 L/h; CL (CP-C)=0.93 L/h; Vc=100.8 L; Vp=55.2 L; F=91.6%;
Li SC 2021[32]	PPIs、GLU	Age, sex, weight, height, TBIL, DBIL, IBIL, TBA, ALT, AST, ALP, GGT, TP, ALB, GLB, BUN, UA, SCR, BSA	CYP2C19 genotypes	BSV exponential error model; WSV WSV Proportional error models, additive error models and combinatorial error models	ka=1.1/h;F=89.5 %;V (L)=207.29;CL(L/h)=1.91
Wu 2022[33]	PPIs、GLU	Age, sex, weight, BSA, WBC, NEUT, HGB, PLT, TBIL, AST, ALT, GGT, ALB, ALP, Scr, CYSC, Ccr	ALB、CYP2C19genotypes	BSV exponential error model; WSV Proportional error models, additive error models and combinatorial error models	CL=2.29 L/h，V=76 L; F=90.2%; Ka= 1.19h-1(fixed)
Jiang 2022[39]	PPI	Sex, age, weight, height, underlying disease (HIV), VRC medication information (date, dose, time of administration, interval), WBC, HGB, PLT, NEUT, ALT, AST, ALB, TP, TBIL, GGT, urea, CRP	CRP	BSV exponential error model; WSV additive and proportional model	CL=4.34 L/h，V=97.4 L，K=1.1 h-1，F=95.1%
Dvorackova 2023[9]	tacrolimus, Glu (prednisone), gastric pH-raising drugs (famotidine or proton pump inhibitors) and CYP450 inhibitors (azithromycin)	Age, sex, height, Scr, ALT, AST, GGT, eGFR	Age	BSV&WSV Proportional error model	Vd/F=964.46 L; CL/F=32.26 L/h; Ka=0.59h-1
Hu 2023[34]	NR	Race, IFIs, CYP2C19 genotypes, diagnosis, dose, duration of therapy, route of administration, co-administration of medications, TDM results, hepatic and renal function markers	CYP2C19 genotypes	BSV&WSV exponential error model	CL=7.35 L/h、Vc=376 L、F=52.2%、K=1.19h-1
Wang J 2023[35]	Dose, dosing interval, duration of administration, dexamethasone, fluconazole, itraconazole, methylprednisolone, omeprazole, pantoprazole, phenytoin, prednisolone, rabeprazole, rifampicin	Age, sex, weight, ALB, ALT, ALP, APoA, APoB, AST, CRP, CLCR, DBIL, eGFR, GGT, GLO, HGB, PLT, TBIL, TP, WBC	ALB、γ-GGT、DBIL	BSV exponential error model; WSV WSV proportional error models, additive error models and combinatorial error models	CL=3.22 L/h，V=194 L

van den Born 2023[22]	NR	Weight, CRP, ALT, AST, TBIL, ALP, GGT	CRP	BSV&WSV proportional error models, additive error models	V=145 L，Km=5.7 mg/L，Vmax=86.4 mg/h，F=83%
Ling J 2024[36]	PPIs;glucocorticoids	Age, gender, body weight, the CYP2C19 genotypes, CRP, ALB,ALT, AST,TBIL, HGB, PLT, Scr, UA,	CL age,ALB, gender, CRP, CYP2C19 genotypes; V body weight.	BSV exponential error model; WSV Index Additive Portfolio error models	CL=3.83 L/h，V=134 L/h，F=96.5%
Wang 2025[42]	paxlovid, azvudine, clopidogrel, PPIs, CCBs,Glu	Sex, age, weigh, ALT, AST, ALP, GGT, TBIL, DBIL, ALB, GLO, WBC, NEUT, HGB, HCT, PLT, APoA, APoB, GLU, INR, Scr, CRP, CLCR, eGFR, CRRT	CL CRRT、CRP、GGT、AST、PLT	BSV exponential error model; WSV additive error models	CL/F=3.17 L/h，V/F=135 L
Akbar 2025[27]	NR	Age, weight, sex, AST,ALT,ALP,Type of cancer (primary diagnosis) and type of fungal infection	CL CLCR、cancer (primary diagnosis)	BSV exponential error model; WSV proportional error model	CL=6.17 L/h，V=55.9 L

AST aspartate transaminase; ALT alanine aminotransferase; ALP alkaline phosphatase; ALB albumin; TBIL total bilirubin; BUN blood nitrogen; UA uric acid; CLCR creatinine clearance; GGT γ- glutamyltransferase; DBIL direct bilirubin; TG triglycerides; CHO Total cholesterol; TBA Total bile acids; WBC white blood cells; HGB hemoglobin; PLT platelet count ; Scr serum creatinine; POT postoperative time; RBC Red blood cells; MCV Red blood cell volume; NEUT Neutrophils; INR International normalized ratio; PT Prothrombin time; BSA body surface area (calculated according to Mosteller formula); eGFR glomerular filtration rate (calculated according to CKP-EPI formula); IL-6 interleukin-6; TP total protein; BUN blood urea nitrogen; CYSC cystatin C; Ccr endogenous creatinine clearance; APoA apolipoprotein A; APoB apolipoprotein B; GLo globulin; NR not reported; MMF mycophenolate mofetil; SMZ Sulfamethoxazole; GLUs glucocorticoids.

4 RESULTS

4.1 Patients with Fungal Infections

During infection or inflammation, drug-metabolizing enzymes, including CYP450 isoenzymes, exhibit decreased expression at the transcriptional level, leading to reduced metabolism of voriconazole (VRC). Additionally, the C-reactive protein (CRP) level and the concomitant use of proton pump inhibitors (PPIs) were identified as significant covariates for optimizing the initial voriconazole dose in the population pharmacokinetic (PopPK) study conducted by Jiang et al [39], the maximum daily dose of PPI should not exceed 40 mg. In this study, when CRP ≤ 96 mg/L in patients with F. marneffei using VRC, the recommended loading dose is 250 mg/12 h, and the maintenance dose is 100 mg/12 h. When CRP > 96 mg/L, the recommended loading dose is 200 mg/12 h, and the maintenance dose is 75 mg/12 h [39]. In the PopPK model of Aspergillus patients established by Chantharit et al [7] ,serum albumin (ALB) and γ-glutamyl transpeptidase (GGT) were significantly correlated with VRC clearance, and patients in the ALB>30 g/L group needed higher doses to achieve a target concentration similar to that in the ALB≤30 g/L group. Meanwhile, nutritional status was considered to be unexplored. Based on the review of 22 previous PopPK models of VRC, Van Den Born et al [22] selected one of the one-compartment models to establish the PopPK model in patients with fungal infection, and found that CRP significantly affected Vmax. However, the inclusion of CRP increased the coefficient of variation of Vmax CV% from 52% to 99%. It is possible that this study mainly included retrospective data and the high heterogeneity reduced the reliability of the model. Based on the review of previous 22-item VRC PopPK model, although Van Den Born et al. 's model further verified Chantharit et al ' s guess that CRP may affect VRC exposure, more comprehensive data should be used in the future to improve the accuracy of the model.

In critically ill patients with pulmonary fungal infection, Chen et al [43] found that direct bilirubin (DBIL) was significantly correlated with CL after investigating the related factors affecting VRC metabolism. If DBIL was higher than 1 times the average level, CL of VRC decreased by 24.21%. This study suggests that the range of VRC therapy in critically ill patients is between 1.5 and 4.0 μg/mL, which is narrower than that in normal patients. Therefore, it is recommended that the initial loading dose be followed by ivgtt of 150 mg or 200 mg q12h, and 150 mg bid for patients with mild to moderate infection or prophylactic treatment. Ling et al [36] conducted a retrospective analysis of invasive fungal infection patients with different CRP levels combined with CYP2C19 genotype polymorphism, in which the group of patients with CRP over 200 mg/L was compared with the group of patients with CRP below 10 mg/L. The percentage of CYP2C19 NM and IM patients reaching therapeutic trough concentration increased from 20.10% and 41.10% to 26.65% and 14.06%, while the percentage of patients reaching toxic range increased from 20.10% and 41.10% to 73.34% and 85.94%, respectively. The level of inflammation combined with genotype seems to be beneficial for adjusting VRC dosing regimens. Moreover, Wang et al [42] evaluated the PK characteristics of voriconazole in patients with COVID-19 related pulmonary aspergillosis and found that CRRT and CRP both affected the CL of voriconazole. For every 150 mg/L increase in CRP, the CL of voriconazole decreased by 50%. Dosing regimens were

optimized according to whether patients were receiving CRRT, with recommended doses of 2 mg/kg q12h for those not receiving CRRT and 4 mg/kg q12h for those receiving CRRT to ensure a therapeutic range of 2-5 μg/mL.

4.2 Transplant Patients and Immunodeficient Patients

In renal transplant patients, the PopPK model of Li et al [28] showed that AST and CYP2C19 genotype had a significant effect on CL, and the trough concentration of VRC was significantly higher in CYP2C19 intermediate metabolic phenotype (IM) than in extensive metabolic phenotype (NM). This is consistent with the prospective PopPK study of Lin et al [8] in renal transplant patients, CYP2C19 genotype has a significant effect on CL, and the VRC trough concentration of the poor metabolic group (PM) is significantly higher than that of the IM and NM phenotypes. The study combined with the time after transplantation to give the estimated dosing regimen for PM, IM and NM genotypes, respectively. See Table 3 for details. Han et al [20] found in lung transplant patients that the bioavailability of VRC in patients with pulmonary fibrosis was significantly lower than that in patients without fibrosis, and that pulmonary fibrosis, time after transplantation, and body weight were factors affecting VRC clearance. However, this study suggests correction bias in population predictions only at low concentrations, which also suggests that patient variables only partially explain the variability in VRC pharmacokinetics in lung transplant patients. Han et al. identified pantoprazole, race, and ALT as parameters influencing VRC pharmacokinetics in liver transplant patients, and the model was externally validated using a retrospectively collected random sample. [21].

Table 3 Summary of CYP2C19 Genotype-Guided VRC Dosing Regimens

CYP2C19 genotype dosing regimen	PM	IM	EM/NM
Lin XB 2018[8](renal transplant recipients)	150 mg bid ivgtt/250mg bid po	200 mg bid ivgtt350mg bid po	300 mg bid ivgtt
LI SC 2021[32]（immunocompromised patients）	225 mg bid/150 mg tid	275 mg bid/175 mg tid	325 mg bid/200 mg tid
Hu Lin 2023[34]（paediatric hematological diseases patients ）	6 mg/kg bid po /5 mg/kg bid ivgtt	9 mg/kg bid po / 5mg/kg bid ivgtt	9 mg/kg bid po / 8mg/kg bid ivgtt
Kim 2019[25]（healthy volunteers and patient）	Loading dose 400mg bid po, maintenance dose 100mg bid po	Loading dose 400mg bid po, maintenance dose 200mg bid po	Loading dose 400mg bid po, maintenance dose 400mg bid po
Liu Yang 2019[41]（elderly patients）	50mg bid po	100mg bid po	\
Ren 2019[30] (patients with A. fumigatus infections)	\	\	Child-Pugh class A and B,75 mg bid ivgtt/Child-Pugh class C，100 mg qd ivgtt

Note: bid: twice daily; po: oral;ivgtt: intravenous drip; qd: once daily; q12h: every 12 hours; q8h: every 8 hours; LD: loading dose; MD: maintenance dose; Child-Pugh: liver function class

In the PopPK of lung transplant patients established by Eliska et al [9], CL of VRC decreased by 0.021 L/h with increasing patient age. In immunocompromised patients, only Li et al [32] retrospectively established the PopPK model and estimated the dosing regimen for NM, IM, and PM genotypes by weighing the relationship between toxicity and efficacy, but the study included only trough concentrations due to retrospective analysis. It is difficult to estimate the evaluation of VRC and its metabolites, such as n-oxide metabolites, during the absorption and distribution periods [32]. Wang et al [31] conducted a PopPK study on patients with liver cirrhosis and found that 69.0% of VRC-related Adverse Events (AEs) occurred within the first week after VRC treatment, indicating that accurate initial dose or blood concentration monitoring of VRC should be carried out as soon as possible to avoid adverse reactions.

VRC is used as a first-line agent to prevent and treat IFIs in allogeneic hematopoietic stem cell transplant recipients [45]. Chen et al [29] conducted PopPK modeling based on the retrospective blood drug concentration data of patients with hematopoietic stem cell transplantation, and the model showed that mycophenolate mofetil and CYP2C19* 2 polymorphism showed a significant effect on CL, with a positive correlation between mycophenolate mofetil and a negative correlation between CYP2C19* 2. In order to discuss the pharmacokinetic changes of VRC in patients with allogeneic hematopoietic stem cell recipients, Suetsugu et al [45] conducted a retrospective PopPK analysis of VRC trough concentrations and found that the combination of letemovir and methylprednisolone increased Vmax of VRC, thereby reducing plasma VRC trough concentrations. Therefore, when lemovir and methylprednisolone are administered simultaneously, the daily dose of VRC needs to be increased to obtain the optimal VRC trough concentration.

4.3 Patients with Organ Dysfunction

In patients with liver dysfunction, the PopPK model of Tang et al [38] showed that total bilirubin (TBIL) was an important predictor of VRC pharmacokinetic parameters, and platelet count (PLT) was significantly correlated with VRC pharmacokinetic parameters. Since CL of VRC is significantly reduced in patients with hepatic insufficiency, dose reduction and prolonged dosing interval should be considered for such patient [38]. For patients with cirrhosis, Ren et al

[30] demonstrated that Child-Pugh class B or C and CYP2C19 genotype are significant factors influencing voriconazole clearance. This finding underscores the importance of utilizing comprehensive liver function indices to evaluate the dosing regimen. These results are consistent with the retrospective PopPK study conducted by Wang et al [31] in cirrhotic patients, which indicated that cirrhosis may exert a greater influence on voriconazole PK parameters than CYP2C19 gene polymorphisms. Lin et al [40] established a PopPK model for patients with hepatic insufficiency, and the results proved that the weight was positively correlated with the volume of distribution (V) of VRC, and Child-Pugh classification had a significant effect on CL. In this study, the recommended intravenous VRC maintenance dose regimen was 100 mg q12h or 200 mg q24h for patients with C-P A/B and 50 mg q12h or 100 mg q24h for patients with C-P C. In addition, the combined use of inflammation and PPIs was also not identified as a significant covariate in Lin's study [40], including the effect of hypoproteinemia on VRC pharmacokinetics in patients with liver disease requiring further investigation.

Khan-Asa et al [19] conducted a PopPK study of VRC in adult patients with hematological diseases. The results indicated that ALB levels and omeprazole doses ≥40 mg/day significantly influenced the clearance-to-fraction absorbed ratio (CL/F). Specifically, patients with lower ALB levels should be prescribed a reduced dose of VRC compared to those with normal ALB levels. Furthermore, caution is advised when administering VRC to patients with hypoalbuminemia who are concurrently receiving omeprazole at doses ≥40 mg/day. Meanwhile, Liu et al [41] developed a PopPK model for VRC in Chinese adult patients with hematological malignancies. Their findings demonstrated that age and CYP2C19 phenotype significantly influenced the CL of VRC, suggesting that genetic testing is essential for elderly Asian patients. Additionally, Akbar et al [27] investigated covariates affecting the pharmacokinetics of intravenous VRC in Pakistani cancer patients. They identified that variations in cancer type and CLCR resulted in differences in VRC clearance. However, further research is warranted to determine how cancer type can guide VRC dosing strategies for individual patients.

4.4 Patients with Special Populations

Wang et al [35] conducted a PopPK study in elderly patients, and the covariate analysis of the model revealed that ALB, γ-glutamyl transpeptidase(γ-GGT), and DBIL significantly influenced the CL of VRC. This study represents the first effort to externally and systematically assess the predictive performance of the PopPK model for VRC in the elderly population. Resztak et al [14] demonstrated that interindividual PK variability is more pronounced in children compared to adults, attributed to their higher weight-standardized clearance and enhanced whole-body and first-pass metabolism. This finding aligns with the study by Karlsson et al [26], who reported that the liver mass to body mass ratio is greater in children than in adults. Consequently, they recommended an intravenous dose of 7 mg/kg twice daily or an oral dose of 200 mg twice daily for patients aged 2-12 years. Additionally, the clearance rate of VRC is significantly higher in children under 12 years old, and its oral bioavailability in children is lower than in adults, reaching only 62%. These observations underscore that age is a critical factor influencing VRC plasma exposure [14].

Hu et al [34] established a PopPK model of VRC in children with hematological IFIs, and the results showed that the oral bioavailability of VRC was only 52%, which was lower than 96% of adults, which was similar to the value of 66% obtained by Walsh et al [46] in children aged 2-12 years. At the same time, this study suggests that the presence of CYP3A4 in the intestine may accelerate the metabolism of oral VRC, which is worthy of further confirmation. This study suggests that CYP2C19 phenotype can be used to guide the adjustment of VRC trough concentration dose in pediatric patients with IFIs. Wu et al [33] established a PopPK model of VRC in Chinese children with hematological malignancies, and the study confirmed that body weight was more suitable than age when allometric model was considered, and the final model showed that body weight, CYP2C19 phenotype and ALB had a significant impact on VRC clearance. Similarly, Takahashi et al [47] investigated the genetic and covariate associations of PK variability among VRC individuals and showed that PK variability among VRC individuals in the age range from 7 months to 20 years is best described by weight function allometric scaling and CYP2C19 phenotype. The study model of adult hematological malignancies by Liu et al [41] showed that age and CYP2C19 genotype were important covariates, while the study model of children by Wu et al [33] showed that weight was more suitable for guiding drug administration than age.

As it is well known that developmental factors play an important role in VRC metabolism in children, Wang J et al [37] developed a PopPK model of intravenous VRC in critically ill children, tested six candidate models to describe differences in the growth and clearance processes of allopathy, and suggested that it was necessary to adjust the dosing regimen according to CYP2C19 genotype. Muto et al [23] established a PopPK model for children with weakened immunity, which tried to identify the effects of new covariates such as CYP2C19 genotype, gender and liver function parameters on other PK parameters of VRC, but failed. CYP2C19 genotype does not seem to be a basis for adjusting the dose for Japanese children. Moreover, no trend was observed by graphical evaluation, and final age and weight were considered as significant covariates in this model. Bioavailability was in the range of 65±20.64 in the four pediatric patients included in this study [23, 26, 33, 34], the bioavailability of 12 items in adult patients ranged from 83.34±15.57 [8, 20-22, 25, 29, 31, 32, 36, 38, 39, 44].

5 GENOTYPE POLYMORPHISM

More and more studies have shown that CYP2C19 genotype is closely related to the therapeutic plasma concentration

difference of VRC. Studies have shown that the proportion of CYP2C19 generation PM phenotype is the highest in the Asian population, about 23%, while the European phenotype is about 7% [14]. Therefore, it is necessary for Asian patients to undergo genetic testing [41]. Of the 29 studies included in this review, only 8 studies did not include CYP2C19 genotype. In adult lung transplant patients [9, 20]、in patients with liver dysfunction [44]、in elderly patients [35]、in patients with cirrhosis [31]、in immunocompromised patients [23]、in patients with cancer [27]、and in patients with a fungal infection [22].

Kim et al [25] established a PopPK model including CYP2C19 phenotype in a group of healthy volunteers and patient populations, and CYP2C19 phenotype, body weight and liver function indicators were considered as significant covariates. This study showed that EM subjects were more likely to reach subtherapeutic concentrations (73.9%) and PM subjects were more likely to reach highly toxic concentrations (48.3%), suggesting that VRC dosing should be adjusted according to CYP2C19 phenotype. Hu et al [34] suggested that low oral bioavailability, high CL and high proportion of CYP2C19 NM were responsible for low VRC trough concentrations. Therefore, it is important to focus on the problem of low VRC trough concentration levels in NMs. Ling et al [36] retrospectively analyzed the effect of inflammation on VRC pharmacokinetics in patients with different CYP2C19 genotypes, and indicated that patients with NM and IM complicated with inflammation should be closely monitored when given VRC.

According to Table 3, the recommended dose of EM/NM in patients with normal extensive metabolism is generally higher than that in patients with intermediate metabolism IM phenotype and poor metabolism PM phenotype, and the appropriate dose and frequency are in the range of 300 mg bid to 400 mg bid. 75 mg bid ivgtt is recommended for patients with mild-to-moderate liver injury, and 100 mg qd ivgtt is recommended for patients with severe liver injury. However, the dosing regimen guided by CYP2C19 phenotype still has challenges in real life [24], because genotype information is usually difficult to obtain in clinical practice, and may be obtained after the patient has been treated. Liu et al [48] proposed that CYP2C19 gene polymorphism should be genotyped for drug administration, and it does not seem to be necessary to consider the effects of CYP2C9, CYP3A4 and FMO3 polymorphisms on the pharmacokinetics of voriconazole. In fact, this is in contrast to the study by Gautier-Veyret et al [49], who demonstrated in a retrospective study that the CYP3A4*22 polymorphism (rs35599367) significantly affected voriconazole trough concentrations in 29 patients undergoing allogeneic HSCT. In addition, two retrospective studies in China found that SNPS located in the intron region of CYP3A4 (rs4646437) were associated with higher VRC levels [50, 51]. Data on genetic variants in CYP3A4 affecting plasma concentrations of VRC are limited and need to be confirmed in independent and larger cohorts of patients treated with voriconazole.

6 SUMMARY OF SIGNIFICANT COVARIATES

By summarizing the significant covariates in the PopPK model of VRC, Table 4 was obtained. Most of the methods for covariate screening in this review were stepwise covariate modeling, and a few were log-likelihood methods. Among the 21 studies, the CYP2C19 genotype was identified as a significant covariate in 13 studies [8, 24-26, 28-30, 32-34, 37, 41].In conclusion, CYP2C19 phenotype is considered to have a significant effect on the pharmacokinetic parameters of VRC in many PopPK models, and it is expected to be an important basis for guiding the individualized treatment of VRC. Body weight was identified as a significant covariate in 8 studies [8, 23, 25, 30, 31, 36, 37, 40], indicating the potential to guide the clinical use of VRC according to patient weight, Albumin was accepted as a significant covariate in 5 studies[7, 26, 33, 35, 36], followed by age [9, 23, 36, 41]、γ -GGT [7, 21, 35, 42]and CRP[22, 36, 39, 42] were each identified as a significant covariate in 4 studies. Most of the significant covariates affecting VRC clearance were indicators of liver function, which can reduce plasma clearance of drugs due to reduced liver metabolism or biliary excretion [38].

Table 4 Significant Covariates Included in the Studies Reviewed

Study	Significant covariate
Kim 2019[25]、Dolton 2014[24]、Chen 2019[29]、Liu 2019[41]、WangJ 2021[37]、Wu 2022[33]、Li 2017[28]、Ren 2019[30]、Hu 2023[34]、LiSC 2021[32]、Karlsson 2009[26]、Lin XB 2018[8]、Ling J 2024[36]	CYP2C19 phenotype
Kim 2019[25]、Lin 2022[40]、WangJ 2021[37]、Ren 2019[30]、WangT 2021[31]、Muto 2015[23]、Lin XB 2018[8]、Ling J 2024[36]	Weight
Wu 2022[33]、Wang 2023[35]、Chantharit 2020[7]、Ling J2024[36]、Karlsson 2009[26]	ALB
Dvorackova 2023[9]、Liu 2019[41]、Muto 2015[23]、Ling J 2024[36]	Age
Wang 2023[35]、Han 2011[21]、Chantharit 2020[7]、Wang 2025[42]	γ -GGT
Jiang 2023[39]、van den Born 2023[22]、Ling J 2024[36]、Wang 2025[42]	CRP
Lin 2022[40]、Ren 2019[30]、WangT 2021[31]	Child-Pugh classification
Tang 2019[44]、Tang Dan 2021[38]、Wang 2025[42]	PLT
Wang 2023[35]、Chen WY 2014[43]	DBIL
Karlsson 2009[26]、Wang 2025[42]	ALT
Kim 2019[25]	Liver insufficiency (≥ grade 3)
Dolton 2014[24]	Glu

Ling J 2024[36]	Gender
Chen 2019[29]	MMF
WangJ 2021[37]	Omeprazole
Khan-asa 2020[19]	Omeprazole≥40 mg/Day
Li 2017[28]	AST
Akbar 2025[27]	CLCR
Han 2011[21]	Pantoprazole
Tang Dan 2021[38]	TBIL
Wang 2025[42]	CRRT
Akbar 2025[27]	Cancer (primary diagnosis)

7 DRUG-DRUG INTERACTIONS IN THE VRC

The common concomitant drugs of voriconazole include PPIs and glucocorticoids. It is not clear whether the changes of voriconazole plasma concentration are affected by DDIs. Currently, it has been suggested that the exposure of voriconazole in plasma may be related to the type and dose of PPIs. Only three studies [19, 21, 37]， in this review included PPI as a significant covariate affecting VRC clearance or apparent volume of distribution. The Khan-asa study in the Thai population suggests that voriconazole should be used with caution or appropriately reduced dose in patients with hypoalbuminemia who are treated with omeprazole ≥40mg/day [19]。 Hna et al [21] suggested that co-administration of pantoprazole may affect the PK of VRC, but further correlation studies are lacking. Wang [37] in a study of critically ill pediatric patients, suggested that when omeprazole was not used, patients in the PM and IM groups required doses of 6 mg/kg and 8 mg/kg21 q12h, respectively, while patients in the EM group required doses of 9 mg/kg q12h. However, due to the limited sample size, the recommendations are for reference only and further clinical practice is needed. The study of Dolton et al [24] in healthy people showed that the combination of phenytoin, rifampin, St. John's's extract, methylprednisolone, dexamethasone and prednisone was associated with a significant increase in Vmax of the VRC, possibly because the exposure of the VRC was reduced to varying degrees by such drugs. Especially in patients with CYP2C19 phenotype EM/HUM, while short-term use of ritonavir can reduce Vmax, especially in patients with CYP2C19 phenotype PM/HEM. Therefore, glucocorticoids were included as a significant covariate in the study by Dolton et al [24]. In addition, DDIs between VRC and immunosuppressive agents in Hiv-Infected patients were not evaluated because antiretroviral therapy was not initiated during VRC induction therapy.

8 DISCUSSION

VRC is a widely used antifungal agent in IFIs patients with life-threatening infections caused by Aspergillus and Candida [52]. Although VRC is an established drug in clinical practice and is included in the World Health Organization Core List of Essential Medicines for adults and children[53], the relative importance of its different pathways and metabolic enzymes involved is still not fully elucidated. The dose optimization of VRC has always been a hot topic in clinical practice due to the nonlinearity of its pharmacokinetics, high inter-individual and intra-individual variability, large drug interactions, and relatively narrow therapeutic range [54]。

This study reviews the research on VRC in various clinical patients at home and abroad that includes it. In China, the PopPK of VRC has been preliminarily studied in patients with liver dysfunction, patients undergoing hematopoietic stem cell transplantation, patients with hematological malignancies, critically ill children, patients undergoing kidney transplantation, elderly patients, patients with impaired immune function, and patients with pulmonary infections. However, among them, the studies on patients with impaired immune function, patients with liver cirrhosis, etc. were all retrospective studies. The included data in these studies were all trough concentration data, which could not be used to characterize the absorption phase. It might not be possible to fully capture the distribution and elimination characteristics of VRC, thereby posing challenges to the estimation of its pharmacokinetics. Therefore, in such patients, The accuracy of parameter estimation and covariate detection still needs to be confirmed by developing large-sample prospective studies [32, 35]. The PopPK of VRC abroad has been preliminarily studied in transplant patients, adult patients with hematological diseases, pediatric patients and patients with invasive fungal infections.

VRC is mainly metabolized by CYP2C19 P450 enzyme. The proportion of homozygous fast metabolizer enzyme in Asian population (35%) is lower than that in Caucasian population (75%), so the plasma concentration of VRC in Asian population is generally higher than that in Caucasian population. In China, there is still a lack of research on CYP2C19 genotype in the modeling of PopPK in patients with liver dysfunction, elderly patients, and critically ill patients with pulmonary diseases, which needs further research in the future. In addition, the efficacy, safety, and economics of CYP2C19 genetic testing prior to VRC use have not been demonstrated [18]. In this study, a total of 21 studies included CYP2C19 genotype polymorphism as a model covariate, of which 13 studies included it as the final significant covariate in the model, indicating that it was of great significance for optimizing VRC in the guidance of precise drug delivery in clinical practice. It can be seen from this study that patients with NM, IM and PM phenotypes are more common than patients with UM and RM phenotypes in CYP2C19 genotype polymorphism in the Chinese population, and the ratio is about 3:3:1. Therefore, PM phenotype is less than NM phenotype and IM phenotype. In this review, several studies [38, 39] found that there was no significant difference in voriconazole PTA obtained through intravenous and oral routes, which may suggest that oral and intravenous administration can be alternated based on the patient's own gut nutrition assessment.

Invasive fungal disease poses a significant threat to immunocompromised patients, especially those with pediatric hematologic disorders or those receiving hematopoietic stem cell therapy [34]. In recent years, inflammation level and other clinical indicators such as CRP have also been considered to be related to individual PK differences of voriconazole in several PopPK models, but the specific dose and administration regimen need to be further verified. In organ transplant and immunodeficient patients treated with VRC, the time after transplantation and the degree of body recovery lead to gradual changes in the metabolism and excretion of VRC, which may affect the pharmacokinetics of VRC. The PopPK study of VRC in HSCT patients should also be studied prospectively in pediatric patients. There have been reports of using mechanistic models to simultaneously evaluate the PopPK properties of VRC and its n-oxide metabolite, but the effect of VNO on VRC can only partially explain the nonlinear pharmacokinetics of VRC, and VRC metabolite evaluation needs to be further studied [32].

In patients with organ dysfunction receiving VRC, especially those with liver dysfunction, the changes of transaminase and bilirubin should be monitored to control the individualized dosing of VRC. In patients with hematologic diseases, age and genotype are considered to be significant indicators that have a chance to guide the administration of drugs in such patients. Invasive aspergillosis (IA) is the most common IFIs in such patients, which is characterized by high morbidity and mortality [55], the European Conference on Infectious Leukemia (ECIL) and IDSA guidelines currently recommend VRC and itsuonazole as the first choice for the treatment of IA in patients with hematological malignancies, with the same level of recommendation (in the IDSA guidelines, VRC has a slightly higher recommendation level than itsuonazole) [4, 56]. In patients with liver dysfunction, liver function classification has been identified as a significant covariate affecting the pharmacokinetic variation of VRC in many studies, and Child-Pugh classification has been recommended for individualized treatment of VRC. Inflammatory markers, albumin and other factors are rarely validated as significant covariates in such patients.

In the special population of patients receiving VRC treatment, the body function of children continues to improve with age, and the metabolism of drugs also changes. So far, the toxicity targets of this group have not been verified, and the PopPK model of patients under 2 years old needs to be further established [16]. In this review, body weight was recommended by most PopPK models as an important indicator for VRC administration in children. However, it has been pointed out that because ontogenetic differences in VRC metabolic enzymes seem to lead to higher first-pass effects in children compared with adults, the dose required in children is much higher than in adults, even when body weight is considered [10]. The bioavailability of VRC in children (65±20.64) was also significantly lower than that in adults (83.34±15.57). In addition, the neonatal population is still at risk of underdosing and overdosing of VRC, and CYP2C19 genotype is also recommended for consideration in pediatric patients.

Multiple studies in this review have shown that standardized VRC dosing regimens are insufficient to achieve target therapeutic exposures in a variety of clinical Settings [29, 33, 57]. Optimizing the drug delivery strategy based on PopPK model combined with TDM can improve the VRC to achieve appropriate PK/PD indicators, optimize its precise drug delivery, and control its blood drug concentration within the therapeutic window [16]. Not only that, PopPK has important advantages in clinical practice, especially in pediatric patients, where PopPK is able to take advantage of opportunistic blood sampling. In this review, 3 pediatric studies [33, 34, 37] used residual blood after routine biochemical tests to determine PopPK, which provided new ideas for the study of POPPK in children with VRC.

In addition, model predictability must be assessed before use of model-informed precision dosing (MIPD). PopPK model evaluation methods are divided into basic internal evaluation, advanced internal evaluation, and external model evaluation. In fact, external evaluation of the model has proven to be one of the most rigorous methods for model testing and is necessary for the use of patient dose personalization in clinical Settings [58]. Only 3 reviews included in this study [21, 35, 57] made external validation of the model. The external validation is to use random samples of clinical patients not used for model construction as the model validation group, and to optimize the established PopPK model using the Bayesian feedback method, which is considered to be the most rigorous validation method, and the optimized final model helps to provide accurate and precise concentration prediction for specific patient groups [21]. In addition, there is a lack of research on the comparison of dose adjustment based on PopPK method and empirical dose adjustment at home and abroad, which is one of the directions that needs to be continued to be studied in the future.

In this review study, CYP450 metabolic enzymes and alleles serve as a critical foundation for individualized voriconazole dosing. However, there remain certain technical limitations and insufficient information in determining the actual genetic phenotype of patients to guide voriconazole (VRC) dosing. Currently, research on VRC in real-world clinical patients has broadly encompassed most drug users, and the population pharmacokinetic (PopPK) model plays a central role in guiding personalized VRC treatment. Nevertheless, in this review, only a subset of patients underwent simulation of the dosing regimen and external validation of the model based on significant covariates. Few studies have selected an independent cohort of patients to verify the simulated dosing regimen and evaluate its implementation, which warrants further investigation with larger sample sizes in future studies. Several limitations need to be considered. First, the limitation of this study to English literature may have led to the unintentional exclusion of relevant studies published in other languages, thus limiting the opportunity for comparative analyses within the same geographic region. Second, only parametric PPK models were included in this study, and non-parametric PPK models were excluded because the parameters of the non-parametric model were difficult to bridge to the parametric model

9 CONCLUSION

The implementation of a model repository that includes parameterized PopPK models within the VRC demonstrates

significant potential for advancing the field of MIPD. This review provides an in-depth analysis of relevant information on the population pharmacokinetics of VRC, serving as a valuable reference for both clinicians and researchers. For clinicians, this review emphasizes key predictors that can be utilized to optimize VRC dosing strategies. For researchers, it is recommended to conduct PopPK analyses on datasets collected over extended periods post-treatment initiation, enabling the detection of any potential temporal changes in pharmacokinetic parameters. A more detailed stratification and comprehensive investigation into the population pharmacokinetics of special populations warrant further exploration. In the future, when constructing PopPK models for VRC in specific patient populations, external validation of the model and comparison of its predictive performance are essential to ensure clinical applicability. Most studies have identified significant covariates of VRC in patients with varying physiological and pathological conditions; however, simulations based on these covariates for personalized dosing regimens remain underexplored. Monte Carlo simulation is proposed as a method to evaluate covariate effects derived from diverse patient groups. Additionally, it is recommended to assess the clinical efficacy differences between doses guided by PopPK models and traditional empirical doses, track the individualized medication effects of PopPK models, and conduct supplementary trials integrated with real-world clinical outcomes to enhance the rational use of these models in practice.

COMPETING INTERESTS

The authors have no relevant financial or non-financial interests to disclose.

FUNDING

Financial support for this publication was provided by the Guizhou Provincial Science and Technology Support Program (Qian Ke He Support [2021] General 443) and Department of pharmaceutics, Kweichow Moutai Hospital (Zunshi Ke He HZ (2022) No. 269).

AUTHORS' CONTRIBUTIONS

Min Luo, Liu Shi was responsible for reviewing, searching, screening the literature and checking the format of the review; Lu Yao was responsible for extracting the pharmacokinetic parameters and summarizing them into a table to write the review; Lei Gong, Bao Fu, Yan Chen and Tao Chen was responsible for checking and suggesting changes. All authors contributed to the design of the manuscript and discussed the typesetting of the manuscript.

REFERENCES

[1] Cordonnier C, Rovira M, Maertens J, et al. Voriconazole for secondary prophylaxis of invasive fungal infections in allogeneic stem cell transplant recipients: Results of the vosifi study. Haematologica, 2010, 95(10): 1762-1768. https://doi.org/10.3324/haematol.2009.020073.

[2] Mikulska M, Novelli A, Aversa F, et al. Voriconazole in clinical practice. Journal of chemotherapy (Florence, Italy), 2012, 24(6): 311-327. https://doi.org/10.1179/1973947812y.0000000051.

[3] Pappas P G, Kauffman C A, Andes D R, et al. Clinical practice guideline for the management of candidiasis: 2016 update by the infectious diseases society of america. Clinical infectious diseases: an official publication of the Infectious Diseases Society of America, 2016, 62(4): e1-50. https://doi.org/10.1093/cid/civ933.

[4] Patterson T F, Thompson G R, Denning D W, et al. Practice guidelines for the diagnosis and management of aspergillosis: 2016 update by the infectious diseases society of america. Clinical infectious diseases: an official publication of the Infectious Diseases Society of America, 2016, 63(4): e1-e60. https://doi.org/10.1093/cid/ciw326.

[5] Huang C, Dong D, Yu F, et al. Evaluation of pharmacokinetics and safety with bioequivalence of voriconazole injection of 2 formulations in chinese healthy volunteers: Bioequivalence study. Clinical pharmacology in drug development, 2023, 12(5): 542-547. https://doi.org/10.1002/cpdd.1218.

[6] Takesue Y, Hanai Y, Oda K, et al. Clinical practice guideline for the therapeutic drug monitoring of voriconazole in non-asian and asian adult patients: Consensus review by the japanese society of chemotherapy and the japanese society of therapeutic drug monitoring. Clinical therapeutics, 2022, 44(12): 1604-1623. https://doi.org/10.1016/j.clinthera.2022.10.005.

[7] Chantharit P, Tantasawat M, Kasai H, et al. Population pharmacokinetics of voriconazole in patients with invasive aspergillosis: Serum albumin level as a novel marker for clearance and dosage optimization. Therapeutic drug monitoring, 2020, 42(6): 872-879. https://doi.org/10.1097/ftd.0000000000000799.

[8] Lin X B, Li Z W, Yan M, et al. Population pharmacokinetics of voriconazole and CYP2C19 polymorphisms for optimizing dosing regimens in renal transplant recipients. British journal of clinical pharmacology, 2018, 84(7): 1587-1597. https://doi.org/10.1111/bcp.13595.

[9] Dvorackova E, Sima M, Vyskocilova K, et al. Population pharmacokinetics and covariate-based dosing individualization of voriconazole in lung transplant recipients. Journal of chemotherapy (Florence, Italy), 2023: 1-10. https://doi.org/10.1080/1120009x.2023.2219590.

[10] Schulz J, Kluwe F, Mikus G, et al. Novel insights into the complex pharmacokinetics of voriconazole: A review of its metabolism. Drug metabolism reviews, 2019, 51(3): 247-265. https://doi.org/10.1080/03602532.2019.1632888.

[11] Ullmann A J, Aguado J M, Arikan-Akdagli S, et al. Diagnosis and management of aspergillus diseases: Executive summary of the 2017 escmid-ECMM-ers guideline. Clinical microbiology and infection: the official publication of the European Society of Clinical Microbiology and Infectious Diseases, 2018, 24(Suppl 1): e1-e38. https://doi.org/10.1016/j.cmi.2018.01.002.

[12] Chen K, Zhang X, Ke X, et al. Individualized medication of voriconazole: A practice guideline of the division of therapeutic drug monitoring, chinese pharmacological society. Therapeutic drug monitoring, 2018, 40(6): 663-674. https://doi.org/10.1097/ftd.0000000000000561.

[13] Bodilsen J, D'Alessandris Q G, Humphreys H, et al. European society of clinical microbiology and infectious diseases guidelines on diagnosis and treatment of brain abscess in children and adults. Clinical microbiology and infection: the official publication of the European Society of Clinical Microbiology and Infectious Diseases, 2024, 30(1): 66-89. https://doi.org/10.1016/j.cmi.2023.08.016.

[14] Resztak M, Sobiak J, Czyrski A. Recent advances in therapeutic drug monitoring of voriconazole, mycophenolic acid, and vancomycin: A literature review of pediatric studies. Pharmaceutics, 2021, 13(12). https://doi.org/10.3390/pharmaceutics13121991.

[15] Kluwe F, Michelet R, Huisinga W, et al. Towards model-informed precision dosing of voriconazole: Challenging published voriconazole nonlinear mixed-effects models with real-world clinical data. Clinical pharmacokinetics, 2023, 62(10): 1461-1477. https://doi.org/10.1007/s40262-023-01274-y.

[16] Shi C, Xiao Y, Mao Y, et al. Voriconazole: A review of population pharmacokinetic analyses. Clinical pharmacokinetics, 2019, 58(6): 687-703. https://doi.org/10.1007/s40262-019-00735-7.

[17] Chaudhri K, Stocker S L, Williams K M, et al. Voriconazole: An audit of hospital-based dosing and monitoring and evaluation of the predictive performance of a dose-prediction software package. The Journal of antimicrobial chemotherapy, 2020, 75(7): 1981-1984. https://doi.org/10.1093/jac/dkaa098.

[18] Jin H, Wang T, Falcione B A, et al. Trough concentration of voriconazole and its relationship with efficacy and safety: A systematic review and meta-analysis. The Journal of antimicrobial chemotherapy, 2016, 71(7): 1772-1785. https://doi.org/10.1093/jac/dkw045.

[19] Khan-Asa B, Punyawudho B, Singkham N, et al. Impact of albumin and omeprazole on steady-state population pharmacokinetics of voriconazole and development of a voriconazole dosing optimization model in thai patients with hematologic diseases. Antibiotics (Basel, Switzerland), 2020, 9(9): https://doi.org/10.3390/antibiotics9090574.

[20] Han K, Capitano B, Bies R, et al. Bioavailability and population pharmacokinetics of voriconazole in lung transplant recipients. Antimicrobial agents and chemotherapy, 2010, 54(10): 4424-4431. https://doi.org/10.1128/aac.00504-10.

[21] Han K, Bies R, Johnson H, et al. Population pharmacokinetic evaluation with external validation and bayesian estimator of voriconazole in liver transplant recipients. Clinical pharmacokinetics, 2011, 50(3): 201-214. https://doi.org/10.2165/11538690-000000000-00000.

[22] van den Born D A, Märtson A G, Veringa A, et al. Voriconazole exposure is influenced by inflammation: A population pharmacokinetic model. International journal of antimicrobial agents, 2023, 61(4): 106750. https://doi.org/10.1016/j.ijantimicag.2023.106750.

[23] Muto C, Shoji S, Tomono Y, et al. Population pharmacokinetic analysis of voriconazole from a pharmacokinetic study with immunocompromised japanese pediatric subjects. Antimicrobial agents and chemotherapy, 2015, 59(6): 3216-3223. https://doi.org/10.1128/aac.04993-14.

[24] Dolton M J, Mikus G, Weiss J, et al. Understanding variability with voriconazole using a population pharmacokinetic approach: Implications for optimal dosing. The Journal of antimicrobial chemotherapy, 2014, 69(6): 1633-1641. https://doi.org/10.1093/jac/dku031.

[25] Kim Y, Rhee S J, Park W B, et al. A personalized CYP2C19 phenotype-guided dosing regimen of voriconazole using a population pharmacokinetic analysis. Journal of clinical medicine, 2019, 8(2): https://doi.org/10.3390/jcm8020227.

[26] Karlsson M O, Lutsar I, Milligan P A. Population pharmacokinetic analysis of voriconazole plasma concentration data from pediatric studies. Antimicrobial agents and chemotherapy, 2009, 53(3): 935-944. https://doi.org/10.1128/aac.00751-08.

[27] Akbar Z, Usman M, Aamir M, et al. Population pharmacokinetic analysis of intravenous voriconazole in cancer patients. PloS one, 2025, 20(3): e0318883. https://doi.org/10.1371/journal.pone.0318883.

[28] Li Z W, Peng F H, Yan M, et al. Impact of CYP2C19 genotype and liver function on voriconazole pharmacokinetics in renal transplant recipients. Therapeutic drug monitoring, 2017, 39(4): 422-428. https://doi.org/10.1097/ftd.0000000000000425.

[29] Chen C, Yang T, Li X, et al. Population pharmacokinetics of voriconazole in chinese patients with hematopoietic stem cell transplantation. European journal of drug metabolism and pharmacokinetics, 2019, 44(5): 659-668. https://doi.org/10.1007/s13318-019-00556-w.

[30] Ren Q X, Li X G, Mu J S, et al. Population pharmacokinetics of voriconazole and optimization of dosage regimens based on monte carlo simulation in patients with liver cirrhosis. Journal of pharmaceutical sciences, 2019, 108(12): 3923-3931. https://doi.org/10.1016/j.xphs.2019.09.019.

[31] Wang T, Yan M, Tang D, et al. Using child-pugh class to optimize voriconazole dosage regimens and improve safety in patients with liver cirrhosis: Insights from a population pharmacokinetic model-based analysis. Pharmacotherapy, 2021, 41(2): 172-183. https://doi.org/10.1002/phar.2474.
[32] Li S, Wu S, Gong W, et al. Application of population pharmacokinetic analysis to characterize CYP2C19 mediated metabolic mechanism of voriconazole and support dose optimization. Frontiers in pharmacology, 2021: 12730826. https://doi.org/10.3389/fphar.2021.730826.
[33] Wu Y, Lv C, Wu D, et al. Dosage optimization of voriconazole in children with haematological malignancies based on population pharmacokinetics. Journal of clinical pharmacy and therapeutics, 2022, 47(12): 2245-2254. https://doi.org/10.1111/jcpt.13801.
[34] Hu L, Huang S, Huang Q, et al. Population pharmacokinetics of voriconazole and the role of CYP2C19 genotype on treatment optimization in pediatric patients. PloS one, 2023, 18(9): e0288794. https://doi.org/10.1371/journal.pone.0288794.
[35] Wang J, Shen Y, Wu Z, et al. Population pharmacokinetics of voriconazole and dose optimization in elderly chinese patients. Journal of clinical pharmacology, 2023. https://doi.org/10.1002/jcph.2357.
[36] Ling J, Yang X, Dong L, et al. Influence of c-reactive protein on the pharmacokinetics of voriconazole in relation to the CYP2C19 genotype: A population pharmacokinetics analysis. Frontiers in pharmacology, 2024: 151455721. https://doi.org/10.3389/fphar.2024.1455721.
[37] Wang J, Xu H, Li R, et al. Model-oriented dose optimization of voriconazole in critically ill children. Antimicrobial agents and chemotherapy, 2021, 65(9): e0049321. https://doi.org/10.1128/aac.00493-21.
[38] Tang D, Yan M, Song B L, et al. Population pharmacokinetics, safety and dosing optimization of voriconazole in patients with liver dysfunction: A prospective observational study. British journal of clinical pharmacology, 2021. 87(4): 1890-1902. https://doi.org/10.1111/bcp.14578.
[39] Jiang Z, Wei Y, Huang W, et al. Population pharmacokinetics of voriconazole and initial dosage optimization in patients with talaromycosis. Frontiers in pharmacology, 2022: 13982981. https://doi.org/10.3389/fphar.2022.982981.
[40] Lin X B, Lui K Y, Guo P H, et al. Population pharmacokinetic model-guided optimization of intravenous voriconazole dosing regimens in critically ill patients with liver dysfunction. Pharmacotherapy, 2022, 42(1): 23-33. https://doi.org/10.1002/phar.2634.
[41] Liu Y, Qiu T, Liu Y, et al. Model-based voriconazole dose optimization in chinese adult patients with hematologic malignancies. Clinical therapeutics, 2019, 41(6): 1151-1163. https://doi.org/10.1016/j.clinthera.2019.04.027.
[42] Wang H, Shen Y, Luo X, et al. Population pharmacokinetics and dose optimization of voriconazole in patients with covid-19-associated pulmonary aspergillosis. Frontiers in pharmacology, 2025: 161554370. https://doi.org/10.3389/fphar.2025.1554370.
[43] Chen W, Xie H, Liang F, et al. Population pharmacokinetics in china: The dynamics of intravenous voriconazole in critically ill patients with pulmonary disease. Biological & pharmaceutical bulletin, 2015, 38(7): 996-1004. https://doi.org/10.1248/bpb.b14-00768.
[44] Tang D, Song B L, Yan M, et al. Identifying factors affecting the pharmacokinetics of voriconazole in patients with liver dysfunction: A population pharmacokinetic approach. Basic & clinical pharmacology & toxicology, 2019, 125(1): 34-43. https://doi.org/10.1111/bcpt.13208.
[45] Suetsugu K, Muraki S, Fukumoto J, et al. Effects of letermovir and/or methylprednisolone coadministration on voriconazole pharmacokinetics in hematopoietic stem cell transplantation: A population pharmacokinetic study. Drugs in R&D, 2021, 21(4): 419-429. https://doi.org/10.1007/s40268-021-00365-0.
[46] Walsh T J, Driscoll T, Milligan P A, et al. Pharmacokinetics, safety, and tolerability of voriconazole in immunocompromised children. Antimicrobial agents and chemotherapy, 2010, 54(10): 4116-4123. https://doi.org/10.1128/aac.00896-10.
[47] Takahashi T, Mohamud M A, Smith A R, et al. CYP2C19 phenotype and body weight-guided voriconazole initial dose in infants and children after hematopoietic cell transplantation. Antimicrobial agents and chemotherapy, 2021, 65(9): e0062321. https://doi.org/10.1128/aac.00623-21.
[48] Liu S, Yao X, Tao J, et al. Impact of CYP2C19, CYP2C9, CYP3A4, and FMO3 genetic polymorphisms and sex on the pharmacokinetics of voriconazole after single and multiple doses in healthy chinese subjects. Journal of clinical pharmacology, 2024, 64(8): 1030-1043. https://doi.org/10.1002/jcph.2440.
[49] Gautier-Veyret E, Fonrose X, Stanke-Labesque F. A genetic score combining CYP450 2C19 and 3A4 genotypes to predict voriconazole plasma exposure? International journal of antimicrobial agents, 2016, 48(2): 221-222. https://doi.org/10.1016/j.ijantimicag.2016.05.002.
[50] He H R, Sun J Y, Ren X D, et al. Effects of CYP3A4 polymorphisms on the plasma concentration of voriconazole. European journal of clinical microbiology & infectious diseases: official publication of the European Society of Clinical Microbiology, 2015, 34(4): 811-819. https://doi.org/10.1007/s10096-014-2294-5.
[51] Shao B, Ma Y, Li Q, et al. Effects of cytochrome P450 3A4 and non-genetic factors on initial voriconazole serum trough concentrations in hematological patients with different cytochrome P450 2C19 genotypes. Xenobiotica; the fate of foreign compounds in biological systems, 2017, 47(12): 1121-1129. https://doi.org/10.1080/00498254.2016.1271960.
[52] Boglione-Kerrien C, Zerrouki S, Le Bot A, et al. Can we predict the influence of inflammation on voriconazole exposure? An overview. The Journal of antimicrobial chemotherapy, 2023. https://doi.org/10.1093/jac/dkad293.

[53] Organization W H. Who model list of essential medicines, 2017a. https://doi.org/10.1080/00498254.2022.2025628.
[54] Xie J, Yang Q, Han X, et al. Pharmacokinetic/pharmacodynamic target attainment of different antifungal agents in de-escalation treatment in critically ill patients: A step toward dose optimization using monte carlo simulation. Antimicrobial agents and chemotherapy, 2022, 66(6): e0009922. https://doi.org/10.1128/aac.00099-22.
[55] Maertens J, Pagano L, Azoulay E, et al. Liposomal amphotericin b-the present. The Journal of antimicrobial chemotherapy, 2022, 77(Suppl_2): ii11-ii20. https://doi.org/10.1093/jac/dkac352.
[56] Tissot F, Agrawal S, Pagano L, et al. Ecil-6 guidelines for the treatment of invasive candidiasis, aspergillosis and mucormycosis in leukemia and hematopoietic stem cell transplant patients. Haematologica, 2017, 102(3): 433-444. https://doi.org/10.3324/haematol.2016.152900.
[57] Huang W, Zheng Y, Huang H, et al. External evaluation of population pharmacokinetic models for voriconazole in chinese adult patients with hematological malignancy. European journal of clinical pharmacology, 2022, 78(9): 1447-1457. https://doi.org/10.1007/s00228-022-03359-2.
[58] Kiang T K, Sherwin C M, Spigarelli M G, et al. Fundamentals of population pharmacokinetic modelling: Modelling and software. Clinical pharmacokinetics, 2012, 51(8): 515-525. https://doi.org/10.1007/bf03261928.

Eurasia Journal of Science and Technology
Print ISSN: 2663-1024
Online ISSN: 2663-1016
DOI: https://doi.org/10.61784/ejst3113

BASED ON UNITY3D, TWO-PLAYER COOPERATION CAPTURES THE DESIGN AND IMPLEMENTATION OF THE GOBLIN GAME "INK WALKER"

Yue Zhou
College of Fine Arts, Guangdong Polytechnic Normal University, Guangzhou 510665, Guangdong, China.
Corresponding Email: 13302855472@163.com

Abstract: This paper takes *Ink Walker*, a Chinese-style two-player cooperative goblin-catching game developed based on the Unity3D engine, as the research object. Combining practical experience from Game Jam competitions, it explores the design and implementation process of the game. The research centers on three core goals: the visual design of Chinese-style elements, the innovation of two-player collaboration mechanisms, and the cross-platform technical implementation. It unfolds from aspects such as artistic concept design (including the setting of world view and plot, the visual design of characters, goblins, scenes and UI), technical indicators and research methods (covering technical foundations and development toolchains, the technical implementation of core gameplay, system architecture and performance optimization), and performance optimization strategies. By integrating Chinese-style culture with game design, innovating two-player collaboration mechanisms, utilizing Unity3D to realize cross-platform development and conduct performance optimization, it provides technical solutions and creative paradigms for the development of similar Chinese-style games, and has certain theoretical and practical significance.
Keywords: *Ink Walker*; Unity3D; Two-player cooperation; Goblin catching; Chinese style; Game design and implementation

1 INTRODUCTION

1.1 Research Background and Significance

At a time when digital media art and game design technology are deeply integrated, two-player cooperative games have become a popular field in the game industry with their unique social attributes and creative gameplay. As players' requirements for gaming experience continue to improve, games that integrate multicultural elements and innovative interaction mechanisms are becoming more and more popular. As a treasure of the traditional culture of the Chinese nation, national style culture contains rich artistic value and cultural connotation, providing a broad source of creativity for game design. Integrating national style elements into two-player cooperative games can not only meet players' pursuit of cultural diversity, but also spread and promote the excellent traditional Chinese culture through the medium of games.

Based on the author's practical experience in participating in Game Jam competitions, this study takes the self-developed game "Ink Walker" as a specific case to explore how to use the Unity3D engine to achieve a two-player cooperative game with national style to catch goblins. As a widely used game development engine, Unity3D has strong cross-platform development capabilities, rich plug-in resources, and a convenient operation interface, providing efficient technical support for game development. By analyzing the design and implementation process of "Ink Walker", it aims to provide technical solutions and creative paradigms with reference value for the development of similar games, and promote the development of national style theme games in technological innovation and cultural expression.

1.2 Research Objectives and Content

This study focuses on the three core goals of "visual design of national style elements", "innovation of two-person collaboration mechanism" and "cross-platform technology realization", and constructs a complete research framework covering art concept design, gameplay logic development, and system architecture construction. In terms of art concept design, we will dig deep into the artistic elements in the national style culture, such as green landscapes, traditional mythological creatures, etc., and transform them into character images, scene design and special effects in the game, showing the unique charm of the national style culture; In terms of gameplay logic development, the two-person cooperation mechanism is innovatively designed, combining the five elements and the goblin capture gameplay to bring players a novel gaming experience; During the system architecture construction process, the characteristics of the Unity3D engine are used to achieve stable operation of the game on multiple platforms, optimize game performance, and improve the smoothness of the game.

The specific research content includes: analyzing the application of national style elements in game art design, and explaining how to visualize national style culture from the aspects of character design, scene construction, and special effects production; Explore the innovative design of two-player cooperation mechanism in gameplay, such as skill cooperation between players and division of tasks. Research game development technologies based on the Unity3D

engine, including scripting, physics system application, resource management, etc. Evaluate the creativity, interactivity and technical implementation effect of the game, analyze the advantages and disadvantages of the game through player testing and feedback, and put forward improvement directions and future prospects.

2 GAME CONCEPT DESIGN AND CREATIVE CONSTRUCTION

2.1 World View and Plot Setting

(1) Mythological Worldview: "Ink Walker" builds a unique Guofeng mythological worldview, with "Ink Walker" as the core profession, integrating ink and natural elements into a unique spell system to create a fantasy world of Xianxia. In this world, painters are known as "inkwalkers" who have the ability to manipulate ink with natural elements, allowing them to merge the two to create magical spells. This setting cleverly combines the elements of pen and ink in traditional Chinese culture with natural philosophical concepts, giving the game a unique cultural heritage.
The main capture object in the game, the "Painting Spirit", is a creation spirit created by nature and ink, that is, the fairy. These fairies have a wealth of attribute settings, including five single attributes of "gold, wood, water, fire, and earth" and 10 dual attributes formed by combining two of them. This attribute setting not only enriches the gameplay of the game, but also echoes the traditional Chinese theory of the five elements, bringing players a more in-depth gaming experience. For example, the Gold Elemental Elves may have a hard shell and powerful attack power, while the Wood Elemental Fairies may be good at healing and controlling, and players need to use corresponding strategies and skills to capture them according to the attributes and characteristics of different Fairies.
(2) Level narrative structure: The game has five major levels, namely "Green Ridge", "Sunset Mountain", "Broken River", "Purple Shirt Ze" and "Youqu Path", each level has a unique scene style and fairy type, through the gradual unlocking of levels, gradually expand the game world view[1]. Map Level Design in the Game "Ink Walker" can be seen in Figure 1.

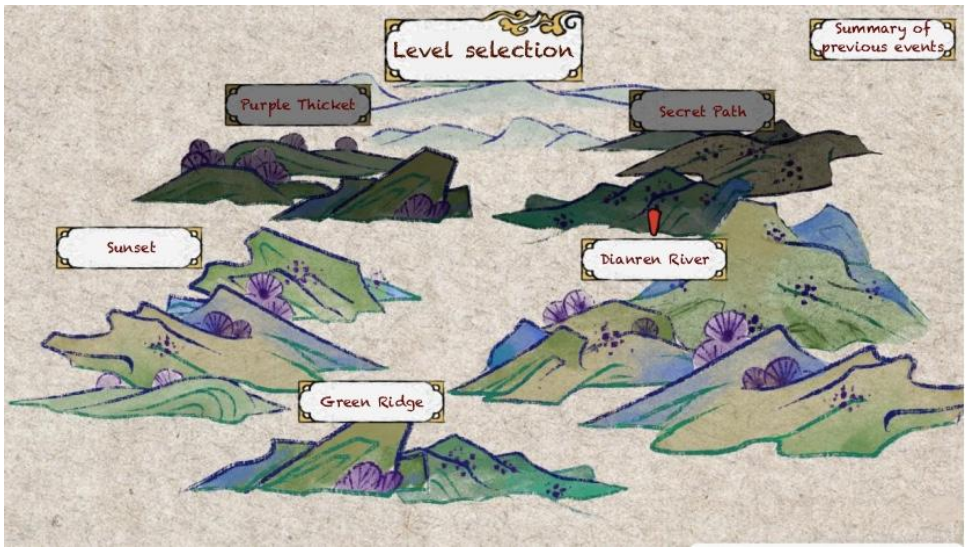

Figure 1 Map Level Design in the Game "Ink Walker"

As the starting level of the game, "Green Ridge" uses pastel ink to render the scene of cascading mountains, creating a fresh and tranquil atmosphere and presenting players with a natural world full of life. In this level, players mainly encounter wood and water fairies, which are integrated with the scene, such as vine-entwined wood element fairies and water element fairies, guiding players to have a preliminary understanding of the game's world view and gameplay.
As the level progresses, "Sunset Mountain" is set against the backdrop of the sunset maple forest, and the maple leaves are like fire, dyeing the entire mountain forest orange-red, creating a serene and slightly mysterious atmosphere. In this level, in addition to wood and water fairies, there will also be fire fairies, and their forms may be combined with burning flames, such as flame birds, fire foxes, etc., and their fiery attributes echo the afterglow of the sunset in the scene, adding to the visual impact and challenge of the game.
"Broken Renchuan" shows the steep terrain through the fractured canyon and flowing ink, the canyon is deep, the water is fast, and the flow of ink adds a bit of mystery and danger. Here, players will encounter metallic and earth-attribute fairies, which may appear in mechanical metal forms and have strong defense and attack power; Earth attribute fairies may be combined with rocks and soil, and are good at defending and controlling terrain, such as rock giants, earth element puppets, etc., and players need to deal with these goblins in complex terrain to further experience the richness and challenge of the game world.
In "Purple Shirt", the purple mist fills the swamp, mysterious and deep, as if hiding endless secrets. In this level, the types and numbers of dual-attribute goblins gradually increase, such as wood and water dual-attribute goblins, they may have the agility of water and the healing power of wood, and players need to use skills and strategies more flexibly to successfully subdue these goblins and explore this mysterious world in depth

The final "Youqu Trail" is a deep and winding trail as the main scene, lined with dense bamboo forests and ancient buildings, and moonlight shines on the ground through the bamboo leaves, creating a quiet and mysterious atmosphere. In this level, goblins of various attributes gather, and players need to give full play to their wisdom and operating skills, match skills reasonably, and work closely with teammates to complete the final challenge and reveal the secrets behind the game world. This kind of design that gradually enriches the game content and world view through the narrative structure of the level can attract players to continue to explore and deeply experience the mythical world of the national style created by the game.

2.2 The Creativity of Art Concept Design

2.2.1 Character and goblin visual design

(1) Protagonist design: As the protagonists of the game, the painter brother and sister use a very distinctive ink style character design. Their costume design cleverly incorporates elements such as brushes and rice paper, reflecting the professional characteristics of "ink walkers". For example, the senior brother's robe may have the texture of brush strokes drawn on it, and the cuffs and neckline are designed with the texture of rice paper, which seems to have the fragrance of ink when fluttering in the wind; The junior sister's costume may be based on light ink colors, with streamers made of rice paper, on which exquisite ink patterns are drawn, such as plum blossoms, bamboo, etc., showing the softness and agility of female characters(Figure 2).

Figure 2 "Ink Walker" Begins the Visual Design of the Game Interface

When the skill is released, the character will present the special effect of ink diffusion, which further strengthens the expression of national style elements. When the senior brother uses the gold skill, the golden ink will spread out from the brush tip like lightning, and after hitting the target, golden ink patterns will appear around it[2], as if the luster of metal shines in the ink color; When the junior sister uses the water skill, the blue ink will ripple like water waves, forming a circular water curtain that envelops the target, and a faint cuttlefish pattern will appear on the water curtain, vividly showing the agility and softness of the water. The design of this skill special effect not only increases the visual impact of the game, but also allows players to feel the unique spell charm of "Ink Walker" during operation.

(2) Fairy form innovation: The form design of the fairy combines the characteristics of the strange beasts of the "Classic of Mountains and Seas" with the modern Q version aesthetics, realizing the expression of "rejuvenation of traditional elements". Taking the "Golden Element Fairy" as an example, its shape borrows from some metallic beasts in the "Classic of Mountains and Seas", while incorporating the rounded lines and cute expressions of the modern Q version style, making it not only have the heritage of traditional culture, but also conform to the aesthetic taste of contemporary players. Its body surface is covered with mechanical metal patterns, which not only add to the sense of technology of the fairy, but also hint at the hardness and sharpness of the gold element. Its eyes may be designed as shimmering red gemstones, like burning flames, revealing the fiery heat and power of the gold element[3].

Figure 3 The Fairy Form Card that the Player needs to Capture
(Displayed in the Upper Left Corner of the Game Interface)

As shown in Figure 3, the "Wood Element Fairy" incorporates the forms of vines and flowers, showing the vitality and vitality of nature. Its body may be wrapped in vines, forming a cute animal shape, such as a rabbit, a fawn, etc., and bright flowers grow on the vines, gently swaying with the movements of the goblins, emitting a charming fragrance. Its ears or tail may be made of long vines dotted with crystal dewdrops, as if it were an elf who has just awakened in the forest in the early morning. This design that combines traditional elements with modern aesthetics makes the image of the goblin more vivid and interesting, and is easy to accept and love by players.

2.2.2 Scene and UI visual language

(1) Scene composition: The game scene composition uses the technique of Chinese landscape painting "high, far-reaching, and flat" to build a multi-level explorable map, bringing players a rich visual experience and exploration fun. In the "Green Ridge" level, the layered mountains are rendered with pastel ink painting, using the high distance method, and the distant peaks are obscured by the tall mountains nearby, creating a sense of towering into the sky, making players feel like they are in the majestic mountains. The clouds and mist are swirling between the mountains, and the use of blank space to express the ethereal nature of the clouds and mist, leaving players with room for imagination. At the same time, some paths, streams and pavilions are cleverly arranged in the picture to guide the player's eye deep into the picture [4] and increase the sense of layering and depth of the scene.

The "Broken River" level expresses the steep terrain through the fractured canyon and flowing ink, using the far-reaching method. The cliffs on both sides of the canyon are towering and steep, shading each other and forming a deep canyon space. As players move forward through the canyon, they will see the canyon in the distance gradually disappear into the ink-colored fog, as if bottomless, adding to the mystery and danger of the scene. The water at the bottom of the canyon flows rapidly, expressing the dynamics of the water flow with flowing ink lines, and the splashing places are embellished with white ink dots, vividly showing the power and speed of the water flow.

(2)UI interaction design: UI interactive design adopts scroll-style menus and stamp-style buttons, and the skill selection interface is presented as a "nine-square grid inkstone", which strengthens the recognition of the national style. The design of the scroll-style menu is inspired by ancient Chinese calligraphy and painting scrolls, when the player opens the menu, the menu slowly unfolds like a scroll, and the text and icons on it are presented in quaint calligraphy fonts and traditional patterns, giving players the feeling of flipping through ancient books[5]. The stamp button imitates the shape and texture of traditional Chinese seals, and the buttons are engraved with simple patterns or text, such as skill icons, function names, etc., and when the player clicks on the button, the special effects under the seal will appear, increasing the fun and ritual of the operation.

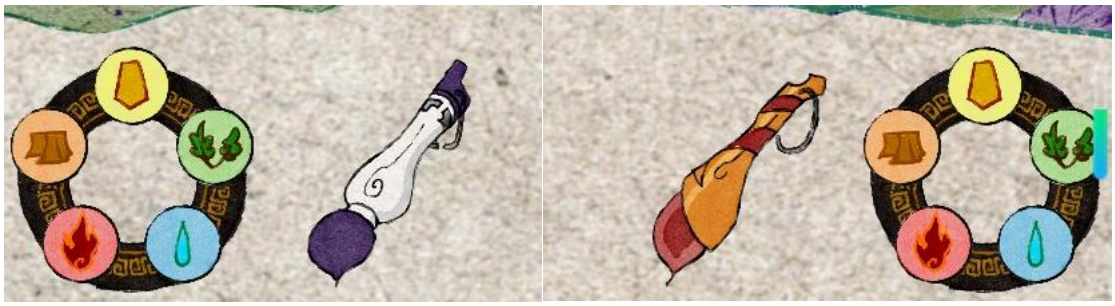

Figure 4 The Color Palette Props Operated by the Two Players Respectively (Player 1 Left, Player 2 Right)

As shown in Figure 4, the skill selection interface is presented as a "nine-square grid inkstone", placing the skill icons in the game in the nine grids of the inkstone, and there are also faint ink marks drawn around each grid, as if they are traces left by a brush that has just dipped ink. When the player selects a skill, the corresponding grid in the inkstone will light up, and the ink color will flow with it, creating an elegant and quaint atmosphere. This UI design not only aligns with the game's national style theme, but also brings players a unique interactive experience, allowing players to feel the charm of traditional Chinese culture during operation[6].

3 TECHNICAL INDICATORS AND RESEARCH METHODS

3.1 Technical Foundation and Development Tool Chain

3.1.1 Unity3D engine core feature application

(1) Cross-platform architecture: With the help of IL2CPP technology, "Ink Walker" realizes the compilation of multiple platforms such as Windows, Android, and iOS. IL2CPP compiles C# code into CIL intermediate language, then converts it into C++ code, and finally generates machine code by C++ compilers on each platform, greatly improving code execution efficiency and cross-platform compatibility[7].On different devices, through dynamic resolution adjustment, the resolution is automatically adapted according to the device performance and screen parameters, combined with the optimized resource loading strategy, to ensure that the game frame rate is stable above 60fps, providing players with a smooth gaming experience.

(2) Visual development toolchain: Based on the Unity Editor, developers can efficiently build scenes. Using the Tilemap component, 2D level maps such as "Green Green Ridge" and "Sunset Mountain" are quickly constructed by splicing tiles, and its rich editing tools and flexible tile combination methods greatly improve the efficiency of map creation. The Animator controller is used to manage the character action state machine, and by defining different animation states and conversion conditions, it realizes the natural switching of character actions, such as from standing to walking, running, and skill release actions, etc., which improves the development efficiency by more than 30% compared to traditional animation management methods.

3.1.2 Technology stack and resource management

(1) Art resource pipeline: Art resource production adopts the "Blender modeling→ Substance Painter texture→ Unity resource library management" process. In Blender, polygon modeling, sculpting, and other techniques are used to create high-precision characters, goblins, and scene models. Then, in Substance Painter, use intelligent materials and drawing functions to generate realistic texture maps; Finally, the Unity resource library was imported, and a standardized asset naming convention and version control process were established, achieving a 40% reuse rate of art assets and reducing duplicate production workload.

(2) Scripting system design: Use C# language to write core logic and implement role control based on MonoBehavior components. Take character movement control as an example, achieve 8 directions of movement, set skill cooldowns, and limit the frequency of skill releases to ensure the balance and strategy of the game. Introduce object pool technology to manage goblin generation, create a certain number of goblin objects in advance and store them in the object pool, directly obtain them when needed, and put them back after use, effectively reducing memory peaks by 25% and improving game performance.

3.2 Implementation of Core Gameplay Technology

3.2.1 Development of two-person collaboration mechanism

(1) Network synchronization solution: A client-server architecture is built based on the Unity Networking module, where the server controls the overall state of the game, and the client is responsible for displaying information and sending operation instructions. Key operations such as skill release and goblin capture are synchronized with the help of RPC remote procedure call mechanism to ensure the consistent state of all clients. In response to the network latency problem, a predictive compensation algorithm is introduced, and the client locally predicts the operation results and displays them, and at the same time sends instructions to the server for verification and correction, and finally sends the synchronization information back to the client for adjustment, successfully controlling the synchronization delay of two-player operation within 150ms to ensure smooth game interaction.

(2) Division of labor and cooperation system: Clarify the role positioning of "ink attack" high output and "stick" strong control. Through the visualization of the skill range, the skill release range is clearly displayed in the game interface, which is convenient for players to cooperate. Real-time location tags keep players informed about the location of their teammates. Designed combined skills such as "Elemental Resonance", which require the overlapping skill areas of the two characters to trigger, such as "Water and Fire Blending", Ink Attack Fire Attribute Skills, and Stick Water Attribute Skills, combined with steam generating areas to cause damage and interference, greatly improving the depth of game strategy(Figure 5).

Figure 5 Player 1 is Capturing the Operation Screen of the Fire Elementary Fairy

3.2.2 Element and level system implementation

(1) Five elements mutual restraint algorithm: Construct an attribute restraint matrix, single-attribute goblins follow the basic rules of "gold and wood, wood and earth, earth and water, water and fire, and fire and gold", and dual-attribute fairies need to be covered by dual attributes to successfully capture. For example, when a metallic skill attacks a wood-attribute fairy, the ray detects whether the skill range covers the goblin, and combines the collision algorithm to determine whether it hits or not to achieve accurate capture judgment.

(2) Dynamic difficulty curve: Dynamically adjust the difficulty according to the player's historical clearance time, and the proportion of dual-attribute goblins will gradually increase to 60% after the 3rd level, while increasing the

movement speed of goblins. With the increasing complexity of the terrain, such as the dynamic water flow collision detection in the "Broken River" level, when players cross the river, the water flow will affect the movement of the character, so it needs to be carefully dealt with, forming a gradient experience from beginner-friendly to expert challenges to meet the needs of players of different levels.

3.3 System Architecture and Performance Optimization

3.1.1 Core module development

(1) Character control system: supports keyboard/controller dual operation adaptation, and realizes cross-platform input management through the Input System component to adapt to different player operating habits. Keyboard operation uses W, A, S, D to control movement, and number keys 1 - 5 release skills; The handle operation uses the left joystick to control the movement, the right joystick adjusts the viewing angle, and the function button releases the skill. Introducing the "Ink Energy Bar" mechanism, skill release consumes energy, and energy recovers over time, limiting players' high-frequency operations and prompting players to reasonably plan the timing of skill release(Figure 6).

Figure 6 Player's Operation Prompt Key Interface

(2)Collision and physics system: Combines Box Collider 2D and Polygon Collider 2D components to achieve complex terrain interaction. Box Collider 2D is used for collision detection of regularly shaped objects such as rectangles, while Polygon Collider 2D creates colliders with a conforming shape for irregular objects such as rocks and trees. Utilize the PhysX engine to simulate physical blocking effects in ink areas, such as player-drawn ink barriers that block goblin action, ensuring smooth feedback of character movements and skill releases, enhancing game realism.

4 PERFORMANCE OPTIMIZATION STRATEGIES

(1) Rendering optimization: Use occlusion culling technology to mark occlusion and occlusion objects in the scene to avoid rendering completely occluded objects and reduce invalid rendering objects. Through LOD (Level of Detail) hierarchical processing, the model detail level is dynamically switched according to the camera distance, high-detail models are displayed at close range, and low-detail models are used at a distance to improve scene loading speed, reducing rendering time by 40% in complex mobile scenes.

(2) Memory management: Use object pool technology to reuse goblins and skill special effects objects to avoid performance overhead caused by frequent creation and destruction; Coordinate with the Profiler tool to monitor memory allocation in real time, detect memory leaks and irrational allocations in a timely manner, and strictly control the peak memory usage of mobile devices within 500MB to ensure stable game operation(Figure 7).

Figure 7 The Game Screen of the Player Playing the Game

5 CONCLUSION

This study conducts an in-depth analysis of the design and implementation process of "Ink Walker", a two-player game based on Unity3D that captures fairies, and constructs a game development framework that integrates national style aesthetics and two-player collaborative gameplay, providing a technical solution and creative paradigm with reference value for the development of similar games.

In terms of art concept design, through the modern translation of national style elements, the low-poly ink rendering style was created, and the Q version of the goblin image was designed, realizing the organic combination of tradition and modernity. Using the scene-based expression of visual narrative, the game world view and plot are integrated into the details of the level scenes, bringing players an immersive narrative experience. In terms of gameplay design, the innovative two-player cooperation mechanism and dynamic difficulty adaptation system increase the strategic depth and playability of the game, meeting the gaming needs of different players.

At the technical implementation level, the characteristics of the Unity3D engine are used to realize core functions such as cross-platform development, character control, scene construction, collision detection, and two-player collaboration, and ensure the smooth operation of the game and a good user experience by optimizing the network synchronization mechanism and improving performance.

Through player testing and feedback, the feasibility and effectiveness of the game in terms of art creativity, gameplay design and technical implementation are verified. However, the game still has some shortcomings, such as the intelligence of AI behavior needs to be improved, and the difficulty balance of later levels needs to be further optimized.

In the future, with the continuous development of artificial intelligence, virtual reality and other technologies, Guofeng digital games are expected to achieve greater breakthroughs in technological innovation and cultural expression. The application of AI intelligence in games can be further deepened, such as developing smarter goblin AI, which can respond more flexibly based on player behavior; Strengthen UGC content creation, allowing players to participate in the generation of game content, and increase the fun and social nature of the game. explore the integration with more cultural IPs, expand the cultural connotation and market influence of games, and promote the global dissemination of national style digital games.

To sum up, this study not only provides a direction for the subsequent optimization and development of "Ink Walker", but also provides a useful reference for the exploration of technological innovation and cultural inheritance of national style games, which has certain theoretical and practical significance.

COMPETING INTERESTS

The authors have no relevant financial or non-financial interests to disclose.

REFERENCES

[1] Liu Jiaxin, Gao Tingting. Research on the development and design of a new immersive game model based on digital tourism experience - Taking Tai'an City as an example. Zhongyuan Culture and Tourism, 2024(14): 19-21.

[2] Liu Ninghui, Song Jinyu. Design and development of ink-and-wash text adventure game based on Unity3D. Software Engineering and Applications, 2022, 11 (4): 779-787. DOI: 10.12677/SEA.2022.114081.

[3] Bao Yanrong, Zhou Xiaowen, Tang Annan. Cross-dimensional digital expression of Dunhuang culture: 2D+3D game development based on Unreal Engine. Journal of North University of China (Social Sciences Edition), 2025.

[4] Zhang Shiyu. Design and development of VR games based on traditional Lingnan garden themes. Guangzhou: Guangzhou University, 2024. DOI: 10.27040/d.cnki.ggzdu.2024.000577.

[5] Pan Tianshou, Xu Jianrong. The style of traditional Chinese painting. Shanghai: Shanghai Painting and Calligraphy Publishing House, 2003: 198-200.

[6] Zheng Zhiqiang. Research on the design and development of digital entertainment system for the elderly based on somatosensory. Shanghai: Shanghai Jiaotong University, 2013.

[7] Huang Zhanpeng. Unity3D game development. Beijing: People's Posts and Telecommunications Press, 2023: 312.

Eurasia Journal of Science and Technology
Print ISSN: 2663-1024
Online ISSN: 2663-1016
DOI: https://doi.org/10.61784/ejst3114

INDUSTRIAL AND SUPPLY CHAIN COORDINATION AND SUSTAINABLE DEVELOPMENT IN WESTERN CHINA UNDER THE DIGITAL ECONOMY

LingYan Sun
Silk Road Economic Belt Core Area Industrial High-quality Development Research Center, Business School, Xinjiang Normal University, Urumqi 830054, Xinjiang, China.
Corresponding Email: linda.1sunny@163.com

Abstract: With the rapid development of the digital economy, big data, cloud computing, the Internet of Things and artificial intelligence have driven a new round of industrial transformation. In this process, data has gradually become the core driving factor, not only reconfiguring the collaborative mechanism between the industrial chain and the supply chain, but also promoting the sustainable development of the overall operation. This study, based on the background of the development of the digital economy, focuses on the western region of China and explores how regional industrial chains and supply chains can coordinate and interact to achieve sustainable economic development. Starting from the enabling mechanism of the digital economy, this article deeply analyzes the internal logic of the "dual-chain" synergy and its specific impact on regional sustainable development. This article expands the analytical framework of the collaboration between industrial chains and supply chains at the theoretical level and the mechanism of digital economy empowering the linkage and driving sustainable development of industrial chains and supply chains. Further, based on the current development status of industrial chains in the western region and the challenges and current situation faced by the development of the digital economy, corresponding suggestions are put forward. This research further enriches the relevant theories on digital economy and regional sustainable development, providing a reference basis for enhancing the economic and social development level of the western region with the aid of digital technology.
Keywords: Supply chain; Industrial chain; Sustainable development; Digital economy

1 INTRODUCTION

The rapid development of information technology has made the digital economy an important force driving economic growth. It has not only changed the structure of traditional industrial and supply chains but also reshaped their operational logic. Empowered by digital technology, supply chains have become more flexible and efficient, and the flow of information and resources between regions and industries has significantly accelerated. This transformation not only supports sustained economic growth but also makes development more resilient. The synergy between industrial and supply chains has led to improved production efficiency and optimized resource utilization, directly enhancing economic competitiveness. More importantly, it is becoming a crucial path for promoting sustainable development strategies, striving for the simultaneous growth of economic, social, and environmental benefits [1].

The western region, as the strategic depth and important barrier of China's economic development, is undergoing profound changes in the reshaping and upgrading of its supply chain and industrial chain, which are deeply integrated with sustainable development. This is a promising yet challenging situation. From the perspective of the supply chain, the western region of China is experiencing a profound role transformation. With the continuous construction of major infrastructure such as the land-sea new channel of the China-Singapore connectivity project and the China-Europe freight train, this region has transformed from a region with lower openness and relatively lagging economy to a core land-based channel connecting the "Belt and Road Initiative" and directly reaching Central Asia and Europe. This characteristic of its geographical location has driven its supply chain function to shift from passively accepting industrial transfer from the east to actively building a cross-regional connection network, becoming an important fortress to ensure the security of the national industrial chain and supply chain and the smooth circulation of the domestic and international dual circulations [2]. At the industrial chain level, the western region has not simply replicated the development model of the east, but has based itself on its own resource endowment and taken a distinctive and clustered path. Its development process focuses on building a characteristic modern industrial system with new energy and new materials as key elements, relying on abundant clean energy and strategic mineral resources. Therefore, the core thread that must be long-term supported in this transformation is sustainable development. The ecological status of the western region is important but fragile, which determines that it must explore a new development path of ecological protection and economic growth that are mutually supportive. Therefore, the key to the future development prospects of the western region lies in achieving high-quality growth with resource intensification, green and low-carbon development, and transforming ecological advantages into economic advantages, truly achieving harmony and win-win between humans and nature [3].

However, the industrial chain and supply chain in the western regions still face many challenges, including a relatively single industrial structure, insufficient completeness of the industrial chain, scattered resources with low utilization

efficiency, and low efficiency in resource allocation due to information asymmetry. These factors have constrained the innovation ability and market competitiveness of the economy in the western regions [3].

The rise of the digital economy has provided opportunities for the western regions to solve their own development problems. From the perspectives of industrial upgrading and sustainable development, the digital economy has brought opportunities for the development of the western regions. In terms of industrial upgrading, the integration of digital technology with traditional industries can enhance production efficiency and improve the resilience of the industrial chain. For example, manufacturing enterprises in the western region have adopted digital management systems, with data stored and shared through blockchain to ensure the authenticity and non-modifiability of the data, improving the authenticity of supply chain information transmission and alleviating the phenomenon of data silos, thereby achieving resource optimization allocation [2]. Moreover, through the integration of data from multiple parties on cloud computing platforms, enterprises can dynamically adjust production plans based on actual needs, avoiding overcapacity [4]. Secondly, manufacturing industries utilize digital twins and other digital supply chain constructions to achieve simulation and simulation of the entire supply chain from suppliers, factories, distributors, to customers. Through digital algorithms, they can achieve real-time insights into the status of the supply chain and risk prediction, thereby enhancing supply chain resilience [5]. In terms of innovation-driven development, the wide application of digital technologies such as big data, artificial intelligence, and cloud computing provides a broader space for the western regions to cultivate new economic growth points, serving as a continuous driving force for attracting innovative talents and capital inflows. In terms of green transformation, digital technologies can empower energy conservation and emission reduction, precisely control pollution emissions using environmental monitoring big data, and promote the transformation of industries towards greening and low-carbonization. In agricultural development, digital platforms can be used to understand the market gaps of specialty agricultural products and guide agricultural production towards higher value categories; at the industrial level, through industrial internet monitoring of data on energy and other resource extraction and processing, production processes can be optimized. This precise allocation enables the western regions to break away from the "extensive development" path, gradually building a more reasonable and competitive industrial structure, thereby alleviating development difficulties.

The core objective of this study focuses on the collaborative mechanism of the industrial chain and supply chain in the western region of China under the background of the digital economy. This paper specifically examines the linkage and upgrading of the industrial chain and supply chain in the western region of China, and explores how the development of the digital economy drives the linkage and upgrading of the industrial chain and supply chain to empower sustainable development. This article mainly focuses on how digital technology changes the existing form and operation mode of industrial chains and supply chains to promote sustainable development. On this basis, we also explore from three perspectives - regional economic development, ecological environment optimization, and social equity - what support digital technology and the linkage of industrial chains and supply chains can provide for sustainable development. In terms of theoretical value, this research can help us build an interdisciplinary analytical framework integrating economics, supply chain management, regional economics, and sustainable development, and also deepen our theoretical understanding of "industrial synergy" and "supply chain management". In the past, studies on supply chains mostly focused on how individual enterprises or a certain industrial chain could improve efficiency; this time, we adopt a "meso perspective", that is, focusing on the linkage of industrial chains and supply chains at the regional level, with a particular emphasis on the collaborative cooperation among different industries and industrial clusters, and then analyze how industrial chains and supply chains achieve deep integration under the assistance of the digital economy. In terms of practical application, the value of this research is also obvious: by detailing the specific paths through which the digital economy plays a role, it can provide references for governments at all levels and enterprises. For example, how to use digital technology to deal with risks in industrial chains and supply chains, and how to optimize the industrial layout within a region, these practical problems can all find directions here.

2 RELATED CONCEPTS AND MECHANISMS

2.1 Concept and Current Situation

Currently, the digital economy has become a crucial driving force for the transformation of the global economy, and has also attracted continuous attention from the academic community. In simple terms, the digital economy refers to a new economic model that relies on the application of digital technologies to promote economic restructuring and reconfigure traditional industrial chains. Some scholars [1] have proposed that the digital economy is a new economic form centered on digital knowledge and information technology, with modern information networks as its carrier, and driven by information technology for development. It mainly consists of two parts: digital industrialization and industrial digitalization. Among them, industrial digitalization focuses on using digital technologies to upgrade and transform traditional industries, which has profoundly changed the ways of production, transactions, and consumption in society. Regarding the characteristics of the digital economy and its enabling role, we have made a brief summary in Table 1.

Table 1 Characteristics and Enabling Functions of the Digital Economy

Feature	Description

Data as a key production factor	Data is the core resource of the digital economy
Digital infrastructure as the core cornerstone	Digital infrastructure supports all digital activities
Digital technology drives economic growth	Technologies such as IT, the Internet of Things, big data, and AI promote development
Widespread application of digital resources	Digital resources widely penetrate traditional industries
In-depth integration of digital industries and traditional industries	In-depth collaboration between old and new industrial chains
Significant improvement in economic operation efficiency	Efficiency improvement in the entire process of production, circulation, and services

The theory of sustainable development serves as the fundamental principle guiding the coordinated development of the economy and society. Its core lies in achieving a dynamic balance among economic development, environmental protection, and social equity. Guided by this goal, the synergy between the digital economy and the industrial chain and supply chain has jointly formed a new paradigm for promoting sustainable development. Among them, the digitalization of supply chains serves as a key driving force, effectively promoting the construction of green supply chains and providing specific paths and support for achieving sustainable development [6]. The enabling role of digitalization can be simply summarized as using digital technologies to conduct refined management and optimization of the entire process of products from raw materials, production, sales to recycling. This can significantly reduce resource waste and environmental pollution, and effectively promote the construction of "green supply chains". If focusing on regional sustainable development, the western regions have the characteristics of both abundant resources and fragile ecology. This "both rich and fragile" contradiction determines that the western regions cannot follow the earlier "high energy consumption, high pollution" extensive development path. The green sustainable development strategy and digital transformation are the inevitable choice for achieving sustainable development in the western regions.

However, in the western regions, the application and innovation of relevant theories have significant practical significance and special challenges. On one hand, although the digital economy infrastructure construction in the western regions started relatively late, it has grown rapidly in recent years, and digital technology has become a key driving force for the linkage of regional industrial and supply chains. On the other hand, the shortage of talents, unbalanced infrastructure construction, and complex and changeable market environment determine the differentiation of the digital economy empowerment mechanism. Therefore, how to analyze the current development status and core challenges of regional industrial and supply chains in a local context, systematically evaluate the regional sustainable development level, and scientifically grasp the empowerment mechanism and implementation path of digital economy for regional industrial transformation have become important topics for promoting high-quality regional economic development and building a modern economic system. In-depth research on this topic has key theoretical value and practical significance for enhancing industrial chain resilience, optimizing supply chain layout, achieving regional coordination and green low-carbon development. Table 2 compares the core elements of digital economy, industrial and supply chain linkage, and sustainable development.

Table 2 Comparison of Core Elements of Digital Economy, Industrial Chain and Supply Chain Linkage, and Sustainable Development

Theoretical Element	Main Content
Digital Economy	By taking data as the key element, we can achieve the digitalization, networking and intelligence of economic activities.
Industrial Chain and Supply Chain Linkage	Cross-enterprise, cross-industry, and cross-regional collaborative integration and process optimization; upstream and downstream collaboration, information sharing, integration of logistics and

	capital flow, and risk sharing.
Sustainable Development	Resource conservation, low-carbon emissions, ecological protection, social equity, inclusive growth.

2.2 THE DIGITAL ECONOMY EMPOWERS THE LINKAGE AND SUSTAINABLE DEVELOPMENT OF REGIONAL INDUSTRIAL AND SUPPLY CHAINS

The current term "digital economy" refers to a new economic form driven by digital technologies. Technologies such as big data, cloud computing, the Internet of Things, and 5G communication, which are commonly heard of, all fall within its scope - it has brought profound changes to the traditional economic model [7]. From a macro perspective, the digital economy has taken a path of development driven by innovation by integrating various technologies and reconfiguring information resources. This has been of great help in reshaping and optimizing the industrial chain and supply chain. Especially when the industrial chain and supply chain cooperate and develop in a coordinated manner, the digital economy not only enables faster and smoother information transmission but also enhances the cooperation capabilities among enterprises. As for how the digital economy promotes the linkage of industrial chains and supply chains in the western regions, the specific approaches mainly focus on two aspects: one is the practical application of digital technologies, and the other is to drive development through innovation. Firstly, big data technology, through real-time collection and in-depth analysis of data from each link of the industrial chain, realizes data visualization, significantly improving the transparency of the supply chain and the ability of risk warning, effectively promoting information sharing in the raw material supply, production processing, sales distribution and other links. Secondly, cloud computing provides timely and effective data resource support for enterprises in the western region, making cross-regional and cross-enterprise resource integration and collaborative management possible, reducing the spatial limitations and operational costs of information exchange. Moreover, the Internet of Things technology, through intelligent sensing devices connected to the network, realizes real-time perception and automatic control of supply chain nodes, significantly enhancing the intelligence level of the supply chain. Taking western characteristic industrial parks as an example, by building a digital collaborative platform, gathering data and technical resources from upstream and downstream enterprises, promoting the deep integration of R&D, production and market links, improving the integration degree of the industrial chain and the resilience of the supply chain, and forming a typical model of leveraging the digital economy to enhance regional competitiveness [7]. The application of these digital technologies has facilitated timely communication of information and optimized resource allocation, alleviating the problems of information lag and resource waste in traditional industrial and supply chain chains.

At the environmental level, digitization has brought about unprecedented visibility. Through IoT sensors and connected devices, the consumption and utilization of resources are no longer haphazard but can be monitored and measured in real time with precise data. This transparency enables enterprises to precisely identify the sources of waste and emissions and automatically optimize. The immutable data chain built by blockchain technology realizes precise traceability of resources from source production, terminal consumption to final recycling, providing a way for data visualization. Moreover, with the widespread application of smart contracts, enterprises can achieve full-process management through automatically executed electronic contracts, enabling precise resource allocation. This not only improves the efficiency of resource matching but also reduces resource consumption and environmental impact, achieving a dynamic balance of shared environmental risks and shared economic benefits [8].

On the economic front, digitization has led to a transformation from owning products to sharing capabilities and services. Data-driven flexible manufacturing capabilities have made supply chains more "flexible". Under the traditional model, enterprises often carry out batch production based on historical sales data and market forecasts. Once market demand suddenly changes, it is difficult for enterprises to quickly adjust their production plans, which can lead to situations such as insufficient supply of products, missing market opportunities, or excessive product accumulation and occupation of funds and storage space. By collecting real-time market demand data and inventory data of each link in the supply chain through digital technology, production parameters, raw material procurement plans and production schedules can be adjusted quickly, which improves the overall operational efficiency. Haier's launch of COSMOPlat is a typical case of how digitalization drives the development of the industrial chain and supply chain. This platform introduces an industrial internet platform that enables users to participate in the entire process of experience. Haier's "chain group contract" model and COSMOPlat, in essence, restructure enterprises into an open value co-creation network. The two jointly support the operation of a networked ecosystem [9]. This model achieves the synergy of organizational efficiency and user value through user demand-driven and chain group autonomous bidding, realizing the innovation of product design concepts directly participated by users. This production mode based on demand-driven effectively reduces resource waste caused by mismatch between supply and demand, making the entire economic model more adaptable to market fluctuations, with stronger resilience and higher operational efficiency.

At the societal level, the establishment of digital platforms enables different groups and market participants of various scales to share the development dividends more equally, breaking the geographical limitations on economic activities and becoming a direct link connecting producers in remote areas with global consumers. In the traditional agricultural supply chain, the characteristic agricultural products grown by small farmers in remote areas and the handicrafts

meticulously crafted by artisans often have to go through multiple layers of middlemen before reaching consumers. Each layer of middlemen adds a price increase, resulting in a significant reduction in the profits that producers ultimately receive, and consumers have to pay higher costs for these intermediary links. However, through platform economy via internet technology, small farmers and artisans can directly showcase and sell their products on the platform, allowing consumers to directly understand the origin of the products and the stories of the producers, achieving direct sales from the place of origin to the users. This not only reduces unnecessary intermediary links, reduces value loss, but also enables the producers creating value to obtain more benefits and makes the distribution of value more directly inclined towards labor and creation [10]. Digitalization of agricultural supply chains, such as blockchain and smart contracts, can solve the problems of information asymmetry, quality fraud, and trust loss in the agricultural product circulation process [11]. Table 3 shows a comparison of the multi-dimensional mechanisms of digital economy promoting the linkage of industrial chains and supply chains to promote sustainable development.

Table 3 Comparison of Multi-dimensional Mechanisms of Digital Economy Promoting Industrial Chain and Supply Chain Linkage to Facilitate Sustainable Development

Dimension	Promotion Mechanism
Economic	Using big data to analyze market demand, reduce overproduction and stockouts, and lower inventory costs. Digital technology accelerates the integration of industrial chain and supply chain, optimizes resource allocation, improves the efficiency of manufacturing and logistics, and reduces costs and inventory.
Social	The agricultural product traceability system ensures food safety. In emergencies such as the epidemic, smart supply chains can efficiently dispatch living materials. E-commerce platforms help agricultural products from remote areas be sold across the country, increase farmers' income, and contribute to rural revitalization.
Environmental	Using digital twin technology to track the entire process of products from materials, production, use to recycling, facilitating classification, recycling, and reuse.

3 DIGITAL ECONOMY EMPOWERING INDUSTRIAL AND SUPPLY CHAIN UPGRADING IN WESTERN CHINA

However, the promotion effect of the digital economy on the linkage of industrial chains and supply chains in the western regions also faces many practical challenges. Firstly, the overall digital infrastructure construction in the western regions is uneven. The western regions have a vast territory and complex terrain, which leads to higher construction and operation maintenance costs for 5G base stations, fiber optic networks, and IoT facilities compared to the eastern regions. The "digital divide" phenomenon is significant. Even in the areas with infrastructure coverage, the network quality, the scale and efficiency of data platforms are relatively lagging, making it difficult to meet the strict requirements of modern industrial chains for real-time transmission, storage, and processing of massive data, resulting in a lack of a solid foundation for the digital perception and intelligent decision-making of supply chains. Secondly, the shortage of professional technical talents is prominent, and the supply of talents for digital technology development, application, and management is insufficient. The western regions are at a disadvantage in terms of attracting and retaining talents, lacking both compound talents who are proficient in industry knowledge and digital technology, and cutting-edge technical talents who can conduct big data analysis and develop artificial intelligence algorithms [7]. Moreover, there are inconsistent data standards and information silos among the industrial chains and supply chain enterprises in the western regions, and there is a lack of effective cross-industry data sharing platforms, which hinders the circulation and collaborative innovation of digital information. Finally, data sharing among government departments and between upstream and downstream enterprises in the industrial chain is difficult. Due to data security and privacy protection mechanisms, enterprises and governments face security risks in the data management process, which affects the initiative and reliability of information sharing. These constraints directly affect the effectiveness of the industrial chain and supply chain linkage mechanism stimulated by the digital economy.

The aforementioned analysis indicates that numerous challenges such as lagging digital infrastructure, weak foundation for industrial digitalization, and scarcity of high-end talents collectively restrict the enabling effect of the digital economy on the industrial and supply chain ("dual chains") in the western regions of China. However, it must be

recognized that the western regions are not a homogeneous whole. Different provinces within the region, due to differences in resource endowment, geographical conditions, and strategic positioning, exhibit significant differences in the paths and challenges of "dual chain" upgrading. Therefore, this paper selects Xinjiang as a sample for a further brief analysis.

The digital economy, as an important engine of economic development in the new era, holds profound strategic significance for Xinjiang to achieve sustainable development and the linkage of industrial chains and supply chains. Xinjiang is located in the northwest of China and is an important node in the "Belt and Road" initiative. The digital economy infrastructure is constantly improving, providing solid technical support for the deep integration of industrial chains and supply chains. In the current global context of digital transformation, by combining Xinjiang's unique geographical advantages and resource endowments, systematically studying the contradictions and synergies between sustainable development and the linkage of industrial chains and supply chains under the background of digital economy has important theoretical value and practical significance. Through in-depth analysis of the main contradictions and potential opportunities faced by Xinjiang, exploring effective paths for coordinated development, not only provides solutions for regional high-quality development, but also offers references and impetus for promoting the deep integration of digital economy and real economy in the western regions of China. Therefore, this article conducts a detailed analysis of how Xinjiang can achieve a balance and synergy between the linkage of the industrial chain and supply chain and sustainable development under the leadership of the digital economy; it examines the related contradictions and opportunities, and proposes policy suggestions and optimization paths, thereby promoting the green transformation and innovation upgrade of the regional economy.

At present, during the process of promoting the linkage of the industrial chain and supply chain in Xinjiang, multiple contradictions still exist and need to be addressed urgently. Firstly, the pressure on resources and the environment is quite prominent. Xinjiang has a dry and infertile climate, and its ecological environment is somewhat fragile. Moreover, with the continuous expansion of mineral energy development and industrial production, the problems of water scarcity and environmental pollution have become the key factors restricting its sustainable development [12]. Secondly, the uneven level of digital transformation is also one of the prominent contradictions. Although 5G networks have been fully covered in the central urban areas of Xinjiang prefectures, the digital infrastructure in remote areas is still not complete [13]. Moreover, the unsmooth logistics information and low transportation efficiency have become the weak links in the linkage of the industrial chain and supply chain, restricting the digital upgrading of industries and the speed of market response. These contradictions not only directly affect the overall efficiency of the industrial chain and supply chain, but also hinder Xinjiang's transformation from a resource-consuming type to a green and sustainable type, becoming the development bottlenecks that need to be solved urgently.

Based on the analysis in this section, in the face of the situation where the potential of digital economy development in Xinjiang and the linkage between the industrial chain and supply chain coexist, the future should focus on optimizing the following paths. First, it is necessary to strengthen policy support, improve the regulatory and policy framework for the digital economy, and accelerate the transformation and innovation of the green industry. Secondly, continuously enhance the construction of digital infrastructure, especially the computing power network and 5G coverage [13]. Third, formulate and improve green industrial chain and supply chain standards, promote full-process green and low-carbon management, and improve resource utilization efficiency. Fourth, build an efficient regional collaboration mechanism to achieve in-depth cooperation among upstream and downstream enterprises, government departments, and research institutions, forming a diversified and mutually beneficial linkage pattern. Finally, strengthen talent cultivation and the promotion of digital technology, enhance the digital capabilities of enterprises and the level of green transformation, strengthen the construction of digital talent teams, and provide sufficient human resources guarantee for the digital process in the western region [13]. These paths not only provide practical and feasible optimization solutions for the linkage of digital economy and industrial chain and supply chain in Xinjiang, but also lay a solid foundation for achieving the overall green and high-quality development goals of the western region, and have important promotion value and strategic significance.

4 CONCLUSION

The interconnection between the industrial chain and the supply chain essentially means integrating the overall macro-level industrial planning with the daily operational management of individual enterprises, ultimately building a modern industrial system with greater risk-resistance capabilities, higher cooperation efficiency, and the ability to control key links independently. This effective interconnection plays a crucial role in the long-term development of the economy and society in the western region. Take the role of digital technology as an example. By optimizing the coordination of each link in the supply chain through digital technology, not only is the resource allocation more reasonable and unnecessary waste reduced, but in the long run, it also provides tangible assistance in protecting the environment. Through digital means to achieve precise monitoring and management, it helps to reduce carbon emissions and lower energy consumption, promoting the realization of the green development goals. On the other hand, enhanced resilience of the industrial chain and supply chain has improved the anti-risk capabilities of the supply chain and the industrial chain. Moreover, the industrial chain collaboration under the background of the digital economy helps to narrow the gap in industrial development levels between the western regions and the developed eastern regions, promotes balanced regional economic development, and enhances the economic anti-risk capacity and sustainable development potential of the entire western region.

Although the digital economy has become an important engine driving the linkage of regional industrial chains and supply chains in the western region, by optimizing the coordination of information flow, logistics and capital flow, it has significantly improved the overall efficiency and collaboration level of the industrial chain, and promoted resource optimization allocation, environmental protection, social equity. However, bottlenecks such as differences in digital infrastructure, imperfect coordination mechanisms and insufficient policy support still affect the coordinated development and sustainable progress of the industrial chain and supply chain in the western region. Only by combining comprehensive strategies such as strengthening infrastructure construction, deepening regional collaboration, improving financial support and promoting the application of green digital technologies, can the western region fully unleash the potential of the digital economy, achieve efficient integration of industrial and supply chain linkage, and promote the regional economy and society towards a green, high-quality and sustainable future.

COMPETING INTERESTS

The authors have no relevant financial or non-financial interests to disclose.

FUNDING

This study was supported by the Silk Road Economic Belt Core Area Industrial High-quality Development Research Center, Xinjiang Normal University Think Tank Bidding Project (ZK202326C); Research Outcomes Supported by the University Basic Scientific Research Operating Expenses Program (XJEDU2025J094).

REFERENCES

[1] Hao X, Wang X, Wu H, et al. Path to sustainable development: Does digital economy matter in manufacturing green total factor productivity?. Sustainable Development, 2023, 31(1): 360-378.

[2] LIU N N, JIANG D H. Research on the Digital Economy Driving the Resilience Improvement of the Manufacturing Industry Chain in Western China. China Journal of Commerce, 2025, 34(12): 31-35. DOI: 10.19699/j.cnki.issn2096-0298.2025.12.031.

[3] ZHANG X, CUI R M. Strategies for Embedding Western China into the New Development Pattern of 'Dual Circulation'. Journal of Yunnan Minzu University (Philosophy and Social Sciences Edition), 2021, 38(3): 128-135. DOI: 10.13727/j.cnki.53-1191/c.2021.03.016.

[4] W M Samanthi Kumari Weerabahu, Premaratne Samaranayake, Dilupa Nakandala, et al. Digital supply chain research trends: a systematic review and a maturity model for adoption. Benchmarking: An International Journal 2023, 30(9): 3040-3066.

[5] Kamble SS, Gunasekaran A, Parekh H, et al. Digital twin for sustainable manufacturing supply chains: Current trends, future perspectives, and an implementation framework. Technological Forecasting and Social Change, 2022, 176: 121448.

[6] Khan S A R, Godil D I, Jabbour C J C, et al. Green data analytics, blockchain technology for sustainable development, and sustainable supply chain practices: evidence from small and medium enterprises. Annals of Operations Research, 2025, 350(2): 603-627.

[7] WANG Y Z, PU X C. Digital Economy and High-Quality Development in Western Counties: A New Economic Form and Development Model for County-Level Economies. Data, 2022(5): 44-46.

[8] Zhang X, Liu C, Medda F. A smart-contract-aided plastic credit scheme. IEEE Systems Journal, 2022, 17(1): 1703 -1713.

[9] Ding, D. Case study on value cocreation mechanism of Haier COSMOPlat industrial internet platform. Modern Marketing, 2024(03): 1-3. DOI: 10.19932/j.cnki.22-1256/F.2024.01.001.

[10] WANG J B, ZHANG L D. Research on the Adoption Strategy of Blockchain Traceability Technology in Contract Farming Supply Chains. Systems Engineering — Theory & Practice, 2024, 44(2): 612-628.

[11] Caro Miguel Pincheira, Muhammad Salek Ali, Massimo Vecchio, et al. Blockchain-based traceability in Agri-Food supply chain management: A practical implementation. 2018 IoT Vertical and Topical Summit on Agriculture-Tuscany (IOT Tuscany). IEEE, 2018, 1-4. DOI: 10.1109/IOT-TUSCANY.2018.8373021.

[12] ZHAO F. Research on Agricultural Resource Utilization and Economic Sustainable Development in Xinjiang. Co-Operative Economy & Science and Technology, 2025(8): 22-25. DOI: 10.13665/j.cnki.hzjjykj.2025.08.011.

[13] ZUO S. Development Strategies for the Digital Economy in Xinjiang under the "Dual Circulation" Pattern. Contemporary County-Level Economy, 2024(8): 31-33. DOI: 10.16625/j.cnki.51-1752/f.2024.08.011.

Eurasia Journal of Science and Technology
Print ISSN: 2663-1024
Online ISSN: 2663-1016
DOI: https://doi.org/10.61784/ejst3115

LNCRNA-GASS: A PROSPECTIVE BIOMARKER FOR SEPSIS THERAPY

Dan Yang[1,2], JianQuan Li[2*]
[1]*Zunyi Medical University, Zunyi 563000, Guizhou, China.*
[2]*Intensive Care Unit, Guizhou Provincial People's Hospital, Guiyang 550000, Guizhou, China.*
Corresponding Author: JianQuan Li, Email: lijianquan7205@163.com

Abstract: Sepsis, characterized by life-threatening organ impairment triggered by aberrant host reaction to infection, continues to pose a global health challenge with consistently elevated rates of morbidity and mortality. Long non-coding RNAs (lncRNAs) have emerged as crucial modulators in various biological processes, including the development of sepsis. Among these molecules, lncRNA-GASS has attracted growing interest as a promising biomarker of sepsis. This review compiles the current understanding of lncRNA-GASS, covering its regulatory mechanisms in sepsis, its connections to sepsis-induced organ damage, and its potential as a diagnostic/prognostic biomarker for sepsis treatment.
Keywords: LncRNA-GASS; Sepsis; Biomarker

1 INTRODUCTION

Sepsis is a complex clinical syndrome driven by an abnormal immune response to infection, which progresses from an initial hyperinflammatory phase to subsequent immunosuppression and frequently leads to multiple organ dysfunction syndrome (MODS) [1]. Despite improvements in intensive care and antimicrobial treatments, the mortality rate associated with sepsis remains unacceptably high, emphasizing the urgent requirement for new diagnostic tools and therapeutic approaches [2].
LncRNAs are a category of non-protein-coding RNAs that are more than 200 nucleotides in length and play diverse roles in gene regulation, such as transcriptional and post-transcriptional control, chromatin modification, and cell-to-cell communication [3]. Recently, a growing body of research has indicated that lncRNAs are involved in the pathophysiology of sepsis, making them potential candidates for biomarkers and therapeutic intervention [4]. LncRNA-GASS, in particular, has stood out as a key factor due to its unique functional attributes and regulatory impacts in sepsis.

2 OVERVIEW OF LNCRNA-GASS

2.1 Structure and Fundamental Characteristics

LncRNA-GASS has a unique nucleotide sequence and secondary structure, and it is transcribed from specific genomic locations. Its length and sequence composition are key factors that determine its functional abilities [5-6]. For example, certain segments within lncRNA-GASS allow it to interact with DNA, RNA, or proteins. Although the exact structural features of lncRNA-GASS are still being studied, the conservation of its core sequence elements across different species suggests that it has biologically important functions that have been preserved through evolution.

2.2 Expression Patterns in Normal and Septic States

Under normal physiological conditions, lncRNA-GASS is expressed at a basal level in various tissues and cell types. However, in both septic patients and experimental models of sepsis, its expression undergoes significant changes. For instance, in peripheral blood mononuclear cells (PBMCs) of septic patients, the expression of lncRNA-GASS is notably dysregulated compared to healthy individuals [7-8]. Tissue-specific expression patterns are also observed in the lungs of septic mice, a decrease in lncRNA-GASS expression is associated with the development of sepsis-induced acute lung injury (ALI), highlighting its tissue-specific functions in the pathogenesis of sepsis [7].

3 MECHANISMS OF LNCRNA-GASS IN SEPSIS

3.1 Regulation of the Inflammatory Response

3.1.1 Interaction with miRNAs

LncRNA-GASS functions as a competing endogenous RNA (ceRNA) to bind and sequester miRNAs, thereby influencing the expression of miRNA-targeted genes involved in inflammatory signaling pathways [9]. In vitro studies using lipopolysaccharide (LPS)-induced sepsis models have shown that overexpression of lncRNA-GASS increases the levels of TNF-α, interleukin-6 (IL-6), and interleukin-1β (IL-1β) by sequestering miR-223—a miRNA that directly targets the 3' untranslated regions (3'UTRs) of the mRNAs of these proinflammatory cytokines [10].

3.1.2 Regulation of transcription factors

LncRNA-GASS also affects the transcription of inflammatory genes by interacting with transcription factors. For example, it can bind to nuclear factor-κB (NF-κB) to either enhance or inhibit its transcriptional activity [9-10]. In some cases, lncRNA-GASS recruits co-activators or co-repressors to the promoter regions of inflammatory genes, forming complexes with transcription factors to precisely regulate gene expression. A notable example is the lncRNA-GASS-mediated recruitment of co-activators to NF-κB, which helps NF-κB bind to the IL-8 promoter and promotes the transcription of IL-8 [10,11].

3.2 Influence on Cell Death Pathways

3.2.1 Apoptosis

LncRNA-GASS plays a vital role in regulating apoptosis during sepsis, especially in the context of sepsis-related organ damage. In sepsis-induced acute kidney injury (AKI), lncRNA-GASS affects the expression of Bcl-2 family proteins—key regulators of apoptotic cell death. Through interactions with specific miRNAs or direct binding to the promoters of Bcl-2 family genes, lncRNA-GASS can inhibit apoptosis [12]. In a cell model of sepsis-induced renal tubular epithelial cell injury, reducing the expression of lncRNA-GASS increased the levels of anti-apoptotic protein Bcl-2, decreased the levels of pro-apoptotic protein Bax, and ultimately reduced apoptotic cell death [13].

3.2.2 Pyroptosis

Pyroptosis—a proinflammatory form of programmed cell death—contributes significantly to the development of sepsis, and studies have shown that lncRNA-GASS regulates this pathway. Specifically, lncRNA-GASS affects the activation of inflammasomes (such as the NLRP3 inflammasome) either by interacting with components of the inflammasome or by regulating the expression of genes involved in inflammasome activation [14]. In macrophage models of sepsis, overexpression of lncRNA-GASS was linked to increased activation of the NLRP3 inflammasome, leading to more pyroptosis and higher release of proinflammatory cytokines (IL-1β and IL-18) [13].

3.2.3 Impact on autophagy

Autophagy—a cellular self-degradation process that maintains cellular homeostasis and alleviates stress—has recently been associated with the activity of lncRNA-GASS in sepsis. LncRNA-GASS regulates the expression of autophagy-related genes (ATGs), such as ATG5 and ATG7, often through interactions with transcription factors that control the expression of these ATGs [15]. In a mouse model of sepsis-induced liver injury, lncRNA-GASS promoted autophagy by increasing the expression of ATG5 and ATG7, which protected hepatocytes from severe damage by removing dysfunctional organelles and misfolded proteins [16].

4 LNCRNA-GASS AND SEPSIS-ASSOCIATED ORGAN DAMAGE

4.1 Acute Lung Injury (ALI)

LncRNA-GASS is a key factor in the development of sepsis-induced ALI. As previously mentioned, the increase level of lncRNA-GASS expression is associated with the development of ALI [17]. LncRNA-GASS promotes pulmonary inflammation by regulating the expression of pro-inflammatory cytokines and chemokines, and it disrupts the integrity of the alveolar-capillary barrier by affecting the apoptosis and pyroptosis of alveolar epithelial cells and pulmonary endothelial cells—processes that increase vascular permeability, leading to pulmonary edema and impaired gas exchange. Additionally, the regulation of autophagy in lung cells by lncRNA-GASS influences the progression of ALI, highlighting its multiple roles in sepsis-induced lung damage.

4.2 Acute Kidney Injury (AKI)

Sepsis-associated AKI is closely related to the activity of lncRNA-GASS. In the kidney, lncRNA-GASS regulates the survival and function of renal tubular epithelial cells—key targets of sepsis-induced injury. As discussed in Section 3.2.1, lncRNA-GASS affects the apoptosis and pyroptosis of these cells, which are central processes in the development of AKI [12]. Furthermore, lncRNA-GASS impacts renal microcirculation by regulating the function of renal endothelial cells: it modulates the expression of adhesion molecules and vasoactive substances in endothelial cells, changing renal blood flow and contributing to the development of AKI [18].

4.3 Cardiac Dysfunction

Sepsis-induced cardiac dysfunction is a life-threatening complication, and lncRNA-GASS contributes to this pathological condition through multiple mechanisms. It impairs the contractility of cardiomyocytes by regulating the expression of genes involved in cardiac muscle contraction, and it worsens cardiac damage by promoting inflammation and cell death in cardiomyocytes [9]. For example, the lncRNA-GASS-mediated increase in the expression of cardiac proinflammatory cytokines triggers inflammation-related damage to cardiomyocytes, reducing their contractile function and contributing to cardiac dysfunction [11].

5 LNCRNA-GASS AS A BIOMARKER FOR SEPSIS

5.1 Diagnostic Potential

The abnormal expression of lncRNA-GASS in septic patients makes it a promising diagnostic biomarker. Studies have shown that the levels of lncRNA-GASS in PBMCs or plasma of septic patients are significantly different from those in healthy individuals. For example, one study found that plasma lncRNA-GASS levels were increased in septic patients and could distinguish sepsis from healthy controls with moderate sensitivity and specificity [19]. Combining the measurement of lncRNA-GASS with traditional biomarkers (such as C-reactive protein [CRP] and procalcitonin [PCT]) may further enhance diagnostic accuracy, addressing the limitations of current sepsis diagnostic methods [20].

5.2 Prognostic Value

LncRNA-GASS also has prognostic significance in sepsis. Its expression level is associated with the severity of sepsis and patient outcomes: in several study cohorts, extremely high or low expression of lncRNA-GASS in PBMCs was linked to poorer prognosis, including higher mortality rates and longer stays in the intensive care unit (ICU). For instance, a retrospective study of septic patients found that those with lncRNA-GASS expression outside the normal range had a 2.3-fold higher 28-day mortality rate compared to patients with intermediate expression [21]. These findings support the use of lncRNA-GASS as a prognostic tool to identify sepsis patients at high risk.

6 THERAPEUTIC IMPLICATIONS OF TARGETING LNCRNA-GASS

6.1 Antisense Oligonucleotides (ASOs)

ASOs—short, synthetic nucleic acids—can be designed to specifically bind to lncRNA-GASS, blocking its functional activity. Preclinical studies have demonstrated the therapeutic potential of ASOs targeting lncRNA-GASS in sepsis: in a mouse model of LPS-induced sepsis, inhibiting lncRNA-GASS using ASOs reduced the levels of proinflammatory cytokines, suppressed apoptosis and pyroptosis, and improved organ function [22]. However, there are still challenges to overcome for clinical application, including the need for effective in vivo delivery systems and strategies to minimize off-target effects.

6.2 RNA Interference (RNAi)

RNAi technology—which uses small interfering RNAs (siRNAs) to reduce the expression of lncRNA-GASS—represents another therapeutic approach. In vitro studies have shown that reducing lncRNA-GASS expression using siRNAs modulates the expression of genes involved in sepsis pathways, reducing inflammatory responses and cell death [11,19]. Like ASOs, the main obstacle to clinical application is effective in vivo delivery: siRNAs are rapidly broken down in the bloodstream, and targeted delivery to affected organs (such as the lungs and kidneys) remains a technical challenge.

6.3 Small Molecule Modulators

The identification of small molecules that target lncRNA-GASS is an emerging area of research. These compounds can directly interact with lncRNA-GASS or disrupt its interactions with miRNAs/proteins, modifying its functional activity. Although this field is in the early stages, small molecule modulators have advantages over ASOs and siRNAs—including oral bioavailability and easier delivery—making them a promising long-term therapeutic strategy for sepsis.

7 FUTURE DIRECTIONS

7.1 Further Exploration of Molecular Mechanisms

Despite recent progress, there are still significant gaps in our understanding of the mechanisms of lncRNA-GASS in sepsis. Future studies should focus on identifying all miRNAs sequestered by lncRNA-GASS, characterizing its interactions with transcription factors and chromatin modifiers, and investigating its role in intercellular communication (such as through exosomal transfer). Single-cell RNA sequencing and spatial transcriptomics can provide insights into the cell-specific and tissue-specific functions of lncRNA-GASS, enhancing our understanding of its role in organ-specific sepsis pathology.

7.2 Advancing Clinical Translation

Converting preclinical findings into clinical applications requires addressing key technical barriers. For therapeutic agents (such as ASOs and siRNAs), the development of targeted delivery systems—such as nanoparticle-based carriers or exosome-mediated delivery—will be crucial to improve bioavailability and tissue specificity. Additionally, large-scale, multicenter clinical trials are needed to validate the diagnostic and prognostic value of lncRNA-GASS and evaluate the safety and efficacy of therapies targeting lncRNA-GASS in sepsis patients.

7.3 Moving Toward Personalized Medicine

Sepsis is a highly heterogeneous syndrome, and personalized approaches targeting lncRNA-GASS may improve patient outcomes. Future research should explore the use of lncRNA-GASS expression profiles to classify sepsis patients into subgroups with different prognostic risks or treatment responses. For example, patients with high lncRNA-GASS expression may benefit from inhibitors of lncRNA-GASS, while those with low expression may require alternative therapies. Integrating lncRNA-GASS with other omics data (such as transcriptomics and metabolomics) could further refine personalized treatment strategies.

8 CONCLUSION

LncRNA-GASS has emerged as a key regulator of the pathogenesis of sepsis, with multiple roles in modulating inflammatory responses, cell death pathways, and autophagy. Its abnormal expression in sepsis-associated organ damage, along with its potential as a diagnostic and prognostic biomarker, makes it a promising candidate for sepsis management. Although there are still challenges in fully understanding its molecular mechanisms and translating preclinical findings into clinical practice, targeting lncRNA-GASS provides a new opportunity to improve the diagnosis, prognosis, and treatment of sepsis—addressing an unmet clinical need for this life-threatening syndrome.

COMPETING INTERESTS

The authors have no relevant financial or non-financial interests to disclose.

FUNDING

This work was funded by Foundation of Guizhou Science and Technology Cooperation-zk [2023] General 228.

REFERENCES

[1] Singer M, Deutschman CS, Seymour CW, et al. The Third International Consensus Definitions for Sepsis and Septic Shock. JAMA, 2016, 315(8): 801-810.
[2] Rudd KE, Johnson SC, Agesa KM, et al. Global, regional, and national sepsis incidence and mortality, 1990-2017: analysis for the Global Burden of Disease Study. Lancet, 2020, 395(10219): 200-211.
[3] Mercer TR, Dinger ME, Mattick JS. Long non-coding RNAs: insights into functions. Nature Reviews Genetics, 2009, 10(3): 155-159.
[4] Li Y, Yang X, Li J, et al. Long non-coding RNAs in sepsis: functions, mechanisms, and clinical implications. Molecular Immunology, 2019, 112: 120-131.
[5] Kino T, Hurt DE, Ichijo T, et al. Noncoding RNA gas5 is a growth arrest- and starvation-associated repressor of the glucocorticoid receptor. Science Signaling, 2010, 3: ra8. DOI: 10.1126/scisignal.2000568.
[6] Williams GT, Mourtada-Maarabouni M, Farzaneh F. A critical role for non-coding RNA GAS5 in growth arrest and rapamycin inhibition in human T-lymphocytes. Biochemical Society Transactions, 2011, 39: 482–486. DOI: 10.1042/BST0390482.
[7] Li J, Xu H, Li N, et al. Long non-coding RNA growth arrest specific 5 is downregulated in sepsis-ALI and inhibits apoptosis by up-regulating miR-146a. Bioengineered, 2022, 13(2): 4146–4152. DOI: 10.1080/21655979.2021.2014619.
[8] Li M, Zhang Z, Liu B, et al. LncRNA GAS5 upregulates miR-214 through methylation to participate in cell apoptosis of sepsis. The Journal of Metabolic Diseases, 2022, 128(5).
[9] Luo M, Peng Y, Lv D, et al. LncRNA GAS5 downregulates NLRP3 inflammasome activation-mediated pyroptosis in sepsis-induced myocardial injury by targeting SIRT3/AMPKα. Heliyon, 2023, 9(12): e22939. DOI: 10.1016/j.heliyon.2023.e22939.
[10] Wang Z, Yuan J, Qin X, et al. LncRNA GAS5 ameliorates intestinal barrier injury by targeting the miR-223-3p/FBXW7 axis and inactivating NF-κB signaling in vitro and in vivo. The Journal of Pathology, 2025, 267(1): 25 -39. DOI: 10.1002/path.6440.
[11] Gao H, Ma H, Gao M, et al. Long non-coding RNA GAS5 aggravates myocardial depression in mice with sepsis via the microRNA-449b/HMGB1 axis and the NF-κB signaling pathway. Bioscience Reports, 2021, 41(4): BSR20201738. DOI: 10.1042/BSR20201738.
[12] Geng X, Song N, Zhao S, et al. LncRNA GAS5 promotes apoptosis as a competing endogenous RNA for miR-21 via thrombospondin 1 in ischemic AKI. Cell Death Discovery, 2020, 6: 19. DOI: 10.1038/s41420-020-0253-8.
[13] Ling H, Li Q, Duan Z, et al. LncRNA GAS5 inhibits miR-579-3p to activate SIRT1/PGC-1α/Nrf2 signaling pathway to reduce cell pyroptosis in sepsis-associated renal injury. American Journal of Physiology - Cell Physiology, 2021, 321(1): C117-C133. DOI: 10.1152/ajpcell.00394.2020.
[14] Chen T, Meng Y, Zhou Z, et al. GAS5 protects against nonalcoholic fatty liver disease via miR-28a-5p/MARCH7/NLRP3 axis-mediated pyroptosis. Cell Death and Differentiation, 2023, 30(7): 1829-1848. DOI: 10.1038/s41418-023-01183-4.
[15] Li L, Huang C, He Y, et al. Knockdown of Long Non-Coding RNA GAS5 Increases miR-23a by Targeting ATG3 Involved in Autophagy and Cell Viability. Cell Physiology and Biochemistry, 2018, 48(4): 1723-1734. DOI: 10.1159/000492300.

[16] Xu T, Xu X, Chu Y, et al. Long-chain non-coding RNA GAS5 promotes cell autophagy by modulating the miR-181c-5p/ ATG5 and miR-1192/ ATG12 axes. International Journal of Molecular Medicine, 2021, 48(6): 209. DOI: 10.3892/ijmm.2021.5042.
[17] Wang X, Zhang Y, Zhang X, et al. lncRNA-GASS promotes sepsis-induced acute lung injury by regulating the miR-223/TNF-α axis. Journal of Cellular and Molecular Medicine, 2020, 24(20): 11884-11896.
[18] Chen Y, Liu X, Zhang Y, et al. lncRNA-GASS exacerbates sepsis-associated acute kidney injury by regulating the miR-146a-5p/NF-κB pathway. International Journal of Biological Sciences, 2021, 17(8): 2009-2021.
[19] Zeng Z, Lan Y, Chen Y, et al. LncRNA GAS5 suppresses inflammatory responses by inhibiting HMGB1 release via miR-155-5p/SIRT1 axis in sepsis. European Journal of Pharmacology, 2023, 942: 175520. DOI: 10.1016/j.ejphar.2023.175520.
[20] Du J, Jiang H, Wang B. Long Non-coding RNA GAS5/miR-520-3p/SOCS3 Axis Regulates Inflammatory Response in Lipopolysaccharide-Induced Macrophages. Biochemical Genetics, 2022, 60(5): 1793-1808. DOI: 10.1007/s10528-021-10179-z.
[21] Zhang W, Chen B, Chen W. LncRNA GAS5 relates to Th17 cells and serves as a potential biomarker for sepsis inflammation, organ dysfunctions and mortality risk. Journal of Clinical Laboratory Analysis, 2022, 36(5): e24309. DOI: 10.1002/jcla.24309.
[22] Hollie W, Amy C, Bryan E, et al. Structure-function-guided drug development efforts to target lncRNAs. Review Trends Trends in Pharmacological Sciences, 2025, 46(8): 703-721. DOI: 10.1016/j.tips.2025.06.007.

Eurasia Journal of Science and Technology
Print ISSN: 2663-1024
Online ISSN: 2663-1016
DOI: https://doi.org/10.61784/ejst3116

EXTENSION OF NEW MODEL WITH GOOD APPROXIMATION BASED ON RECURRENCE RELATION

PeiPei Ji*, JunHui Yang
School of Health Management, Xi'an Medical University, Xi'an 710021, Shaanxi, China.
Corresponding Author: PeiPei Ji, Email: 13325414692@163.com

Abstract: By using novel recurrence relation, some models with good approximation are constructed, which include three aspects: extension of curve of degree n, extension of surface of degree *n* over rectangular domain. First, based on a novel recurrence relation, we define a Quasi-Bernstein-basis of degree *n* with multiple parameters, which includes the classical Bernstein basis of degree *n* as a special case and has similar properties with the classic Bernstein basis. And the definition, properties, comer cutting algorithm, adjustable effect and quantification of approximation of related curves are discussed in detail. Next, tased on Quasi-Bernstein-basis, we develop a tensor product surface with multiple parameters over rectangular domain, and discuss continuity of Quasi-Bézier-surface at length. Compared with the existing methods, the proposed models keep can beautiful properties of classical method and the multiple parameters introduced in these models can flexibly adjust shape of the generated model and possess good approximation.
Keywords: Recurrence relation; Bernstein basis; Corner cutting algorithm; De Cateljau-type algotithm

1 INTRODUCTION

For many years, free-form curves and surfaces have been the focus of researchers , The classical Bézier model has been widely used for its simple definition and beautiful properties [1]. But there exist some problems. The mainly weak point is that the generated curves and surfaces are fixed relative to their control polygon. We can only adjust the shape by modifying control points [2]. The rational curve and surface can address above problems. However, there are some drawbacks in rational curves and surfaces as well, such as improper use of weight factors may lead to very bad parameterization, or even destroy the subsequent structure of curve and surface [3]. Thus, the construction of free-form model has been a hot topic.

To retain the strong points of the traditional Bézier method,increase the adjustable flexibility of the generated shape of model and improve its approximation, a large number of scholars have started the study of the Bézier curves and patches with parameters and presented many methods[4-13]. Where the most simplest method is to introduce a single parameter or a polynomial containing a single parameter into polynomial space, trigonometric space and exponential space, etc [4-7]. Nevertheless, the ways mentioned above mainly focus on incorporating one parameters into curves and surfaces, which indicates that the generated curves and surfaces only can integrally move to a designated direction. What meaning is that the local shape of these models can not be changed freely.

In order to enhance the adjusting flexibility of generating curves and surfaces, scholars stated to introduce multiple parameters into the constructed model [4-13]. Hu et al. gave a basis with n+1 shape parameters [6], they lately extended this basis to rectangular domain and discussed properties of adjustment, connection of the related surfaces [8]. However, local parameters and global parameter are not independent. Thus, some common strong points in Ref. 4-15 could be concluded: (a) they discuss the essential properties similar to the classical Bernstein basis ; (b) all curves and surfaces contain multiple parameters, which can be used to locally or globally modify the shape of the generated curves and surfaces [4-13].

However, the above methods introduced multiple parameters by not increasing the degree of curves and surfaces. In other words, the approaching ability of the generated curves and surfaces is limited. Therefore, in order to increase the approaching ability of this kind of models, we only accomplish it by increasing degree of models. But the newly coming problem is that when facing the high-order curve, the range of these different parametric values could be taken is different. Therefore, when using these models to practical design, it is necessary to evaluate the range of different parameters. In view of the above, scholars tried to apply the variable degree as adjusting parameter. Costannini constructed a cubic variable-degree basis functions [14], and discussed the form of B-spline lately. Then, Costannini et al. extended the basis functions to degree n [15]. Zhu et al. gave a class of basis with exponential parameters and extended the basis to triangular domain [9,16]. Although these methods can improve the drawback of approaching ability, they still have some problems, such as complex calculation, complex splicing and so on. Moreover, the key point is that these models could only add two parameters at most, so these parameters only serve as global parameters in modeling design, and lack of locally adjustable ability.

In response to the above questions, the purpose of this paper is to propose a novel extended basis of degree n with multiple parameters, which can infinitely approach control polygon. Firstly, a new Quasi-Bernstein-basis of degree n with 2[n/2] parameters, which includes the classical Bernstein basis of degree n as a special case, is defined. Then, we

use method of tensor product to extend it to rectangular domain and construct a class of Quasi-Bernstein-surfaces of degree *n*. Compared with the existing method , the proposed method has multiple parameters, which indicates that the generated curves and patches in this paper can approach the control polygon and mesh infinitely. By adjusting the parametric values, the local shape of the generated curves and patches can be predicted.

Others work of this paper can be concluded as follows: Section 2 gives some work which have been done.Section 3 gives definition and properties of Quasi-Bernstein-basis of degree *n*. Sections 4 discusses the definition,properties, corner cutting algorithm,approaching analysis and comparison and $C^k, C^k(k=0,1,2)$ continuous conditions of the related curve of Quasi-Bernstein-basis of degree *n*. Section 5 gives the definition, properties and $C^k, C^k(k=0,1,2)$ continuous conditions of Quasi-Bézier-surface of degree *n*.

2 PRELIMINARIES

Definition1 The definition of classical Bézier curve of order *n* is:

$$Q(u,v)=\sum_{i=0}^{n} B_{i,j}^{n}(u,v)P_{i,j}^{n}, i,j\in N, i+j=n; u,v\geq 0, u+v=1. \tag{1}$$

Where

$$B_{i,j}^{n}(u,v)=C_n^i u^i v^j=\frac{n!}{i!\,j!}u^i v^j,\quad i,j\in N, i+j=n; u,v\geq 0, u+v=1. \tag{2}$$

is the classical Bernstein basis of order *n*, and $P_{i,j}^{n}$ are control points.

Definition2 The definition of $m\times n$-order classical surfaces over rectangular domain is:

$$Q(u,v;u*,v*)=\sum_{i=0}^{m}\sum_{k=0}^{n} B_{i,j}^{m}(u,v)B_{k,l}^{n}(u*,v*)P_{i,k} \tag{3}$$

where $B_{i,j}^{n}(u,v)$ and $B_{k,l}^{n}(u*,v*)$ are the Bernstein basis given in (2).

Definition 3 For $i,j,k\in N, i+j+k=n, n\geq 2$ and $D=\{(u,v,w)|u+v+w=1; u\geq 0, v\geq 0, w\geq 0\}$ the classical *n*-order Bernstein-Bézier patches over triangular domain are defined as follows:

$$Q(u,v,w)=\sum_{i+j+k=n} B_{i,j,k}^{n}(u,v,w)P_{i,j,k}^{n} \tag{4}$$

$$\text{where}\quad B_{i,j,k}^{n}(u,v,w)=\frac{n!}{i!\,j!\,k!}u^i v^j w^k, (u,v,w)\in D \tag{5}$$

are classical Bernstein-Bézier basis, and $P_{i,j}^{n}$ are control points.

3 QUASI-BERNSTEIN-BASIS OF DEGREE *N*

3.1 Construction of Quasi-Bernstein-Basis

In this subsection, by using a novel recursive relation, the definition of new basis of degree *n* with multiple parameters will be given.

Definition 4 For $i,j\in N, i+j=n, n\geq 2$ and $d=\{(u,v)|u+v=1, u\geq 0, v\geq 0\}$,the Quasi-Bernstein-basis (QB-basis for short) of degree *n* over the domain *d* , with 2[*n*/2] parameters

$\alpha_{x,y}^{n-1}(x,y\in N, x+y=n-1)$ are defined by

$$A_{i,j}^{n}(u,v)=f_{i-1,j}^{n-1}(u,v)B_{i-1}^{n-1}(u,v)+g_{i,j-1}^{n-1}(u,v)B_{i,j-1}^{n-1}(u,v) \tag{6}$$

where

$$B_{x,y}^{n-1}(u,v)=\frac{(n-1)!}{x!\,y!}u^x v^y, (x,y\in N, x+y=n-1) \tag{7}$$

are Bernstein basis of degree *n*-1 over the domain *d*, and

$$\left(\begin{array}{l} f_{i-1,j}^{n-1}(u,v)=\begin{cases} \dfrac{1}{1+\alpha_{i-1,j}^{n-1}(1-u)}u, & i-[(n+1)/2]>0, \\ 1-\dfrac{1}{1+\alpha_{i-1,j}^{n-1}(1-v)}v, & i-[(n+1)/2]\le 0 \end{cases} \\ g_{i,j-1}^{n-1}(u,v)=\begin{cases} \dfrac{1}{1+\alpha_{i,j-1}^{n-1}(1-v)}v, & i-[(n+1)/2]>0, \\ 1-\dfrac{1}{1+\alpha_{i,j-1}^{n-1}(1-u)}u, & i-[(n+1)/2]\le 0 \end{cases} \end{array} \right) \tag{8}$$

if n is even, and

$$\left(\begin{array}{l} f_{i-1,j}^{n-1}(u,v)=\begin{cases} \dfrac{1}{1+\alpha_{i-1,j}^{n-1}(1-u)}u, & i-[(n+1)/2]>0, \\ & i-1,\ j\ne[n/2], \\ 1-\dfrac{1}{1+\alpha_{i-1,j}^{n-1}(1-v)}v, & i-[(n+1)/2]\le 0 \\ & i-1,\ j\ne[n/2], \\ u, & others, \end{cases} \\ g_{i,j-1}^{n-1}(u,v)=\begin{cases} \dfrac{1}{1+\alpha_{i-1,j}^{n-1}(1-v)}v, & j-[(n+1)/2]>0, \\ & i,\ j-1\ne[n/2], \\ 1-\dfrac{1}{1+\alpha_{i-1,j}^{n-1}(1-u)}u, & j-[(n+1)/2]\le 0 \\ & i,\ j-1\ne[n/2], \\ v, & others, \end{cases} \end{array} \right) \tag{9}$$

If n is odd, and $[n/2]\left[n/2\right]=\begin{cases} n/2, if\ n\ is\ even, \\ (n-1)/2, if\ n\ is\ odd. \end{cases}$

Moreover, we always set $\alpha_{x,y}^{n-1}=0$ and $B_{x,y}^{n-1}=0$ whenever one subscript is equal to -1.

Remark 1 Obviously, the QB-basis proposed in this paper has similar form and properties to the classic Bernstein basis of degree n. The difference is that the QB-basis has $2[n/2]$ parameters which can improve the shortcomings of the classic Bernstein basis. In particular, if set all parameters $\alpha_{x,y}^{n-1}=0$, the QB-basis of degree n will degenerate to formula (2).

Remark 2 The QB-basis defined in (6) possesses $2[n/2]$ parameters. Actually, the parameters serve as local parameter, meaning that there exist one single curve segment will be changed when altering a any parameter. In particular, the parameters of QB-basis serve as global parameter when the whole parameters $\alpha_{x,y}^{n-1}$ are taken a same value.

3.2 Properties of the QB-Basis

Theorem 1 The properties of QB-basis given in (6) can be obtained as follows:

(1)Partition of unity: $\sum_{i+j=n}A_{i,j}^{n}(u,v)=1$.

(2)Non-negativity: If all parameters satisfy $\alpha_{x,y}^{n-1}\ge 0$, then $A_{i,j}^{n}(u,v)\ge 0$.

(3)Symmetry: If $\alpha_{x,y}^{n-1}=\alpha_{y,x}^{n-1}$, we have $A_{i,j}^{n}(u,v)=A_{j,i}^{n}(v,u)$, see Figure 1(*a*) and (1)(*b*) .

(4)Terminal properties:When $n \geq 3$, for $v = 1\text{-}u$ and $i, j \in \mathrm{N}$, $j = n - i$,it follows that

$$\begin{cases} A_{n,0}^{n}(1,0)=1, A_{i,n-i}^{n}(1,0)=0(i\neq n), \\ A_{0,n}^{n}(0,1)=1, A_{i,n-i}^{n}(0,1)=0(i\neq 0). \end{cases} \tag{10}$$

By directly differentialing concerning *u*, it follows that

$$\left[A_{i,n-i}^{n}(1,0)\right]'=\begin{cases} n+\alpha_{n-1,0}^{n-1}, i=n, \\ -(n+\alpha_{n-1,0}^{n-1}), i=n-1 \\ 0, others, \end{cases} \tag{11}$$

$$\left[A_{i,n-i}^{n}(0,1)\right]'=\begin{cases} -(n+\alpha_{0,n-1}^{n-1}), i=0, \\ n+\alpha_{0,n-1}^{n-1}, \quad i=1 \\ 0, \quad others, \end{cases} \tag{12}$$

By 2-th differentialing with regard to *u*, it follows that

$$\left[A_{i,n-i}^{3}(1,0)\right]''=\begin{cases} 2(\alpha_{2,0}^{2})^{2}-6\alpha_{2,0}^{2}+6, \quad i=3, \\ -2(\alpha_{2,0}^{2})^{2}+6\alpha_{2,0}^{2}-12, i=2 \\ 6, \quad i=1 \\ 0, \quad others, \end{cases} \tag{13}$$

$$\left[A_{i,n-i}^{3}(0,1)\right]''=\begin{cases} 2(\alpha_{0,2}^{2})^{2}-6\alpha_{0,2}^{2}+6, \quad i=0, \\ -2(\alpha_{0,2}^{2})^{2}+6\alpha_{0,2}^{2}-12, i=1, \\ 6, \quad i=2, \\ 0, \quad others, \end{cases} \tag{14}$$

if $n = 3$, and

$$\left[A_{i,n-i}^{n}(1,0)\right]''=\begin{cases} 2\alpha_{n-1,0}^{n-1}(\alpha_{n-1,0}^{n-1}+n)+n(n-1), \quad i=n, \\ -2\alpha_{n-1,0}^{n-1}(\alpha_{n-1,0}^{n-1}+n)-(n-1)(n+2\alpha_{n-2,1}^{n-1}), i=n-1 \\ 2(n-1)\alpha_{n-2,1}^{n-1}, \quad i=n-2 \\ 0, \quad others, \end{cases} \tag{15}$$

$$\left[A_{i,n-i}^{n}(0,1)\right]''=\begin{cases} 2\alpha_{0,n-1}^{n-1}(\alpha_{0,n-1}^{n-1}+n)+n(n-1), \quad i=0, \\ -2\alpha_{0,n-1}^{n-1}(\alpha_{0,n-1}^{n-1}+n)-(n-1)(n+2\alpha_{1,n-2}^{n-1}), i=1 \\ 2(n-1)\alpha_{1,n-2}^{n-1}, \quad i=2 \\ 0, \quad others, \end{cases} \tag{16}$$

if $n > 3$.

(5)Totally positive property: If all $\alpha_{x,y}^{n-1}>0, A_{i,j}^{n}(u,v)$, form a class of totally positive basis.

(6)Linear independence: If all $\alpha_{x,y}^{n-1}>0,$ the QB-basis given in (6) are linear independence.

4 QUASI-BÉZIER-CURVES OF DEGREE *N*

4.1 Definition of Quasi-Bézier-Curves

Definition 5 Given control points $P_{i,j}\in R^{3}(i,j\in N, i+j=n, n\geq 2),$ and a domain $d=\{(u,v)\,|\,u+v=1, u\geq 0, v\geq 0\}.$ We call

$$R^n(u,v)=\sum_{i+j=n}P_{i,j}A^n_{i,j}(u,v),(u,v)\in d, \tag{17}$$

the Quasi-Bézier-curves (QB-curves for short) of degree n with $2[n/2]$ parameters, where $A^n_{i,j}(u,v)$ are the QB-basis given in (6).

Theorem 2 From Theorem 1, some significant properties of the QB-curves will be organized:

(1)End-points properties: When $n \geq 3$, for $v = 1$ —u and $i, j \in N, j = n$ — i, it follows that

$$\begin{cases} R^n(1,0)=P_{n,0}, \\ R^n(0,1)=P_{0,n}. \end{cases} \tag{18}$$

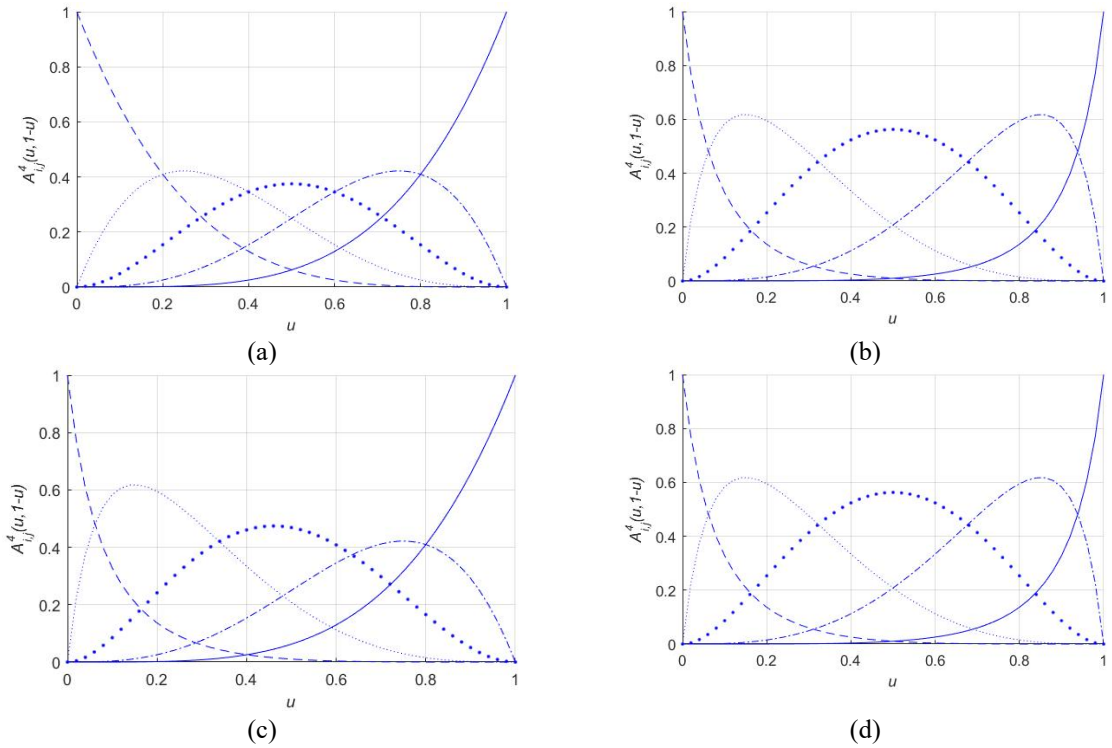

Figure 1 Image of QB-basis with Different Parameters

where, when is shown in Figure 1(a), when is shown in Figure 1(b), when is shown in Figure 1(c), and when is shown in Figure 1(d).

By directly differentialing concerning , it follows that

$$\begin{cases} [R^n(1,0)]'=(n+\alpha^{n-1}_{n-1,0})(P_{n,0}-P_{n-1,1}), \\ [R^n(0,1)]'=(n+\alpha^{n-1}_{0,n-1})(P_{1,n-1}-P_{0,n}). \end{cases} \tag{19}$$

By 2-th differentialing concerning u, it follows that

$$\begin{cases} [R^3(1,0)]''=[2(\alpha^2_{2,0})^2-6\alpha^2_{2,0}+6](P_{3,0}-P_{2,1})+6(P_{1,2}-P_{2,1}), \\ [R^3(0,1)]''=[2(\alpha^2_{0,2})^2-6\alpha^2_{0,2}+6](P_{0,3}-P_{1,2})+6(P_{2,1}-P_{1,2}) \end{cases} \tag{20}$$

if $n = 3$, and

$$\begin{cases} [R^n(1,0)]''=[2\alpha^{n-1}_{n-1,0}(\alpha^{n-1}_{n-1,0}+n)+n(n-1)(P_{n,0}-P_{n-1,1})+2(n-1)\alpha^{n-1}_{n-2,1}(P_{n-2,2}-P_{n-1,1}), \\ [R^n(0,1)]''=[2\alpha^{n-1}_{0,n-1}(\alpha^{n-1}_{0,n-1}+n)+n(n-1)(P_{0,n}-P_{1,n-1})+2(n-1)\alpha^{n-1}_{1,n-2}(P_{2.n-2}-P_{1,n-1}), \end{cases} \tag{21}$$

if n > 3

From formulas (17)-(21), the following conclusions can be deduced:

(1) (a) the QB-curves interpolate to both endpoints of the control polygon, and tangent to the first and the last edge of the control polygon at both endpoints, and (b) the magnitude of the first and the second derivative at both endpoints on QB-curves can be adjusted handily by modifying the shape parameters, which brings considerable convenience to smooth connecting.

(2) Convex hull and affine invariance: Since the QB-basis given in 6 has the properties of partition of unity and non-negativity, then the QB-curves have convex hull and affine invariance.

(3) Symmetry:Given control polygons $P_{n,0}, P_{n-1,1}, \cdots P_{0,n}$ and $P_{0,n}, P_{1,n-1}, \cdots P_{n,0}$, the two class of control polygons define a same QB-curve when $\alpha_{x,y}^{n-1} = \alpha_{y,x}^{n-1}$, that is $R^n(u,v) = R^n(v,u)$.

(4) Variation diminishing property: Since the QB-basis form a class of totally positive basis, then the QB-curves possess variation diminishing property.

(5) Convexity preserving: Since the QB-curves possess variation diminishing property, then the QB curves also possess convexity preserving.

(6) Shape adjustable property: Given a control polygon, the shape of the classical Bézier curve will be completely determined. But for an QB-curve, it is not the case.When fixed the control polygon, the shape of an QB-curve can still be adjusted by changing the $2[n/2]$ parameters.

5 CONCLUSION

This paper proposes a novel class of Quasi-Bernstein basis functions constructed via a new recurrence relation, incorporating multiple shape parameters. On this basis, corresponding Quasi-Bézier curve and surface models are developed. These basis functions not only retain the desirable properties of classical Bernstein bases (such as partition of unity, non-negativity, and symmetry) but also significantly enhance shape adjustability through the introduction of multiple local parameters. The proposed models maintain the advantages of traditional Bézier methods while achieving infinite approximation to the control polygon or mesh via parameter modulation, offering improved local shape control and modeling flexibility.Although the proposed models exhibit excellent performance in shape adjustment and approximation capability, several limitations remain:The number of parameters increases with the degree of the curve/surface, which may complicate parameter selection and optimization in practical applications.The allowable ranges for different parameters in high-degree curves and surfaces may vary, and a unified method for determining these ranges has not been established.The computational complexity of the model is relatively high, which could impact efficiency in real-time interactive design. The current work is limited to tensor-product surfaces over rectangular domains; extension to triangular or other complex domains has not been explored.

Future research will focus on the following aspects:

1. Developing an automatic parameter optimization mechanism to reduce manual intervention and improve modeling efficiency.
2. Extending the proposed basis functions to construct surfaces over triangular domains, further improving their applicability in real-world CAD/CAM systems.
3. Exploring potential applications of the model in isogeometric analysis, reverse engineering, and other related fields.

COMPETING INTERESTS

The authors have no relevant financial or non-financial interests to disclose.

FUNDING

This study was supported by the Scientific research project of Shaanxi Provincial Department of Education (24JK0642); Special Project for the Improvement of Scientific and Technological Capability of Xi'an Medical College (2024NLTS112); Key Project of Shaanxi Education Department :Research on auxiliary diagnosis of mental diseases based on brain network(No. 23JS050).

REFERENCES

[1] Rababah A, Mann S. Iterative process for G 2 -multi degree reduction of Bézier curves. Applied Mathematics and Computation, 2011, 217(20): 8126-8133.
[2] Cao Juan. Adjustment and analysis of curved surface shapes in CAGD. Zhejiang University, 2011(3).
[3] Coelho M, Roehl D, Bletzinger K. Material model based on NURBS response surfaces. Applied Mathematical Modelling, 2017, 51, 574-586.
[4] Oruç H, Phillips M G. q -Bernstein polynomials and Bézier curves. Journal of Computational and Applied Mathematics, 2003, 151(1): 1-12.
[5] Vijay, Prasad P G M, Kumar S G. A new class of cubic trigonometric zipper fractal Bézier curveswith one shape parameter. The European Physical Journal Special Topics, 2025, 1-11. DOI: https://doi.org/10.1140/epjs/s11734-025-01584-1.
[6] Hu G, Wu J, Qin X. A novel extension of the Bézier model and its applications to surface modeling. Advances in Engineering Software, 2018, 125, 27-54.
[7] Shen W, Wang G. Geometric shapes of C-Bézier curves. Computer-Aided Design, 2015, 58, 242-247.
[8] Hu G, Bo C, Wei G, et al. Shape-adjustable generalized Bézier surfaces: Construction and it is geometric continuity conditions. Applied Mathematics and Computation, 2020, 378.
[9] Zhu Y, Han X. Quasi-Bernstein–Bézier polynomials over triangular domain with multiple shape parameters. Applied Mathematics and Computation, 2015, 250, 181-192.

[10] Bashir U, Ali M J. Rational cubic trigonometric Bézier curve with two shape parameters. Computational and Applied Mathematics, 2016, 35(1): 285-300.
[11] Zhu Yuanpeng. Research on Geometric Modeling Theory and Methods with Shape Parameters in Bases. Central South University, 2014(12).
[12] Hu G, Wu J, Qin X. A new approach in designing of local controlled developable H-Bézier surfaces. Advances in Engineering Software, 2018, 121, 26-38.
[13] Han X, Zhu Y. A Practical Method for Generating Trigonometric Polynomial Surfaces over Triangular Domains. Mediterranean Journal of Mathematics, 2016, 13(2): 841-855.
[14] Mazure M. Quasi-Chebyshev splines with connection matrices: application to variable degree polynomial splines. Computer Aided Geometric Design, 2001, 18(3): 287-298.
[15] Mazure M. On dimension elevation in Quasi Extended Chebyshev spaces. Numerische Mathematik, 2008, 109(3): 459-475.
[16] Zhu Y, Han X, Liu S. Curve construction based on four α β -Bernstein-like basis functions. Journal of Computational and Applied Mathematics, 2015, 273, 160-181.